Detecting tissue optical and mechanical properties with an ultrasound-modulated optical imaging system

Yi Cheng

October 2014

Supervised by Dr Meng-Xing Tang and Dr Daniel S. Elson

PhD thesis
Department of Bioengineering
Imperial College London

Submitted for the degree of Doctor of Philosophy of Imperial College London

Declaration of Originality

The work presented in this thesis is my own work unless otherwise attributed.

Yi Cheng

October 2014

Copyright Declaration

Abstract

Tissue optical and mechanical properties are related to tissue pathological changes. The ability to measure both tissue elasticity and its optical properties using the same hardware offers a significant advantage over existing techniques in, e.g. imaging of cancer. Therefore this thesis aims to develop a dual mode imaging system capable of noninvasively sensing local optical and mechanical properties at centimetre depths in samples. The proposed method is based on the detection of photons modulated by ultrasound and shear waves with a modified acoustic radiation force assisted ultrasound modulated optical tomography (ARF-UOT) system.

Firstly the detection of the shear wave and ultrasound modulation with UOT was demonstrated at the surface of tissue mimicking phantoms. The ultrasound field or shear wave wavefront could be imaged by a single CCD exposure and analysis of local laser speckle contrast.

Secondly, within tissue mimicking phantoms, while the shear waves cannot be imaged directly due to optical scattering, the propagation of a transient shear wave was tracked with global laser speckle contrast analysis. A differential method was developed to measure the local shear wave speed and quantify the elasticity of the tissue mimicking phantoms at ~cm depths. The method (SW-LASCA) was based on a modified ARF-UOT system. By generating continuous shear waves at different frequencies, the dispersion of shear wave speed was also investigated. The feasibility of the viscosity measurement was demonstrated by fitting the measured attenuation dispersion using the Voigt model.

Finally, the dual mode system was explored by combining the SW-LASCA and ARF-UOT. The system was demonstrated in an optical reflection detection geometry and

the scanning results of heterogeneous phantoms demonstrated the potential of the system to distinguish optical contrast, mechanical contrast and optical/mechanical contrast in a reflection detection geometry.

Acknowledgements

My gratitude goes first and foremost to my supervisor Dr Meng-Xing Tang who believed in me and gave me the chance to study in his group. During my PhD study, he has given me generous help through all the stages of my PhD. He is always there whenever I need help. His guidance, support and understanding encouraged me to face all the challenges and difficulties on my research.

I also would like to thank my co-supervisor Dr Daniel Elson. It is his illuminating instructions that pushed my research forward. I am also deeply grateful for the time he has spent to listen and discuss with me every week since the first week I started my PhD.

It is a gift to work with intelligent, knowledgeable and most of all nice group members. I owe my deep gratitude to Dr Lipei Song and Dr Rui Li who guided me comprehensively in the early stage of my PhD, especially leading me to the development of my first study. Dr Robert Eckersley is so smart that his genuine advice could always brighten my moody days. Miss Yesna Yildiz and Miss Virginie Papadopoulou were always warm-hearted. Their attitudes about life are an extra harvest. And my fellows, Chee Hau Leow, Yuanwei Li, Shengtao Lin and Tony Cheung made my life enjoyable at London and gave me the chance to share my patriotism out of China.

It is an honour for me to thank Professor David Cosgrove and his family for their precious time spending on me, taking care of me and making my life much easier at London. I will never forget their kindness. Also I need to thank Professor David Cosgrove for his help editing my thesis and correcting my English mistakes.

Next I must thank my parents who are the most important people in my life. Thanks for support me unconditionally. It is their support that makes me brave enough to face life.

Finally, my deepest gratitude goes to my love Sinan Li. Thank you for trying so hard to make me happy every day. Thank you for your patience and tolerance when I was anxious about my experiment and made troubles out of nothing. Thank you for encouraging me when I wanted to give up. Thank you for discussing my results with me and helping me whenever I needed. Without you, I would never finish my PhD.

Table of Contents

List of Publications

1. **Cheng Y.**, Li S.N., Eckersley J.R., Elson S.D. and Tang M.X., *Detecting tissue optical and mechanical properties with an ultrasound modulated optical imaging system in reflection detection geometry.* Biomedical Optics Express, 2015, 6(1): pp. 63-71.

2. **Cheng Y.**, Li S.N., Eckersley J.R., Elson S.D. and Tang M.X., *Viscosity measurement based on shear-wave laser speckle contrast analysis.* Journal of Biomedical Optics, 2013. 18(12): p. 1511-1521.

3. **Cheng Y.**, Li R., Li S.N., Dunsby C, Eckersley J.R., Elson S.D. and Tang M.X., *Shear wave elasticity imaging based on acoustic radiation force and optical detection.* Ultrasound in Medicine & Biology, 2012. 38(9): p 1637-1645.

4. Li S.N., **Cheng Y.**, Song L.P., Eckersley J.R., Elson S.D. and Tang M.X., *Tracking shear waves in turbid medium by light: theory, simulation, and experiment.* Optics Letters, 2014. 39(6): p. 1597 - 1599.

5. Song L.P., **Cheng Y.**, Li R., Tang M.X. and Elson S.D., *Imaging the ultrasound field and shear-wave propagation using acousto-optic laser speckle contrast analysis (AO-LASCA).* Proceedings of SPIE, 2012.

6. Li S.N., **Cheng Y.**, Eckersley J.R., Elson S.D. and Tang M.X., *Dual shear wave induced laser speckle contrast signal and the improvement in shear wave speed measurement.* Biomedical Optics Express (under review).

7. Li S.N., Lin S.T., **Cheng Y.**, Matsunaga O.T., Eckersley J.R. and Tang M.X., *Quantifying activation of perfluorocarbon based phase-change contrast agents using simultaneous acoustic and optical observation.* Ultrasound in Medicine & Biology (accepted).

List of Figures

List of Tables

Chapter 1

Introduction

1.1 Background and motivation

Changes in the mechanical properties of soft tissue, such as elasticity and viscosity, are usually correlated with pathological changes. For example, *in vitro* and *in vivo* studies show fibroadenoma tissue and carcinomas are several times harder than the normal breast tissue [1]. Manual palpation has been used to sense lesions for a long time, such as the digital rectal examination for prostate abnormality. However, it fails when lesions are small or deep in the body. Some lesions, such as breast tumours, are difficult to detect with standard imaging examinations due to the lack of image contrast or resolution [2]. In the past two decades, a number of imaging techniques have been developed to non-invasively measure tissue elasticity. These imaging techniques are based largely on ultrasound (US) and magnetic resonance imaging (MRI) and have been demonstrated, among others, in imaging the breast [3, 4], cardiovascular disease [5, 6], and liver fibrosis [7, 8]. Compared with MRI-based techniques, US-based techniques could be cost effective and real-time. However, the micrometre displacement sensitivity of ultrasound limits its ability to sense small changes of mechanical properties in tissue.

Optical techniques have also been proposed and studied to measure tissue elasticity. They are able to sense sub-nanometre displacements and thus measure subtle changes in elasticity [9]. Furthermore, since elasticity has not been proven to be the discriminated property for tumours, optical techniques could complement the measurement by measuring optical properties which are also correlated to tissue

pathological changes [10]. For example, optical absorption reveals tissue angiogenesis and hypermetabolism which are the hallmarks for cancer [11] and optical scattering spectra provides information of the size distribution of optical scatterers such as cell nuclei which is important indicator of neoplastic precancerous changes [12]. Optical coherence tomography (OCT) has been applied to measure tissue elasticity with a resolution 10-100 times higher than that of US or MRI. However, the imaging depth of OCT is about 2 mm, which limits its ability to measure properties at depth in tissue. Some studies showed results on deep tissue with optical techniques, but they are either invasive [9] or qualitative [13].

Therefore, there is a need for a new technique that is able to noninvasively quantify tissue properties in deep tissue, including mechanical and optical properties. Consequently, the aim of my research is to develop such a dual-mode system that can measure both kinds of properties.

To meet this challenge, I proposed a combination of ultrasound and optical imaging system based on the existing method of ultrasound modulated optical tomography (UOT). UOT is a hybrid technique that combines ultrasound and optics. It uses the local modulation of ultrasound to maintain the optical resolution in deep tissue. Hence, UOT is an optical imaging technique whose resolution is controlled by the US [14]. In this thesis, by utilising the UOT, a dual-mode system is developed and demonstrated with tissue mimicking phantoms. The system not only can quantify elasticity and viscosity of tissue at 1 cm depth but also sense optical absorption properties at the same depth. The system is also studied with reflection geometry where light and detector are positioned on the same side of the sample. The reflection detection geometry is more useful in clinical applications where the light cannot

penetrate compared with the transmission geometry.

1.2 Thesis structure

Chapter 2 is the literature review. Firstly, the measurement of US-based mechanical properties was reviewed, including a brief introduction to elasticity and viscosity and a thorough description of the methods and current state of the ultrasound techniques. Secondly, optical-based techniques to measure mechanical properties were reviewed, including methods for both sub-surface and deep tissue measurements. The final section has two parts. The first part is a brief review of UOT, including the theory, mechanism and current state. The second part includes several topics that correlated to the UOT system that I used, including an introduction of the system setup and a review of laser speckle contrast analysis for the data processing.

Chapter 3 represents an initial study on the development of an alternative application of the UOT system. It proposes a method to image the ultrasound beam and shear wave propagation at the edge of a tissue mimicking phantom. This method provides a fast way to map the ultrasound beam and shear waves at the tissue surface. This study has been included in [15].

Chapter 4 represents the development of an opto-elastography system which can quantify the elasticity with a modified UOT system at ~cm depths in tissue mimicking phantoms. The quantified results were consistent with the results from an independent mechanical test. The sensitivity of the system was also studied by detecting displacement below micrometre amplitude. This part has been published in [16].

Chapter 5 combines the opto-elastography system in Chapter 4 with the UOT system to accomplish a dual-mode system that is sensitive to both mechanical and optical properties. A tissue mimicking phantom with three different inclusions was used to

demonstrate the ability of the combined system. The detection of inclusions was made with a reflection geometry, which was more suitable for using the system in the clinic. Moreover, I also studied the influence of mechanical properties and light intensity on UOT signal. The complex trends of UOT signal in phantoms with different stiffnesses were investigated and discussed. This part has been submitted to Biomedical Optics Express.

Chapter 6 is a study measuring viscosity with the opto-elastography system based on the Voigt model. First of all, both experiment and simulation were conducted to study the feasibility of detecting continuous shear waves in a tissue mimicking phantom. Although it concluded that the differential method used in Chapter 4 did not work with continuous shear waves, I proposed an alternative method to quantify the viscosity using the shear wave amplitude. The results were consistent with those measured with a non-optical method. The method has been published in [17].

Chapter 7 summarises the thesis and contains a thorough discussion about the system and future work.

References

1. Ophir, J., et al., *Elastography: Imaging the elastic properties of soft tissues with ultrasound.* Journal of Medical Ultrasonics, 2002. **29**(4): p. 155-171.

2. Wang, L.V., *Ultrasound-mediated biophotonic imaging: a review of acousto-optical tomography and photo-acoustic tomography.* Dis Markers, 2003. **19**(2-3): p. 123-38.

3. Regner, D.M., et al., *Breast Lesions: Evaluation with US Strain Imaging–Clinical Experience of Multiple Observers.* Radiology, 2006. **238**(2): p. 425-437.

4. Burnside, E.S., et al., *Differentiating Benign from Malignant Solid Breast Masses with US Strain Imaging.* Radiology, 2007. **245**(2): p. 401-410.

5. Trahey, G.E., et al., *Acoustic radiation force impulse imaging of the*

mechanical properties of arteries: In vivo and ex vivo results. Ultrasound in Medicine & Biology, 2004. **30**(9): p. 1163-1171.

6. Pislaru, C., et al., *Ultrasound Strain Imaging of Altered Myocardial Stiffness: Stunned Versus Infarcted Reperfused Myocardium.* Circulation, 2004. **109**(23): p. 2905-2910.

7. Leung, V.Y.-f., et al., *Quantitative Elastography of Liver Fibrosis and Spleen Stiffness in Chronic Hepatitis B Carriers: Comparison of Shear-Wave Elastography and Transient Elastography with Liver Biopsy Correlation.* Radiology, 2013. **269**(3): p. 910-918.

8. Sandrin, L., et al., *Transient elastography: a new noninvasive method for assessment of hepatic fibrosis.* Ultrasound in Medicine & Biology, 2003. **29**(12): p. 1705-1713.
9. Kennedy, K.M., et al., *Analysis of mechanical contrast in optical coherence elastography.* Journal of Biomedical Optics, 2013. **18**(12): p. 121508-121508.

10. Wang, L.V. and H. Wu, *Biomedical Optics: Principles and Imaging*. 2007: Wiley.

11. Folkman, J., *Angiogenesis in cancer, vascular, rheumatoid and other disease.* Nat Med, 1995. **1**(1): p. 27-30.

12. Perelman, L.T., et al., *Observation of Periodic Fine Structure in Reflectance from Biological Tissue: A New Technique for Measuring Nuclear Size Distribution.* Physical Review Letters, 1998. **80**(3): p. 627-630.

13. Bossy, E., et al., *Transient optoelastography in optically diffusive media.* Applied Physics Letters, 2007. **90**(17): p. -.

14. Daniel S. Elson, et al., *Ultrasound-mediated optical tomography: a review of current methods.* Interface Focus, 2011. **1**(4): p. 632-648.

15. Song, L., et al. *Imaging the ultrasound field and shear-wave propagation using acousto-optic laser speckle contrast analysis (AO-LASCA)*. 2012.

16. Cheng, Y., et al., *Shear Wave Elasticity Imaging Based on Acoustic Radiation Force and Optical Detection.* Ultrasound in Medicine & Biology, 2012. **38**(9): p. 1637-1645.

17. Cheng, Y., et al., *Viscosity measurement based on shear-wave laser speckle contrast analysis.* Journal of Biomedical Optics, 2013. **18**(12): p. 121511-121511.

Chapter 2

Measurement of the mechanical properties of tissue and ultrasound modulated optical tomography

Imaging mechanical properties of tissues has gained wide interest because they are closely related to pathological changes of tissue. Many imaging techniques, such as acoustic radiation force elastography imaging (ARFI) and shear wave elastography (SWE) have been developed and some of them are achieving increasing clinical acceptance. However, not all tumours are stiff and not all stiff tissues are tumours. Elasticity alone therefore may not be sufficient to be used as a diagnostic tool and used as an extension of standard ultrasound [1].

The optical properties of biological tissue are sensitive to tissue structure and function, making them promising for the detection of diseases like cancers whose structure is different from normal tissues [2]. Examples of optical imaging techniques include optical microscopy, two-photon imaging and optical coherence tomography (OCT). These techniques can obtain tissue optical contrast with high resolution. Recently, OCT was adapted to measure the mechanical properties of biological tissue and acquire elasticity images with ~μm resolution. More importantly, it intrinsically carries optical information and can potentially provide both mechanical information and optical backscatter anatomy about the tissue, which helps with the diagnosis process. Nevertheless, light suffers from heavy scattering in biological tissues [3] and thus OCT loses resolution in the tissue deeper than ~2 mm.

The aim of my study is to develop a dual-mode system that can measure both optical and mechanical properties in deep tissue. Optical property such as optical absorption

reveals angiogenesis which is the hallmark for caner [4]. To meet this challenge, I proposed a combination of ultrasound and optical imaging based on ultrasound modulated optical tomography (UOT). In this chapter, current methods and techniques measuring tissue mechanical properties are reviewed, including both ultrasound-based and optic-based elastography. Secondly, the mechanisms of UOT are briefly introduced. Finally, several topics related to my study are reviewed, including an introduction of system setup and a study of laser speckle contrast analysis.

2.1 Ultrasound-based mechanical property measurement

Ultrasound-based mechanical property measurement has been investigated intensively during the last two decades and several techniques have been integrated into clinical ultrasound machines. These techniques and methods guided my entire study and they were reviewed in this section.

Ultrasound-based measurement generally includes deforming soft tissue with a certain form of force and monitoring the consequent tissue responses with ultrasound. The responses are then related to either qualitative or quantified mechanical properties. In the following, various techniques were classified and reviewed, based on their ways to deform the tissue. The review was divided into two main sections, one of which reviews elasticity and its measurement and another is about viscosity and the corresponding measurement. Finally ultrasound-based mechanical property measurement is summarized and discussed.

2.1.1 Elasticity

Elasticity is the tendency of a material to return to its original position after being

deformed by an external force. The material experiences the internal forces that oppose the deformation and tend to restore it to its original state [5]. The elasticity of a material can be described by a stress-strain curve that shows stress as a function of strain [6]. The stress σ expresses the restorative internal forces and is defined as the force per unit of a material and the strain ε describes the relative displacement of the material under deformations. The stress-strain curve is unique for each material and reveals many of its properties. The elasticity of a material is measured by an elastic modulus (A) which is defined as the slope of its stress-strain curve in the elastic deformation region where the deformation is reversible:

$$\mathbf{A} \stackrel{\text{def}}{=} \frac{\boldsymbol{stress}(\boldsymbol{\sigma})}{\boldsymbol{strain}(\boldsymbol{\varepsilon})}. \qquad \textbf{(2-1)}$$

In the elastic deformation region (where the deformation is reversible), the elasticity of a material could be linear or nonlinear. Given a small force (thus a small strain) applied in the elasticity measurement of soft tissue, linear elasticity is always assumed. Therefore, an elastic modulus can be measured as the slope of its stress-strain curve.

Specifying how stress and strain are to be measured, many types of elastic moduli are defined, such as Young's modulus (E), shear modulus (G), Poisson's ratio (ν). Homogenous isotropic linear elastic materials have their elastic properties fully described by any two elastic moduli and all others can be calculated. Poisson's ratio is the ratio of transverse to axial strain. Most soft tissues are assumed to roughly incompressible materials and have a Poisson ratio in the range of $0.45 < \nu < 0.49$ [7] which is approximately to be 0.5 in the elasticity measurement. As a result, the elasticity measurement of soft tissue aims to measure either the Young's modulus or shear modulus.

Young's modulus represents the tendency of a material responding a normal strain and shear modulus describes the tendency for a shear strain. The normal strain depicts the change of a material in length which can be expressed as $\varepsilon = \frac{\Delta L}{L}$, where ΔL is the deformation of a material along a certain direction and L is the original length of the material in the same direction as illustrated in Figure 2.1(a)). The shear strain is defined as the angle change between two line segments. In the example in Figure 2.1(b), the shear strain is equal to θ which is the angle change between the θ_1 before load F and θ_2 after the load. Normal and shear strains could occur at the same time as shown in Figure 2.1(c), where not only the elongation and contraction of the block edges but also the rotation of the block diagonals can be observed. Figure 2.1(c) depicts the usual scenario for the soft tissue under load, where the volume is preserved after the deformation (and thus Poisson's ratio is 0.5).

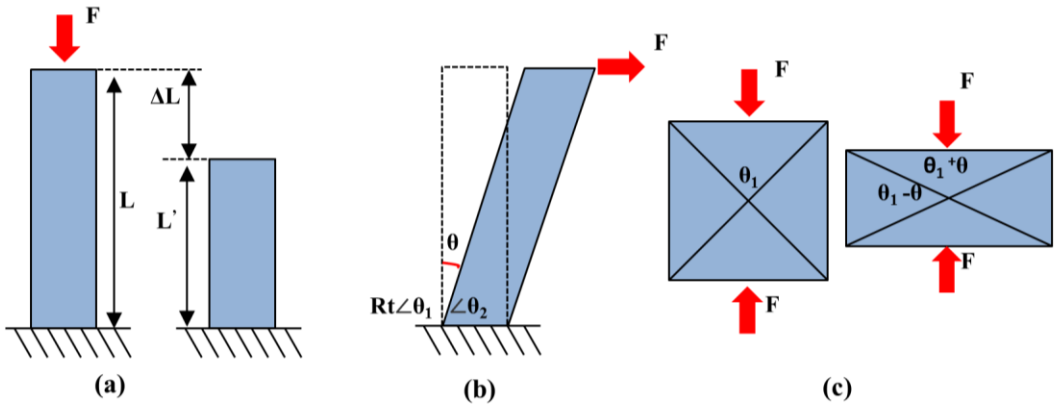

Figure 2.1 Illustration of different strains. (a) Normal strain; (b) Stress strain; (c) Combination of normal and shear strains

A way to measure the elastic modulus of a material is to conduct a compression test that measures the displacement of tissues against an applied force. The compression test usually utilises a testing machine that has two heads: one is for holding the sample and another that is driven to apply force to the sample and measure the

displacement. For example, Figure 2.2(a) shows a typical compression testing machine [8] where the positions of the two heads can be adjusted by a programmable controller. The contracted displacement of tissue (ΔL) between the two heads and the force (F) can be read out from the testing machine. Using prior information about the original length (L) and cross-section area (A) of the sample, a stress-strain curve can be generated as shown in Figure 2.2(b) where the y-axis is the stress (F/A) and x-axis is the strain ($\Delta L/L$). Subsequently, Young's modulus E can be found as the slope of the linear range in the curve (e.g. line S in Figure 2.2(b)).

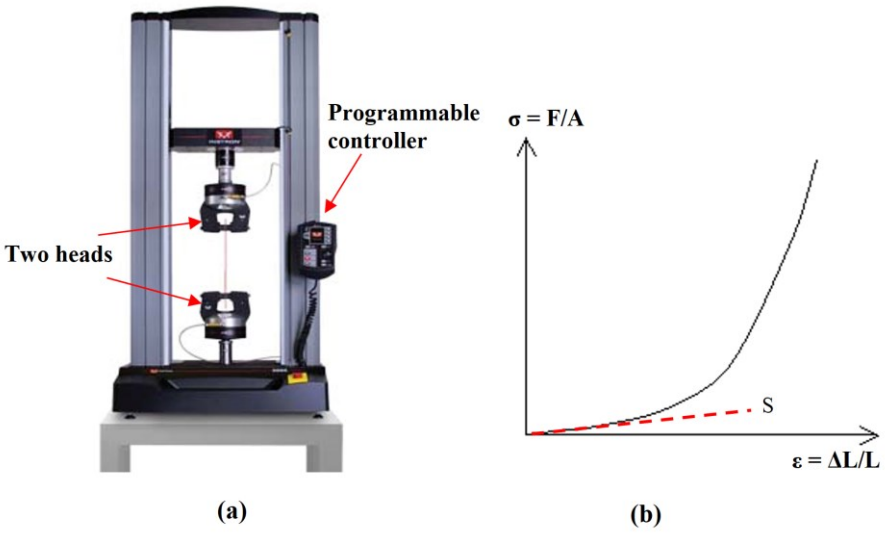

Figure 2.2 (a) A compression testing machine from Instron® [8], where the two heads were for the compression of the sample. The programmable controller was used to control the speed of compression or extension. (b) An example of stress-strain curve where Young's modulus E is the slope of line S. It should be noted that the curve is sketched for illustrative purpose and does not represent real data.

Other ways to quantify the elastic moduli are based on the characterisation of wave propagation in materials. The derivation of the relation between the elastic moduli and wave propagation could start from the equation of motion from Newton's second law. The resultant force F_i acting on an arbitrary volume of material V within a solid is (in

indicial notation)

$$\boldsymbol{F_i = \int_s \ t_i(\vec{n})\, ds + \int_V \ \rho b_i\, dV,} \quad \textbf{(2-2)}$$

where $t_i(\vec{n})$ is the internal traction per unit area on the surface S with the normal $\vec{n}$ that bounds the V, b_i is the body force per mass within V and ρ is the density. These forces are governed by the law of the conservation of linear momentum which states that within a unit time, the total force acting on the body are equal to the change rate of the linear momentum of the body as

$$\boldsymbol{F_i = \frac{\partial P_i}{\partial t} = \partial_t \int_V \ \rho v_i dV,} \quad \textbf{(2-3)}$$

where P_i is the momentum and v_i is the speed. Substituting 2-2 into 2-3, the equation of motion can be found as

$$\boldsymbol{\int_s \ t_i(\vec{n})\, ds + \int_V \ \rho b_i\, dV = \partial_t \int_V \ \rho v_i dV.} \quad \textbf{(2-4)}$$

In the measurement of soft tissue, the time-independent body force $\vec{b}$ can be neglected since the equation can be decomposed into static and dynamic components [9], and the internal surface traction t_i can be fully characterised by Cauchy's stress tensor σ_{ij} as

$$\boldsymbol{t_i(\vec{n}) = n_j\, \sigma_{ij}} \quad \textbf{(2-5)}$$

where σ_{ij} means the *j*th component of traction acting on a plane with normal in the *i*th plane. As a result, by applying the divergence theorem, the equation of motion (2-4) without body forces can be expressed in the terms of Cauchy's stress tensor as

$$\boldsymbol{\partial_j \sigma_{ij} = \rho \partial_t v_i = \ \rho \partial_t^2 u_i,} \quad \textbf{(2-6)}$$

where the u_i is the displacement whose derivation in time is the speed v_i.

In a homogenous and isotropic material, the strain tensor ε_{ij} can be characterised as [9]

$$\boldsymbol{\varepsilon_{ij}} = \frac{1}{2}\left(\boldsymbol{\partial_j u_i} + \boldsymbol{\partial_i u_j}\right). \quad \textbf{(2-7)}$$

Based on Hook's law, the relation of Cauchy's stress tensor and strain tensor can be obtained as

$$\boldsymbol{\sigma_{ij}} = \frac{\boldsymbol{E\nu}}{\boldsymbol{(1-2\nu)(1+\nu)}}\boldsymbol{\varepsilon_{kk}\delta_{ij}} + \boldsymbol{2G\varepsilon_{ij}}, \quad \textbf{(2-8)}$$

where E is Young's modulus, G is the shear modulus, ν is Poisson's ratio and δ_{ij} is the Kronecker delta function which is equal to 1 when $\boldsymbol{i = j}$ and 0 otherwise. Substituting 2-7 and 2-8 into 2-6, the equation of motion can be related to the elastic moduli of the medium as

$$\boldsymbol{\rho\partial_t^2 u_i} = \frac{\boldsymbol{E\nu}}{\boldsymbol{(1-2\nu)(1+\nu)}}\boldsymbol{\partial_i\partial_k u_k} + \boldsymbol{G\partial_i\partial_j u_j} + \boldsymbol{G\partial_j^2 u_i}. \quad \textbf{(2-9)}$$

Further separating the motion field into curl free and div free parts, the equations for the two types of elastic waves (pressure wave (2-10) and shear wave (2-11) respectively) in the medium are then obtained as [10]

$$\boldsymbol{\partial_t^2 u_{pi} = a^2\partial_j^2 u_{pi}};\quad \left(\boldsymbol{a} = \sqrt{\frac{\frac{\boldsymbol{E\nu}}{\boldsymbol{(1-2\nu)(1+\nu)}}+\boldsymbol{2G}}{\boldsymbol{\rho}}}\right), \quad \textbf{(2-10)}$$

$$\boldsymbol{\partial_t^2 u_{si} = b^2\partial_j^2 u_{si}};\ \left(\boldsymbol{b} = \sqrt{\frac{\boldsymbol{G}}{\boldsymbol{\rho}}}\right), \quad \textbf{(2-11)}$$

where the u_{pi} is the displacement of primary wave, u_{si} is the shear wave displacement and $\boldsymbol{a}$ and $\boldsymbol{b}$ are the speeds of the waves respectively.

The pressure wave and the shear wave are two types of elastic waves generated in the body of a material when load is applied. In isotropic and homogenous media, the pressure wave is always a longitudinal wave whose motion is parallel to the travel direction of the wave (Figure 2.3(a)) and can be generated by compression/expansion boundary conditions. The shear wave is a transverse wave whose motion is

perpendicular to the direction of wave propagation (Figure 2.3(b)) and can be generated by shearing boundary conditions. In biological tissues, the speed of the pressure wave is usually more than 1000 m/s whereas the speed of the shear wave is only a few percent of the pressure waves [11].

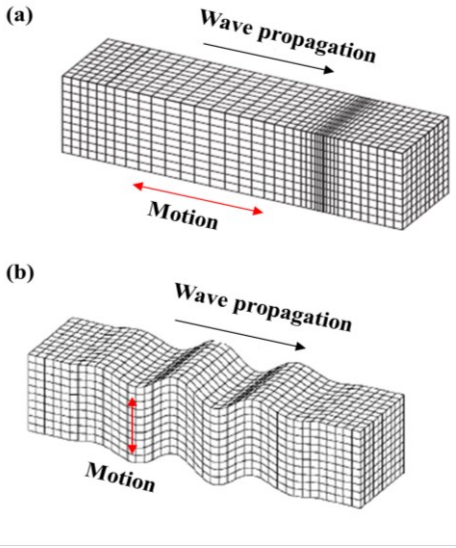

Figure 2.3 Two types of elastic wave. (a) P-wave and (b) Shear wave

Consider a simple one dimension shear wave displacement field $u_s = Asin(kx - \omega t)$ where k is the wavenumber and ω is angular frequency of the shear wave. Substituting this into 2-11, one can obtain

$$\frac{\omega}{k} = \sqrt{\frac{G}{\rho}}, \tag{2-12}$$

which is equal to the speed of shear wave v_s:

$$v_s = \frac{\omega}{k} = \sqrt{\frac{G}{\rho}}. \tag{2-13}$$

Therefore, the shear modulus could be quantified either by measuring the shear wave displacement field in time and space and then inversely solving the shear modulus based on 2-11 [12] , or by measuring the speed of the shear wave and then calculating the shear modulus with 2-13 given the density of soft tissue (usually assumed to be

1000 kg/m^3) [13].

If the frequency of the shear wave is known, an alternative way to calculate the shear wave speed utilises Helmholtz equation

$$\boldsymbol{\partial_j^2 u_{si}' + k^2 u_{si}' = 0,} \quad \textbf{(2-14)}$$

which is obtained by the separation of space and time in 2-11. The u_{si}' is a monochromatic field in the space. The shear wave speed could be derived by inversely finding the wavenumber $\boldsymbol{k}$ and calculating the ratio of the frequency and wavenumber [14].

2.1.2 Elastography (Measurement of elasticity of biological tissue)

Since elasticity imaging was proposed tens of years ago [15], various methods have been devised to estimate tissue elasticity. These methods all combine some forms of tissue deformation techniques with a certain detection method. Currently, ultrasound and magnetic resonance imaging (MRI) are two main modalities for clinical elastography. MRI is an advanced imaging modality and attracting more and more interests, but it is limited by its imaging speed and price. In contrast, ultrasound has the advantage of low cost, real time and mobility, therefore, more researches have been focused on ultrasound elastography, which is consequently the focus of this section.

Displacement estimation

The basic principle of the ultrasound-based elastography is to estimate the displacement of deformed tissue using the changes of ultrasound echo signal in time. All current commercial elastography systems measure the displacement and only differ in how the displacement is used.

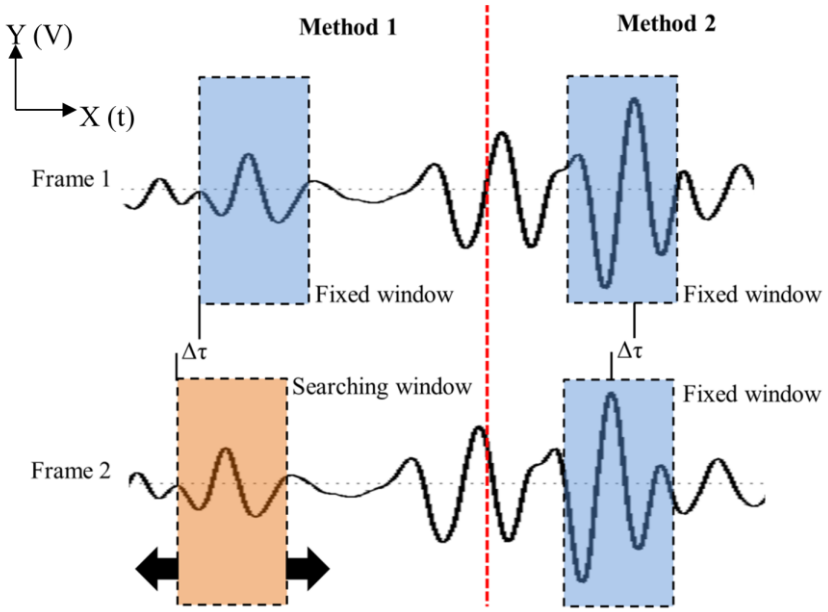

Figure 2.4 Illustration of two cross-correlation based methods for displacement estimation in ultrasound. The blue boxes indicate the fixed windows while the yellow box is the searching window [16].

The cross-correlation-based methods are usually used in ultrasound elastography to estimate displacement. Two most common used methods are depicted in Figure 2.4. In the illustration, Frame 1 and Frame 2 are echoes from the same line of a tissue sample for pre- and post- compression by an external force respectively. The x-axis is time (or depth) and y-axis is the amplitude of the signal. The phase change can be observed in these two echo signals where the phase in Frame 2 is ahead compared with the Frame 1 due to the compression. Method 1 is sometimes called RF-echo tracking which explores a searching window in the echo from Frame 2 to locate the position of an echo pattern (orange window) that best correlates with that in Frame 1 (blue window in Method 1). The shift that maximises the correlation is the local displacement between these two frames ($\Delta\tau$). Method 2 (also called Doppler processing) correlates the same gated regions in both frames (two blue regions in Method 2) and the local displacement is estimated by repeating for several frames and finding the shift that

maximises the correlation coefficient ($\Delta\tau$) [16]. With either method, the displacement along depth (x-axis) can be then obtained by moving the window and finding the local displacement at each position. The size of kernel is usually chosen as a compromise between the imaging resolution (window size) and a good signal-to-noise ratio.

The displacement estimated is then processed to obtain the elasticity-related indexes. For example, in strain-based elastography, strain is displayed by calculating the gradient of the displacement along depth. Because stiff tissues respond differently (hard to deform) from soft tissues, the strains are different (small strain for stiff tissues vs. large strain for soft tissue) [17]; in shear wave-based (SW-based) elastography, the shear wave speed is quantified by tracking the displacement in time and space [18]. The shear wave speed is higher in stiff tissue than in soft tissue.

Tissue deformation and imaging methods

As mentioned previously, either a force or the shear wave can distort tissue.

For force-based deformation, several ways are used and can be categorized into two groups: external deformation and internal deformation. External methods utilise ultrasound probes to compress the surface of skin to deform the tissue beneath. Compression with ultrasound probes could be done by hand with either a single or a sequence of cyclic pressure and release movements. By tracking the displacement with cross-correlation methods during the distortion, strain is then found as the gradient of displacement (Equation 2-8) and displayed as an indicator of the tissue's elastic property. Figure 2.5 compares a conventional B-mode image of a heterogeneous phantom (a) with the registered strain elastography image created by compressing the phantom periodically with a hand-held ultrasound probe (b). The phantom was a tissue-mimicking phantom with a stiff inclusion buried and the

ultrasound scanner used was Esaote MyLab^{TM} Twice. The phantom was placed on an optical table and the elastography was generated by repeatedly compressing the phantom with an ultrasound probe. In the B-mode image, although vague boundaries can be observed around the inclusion (arrow), it is indistinct from surrounding medium, whereas in the elastography image, the inclusion is easy to identify. Furthermore, the colour map in the elastography image suggests that the inclusion has higher stiffness than the background, which is consistent with the known property of the phantom.

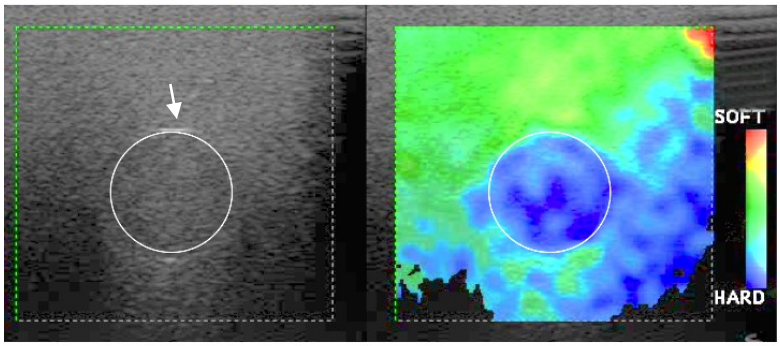

Figure 2.5 Comparison between (a) conventional B-mode image and (b) strain elastography

The image shown in Figure 2.5(b) is called strain elastography (SE) where the strain is displayed. Because the magnitude and direction of the applied stress is difficult to estimate, SE gives only the strain information which can characterise the tissue elastic property only when the stress is uniformly distributed within the region of interest. Therefore, it is important to keep the stress uniaxial and distributed homogenously within the tissue, such that the contrast of SE is influenced only by tissue elasticity. However, several factors could affect the distribution of the stress, such as the size of ultrasound probe [19] and the boundaries [20] in tissue. Figure 2.6 shows the simulated SE images for a heterogeneous phantom generated by the probes with

different sizes indicated by the arrows on the top of the images [16]. In Figure 2.6 (a) and (b) where the probe size is smaller than the imaging region, strain is concentrated below the probe and decays rapidly with depth, whereas Figure 2.6(c) shows a most homogenous strain distribution and a best contrast of image when the size of probe is larger than the imaging region. In another aspect, although the image in Figure 2.6(c) is better compared with (a) and (b), inhomogeneity can still be observed. This is caused by the boundary between the soft background and hard inclusion which leads to an increase of stress in the adjacent soft tissue and gives the cross-like strain distribution [21]. Besides, the boundaries in tissue also cause a low strain beyond boundaries, which could result in soft inclusions being obscured [22]. Another artefact is the hand-held generation of force, which is not stable and may lead to the noise, such as the noise in Figure 2.5(b).

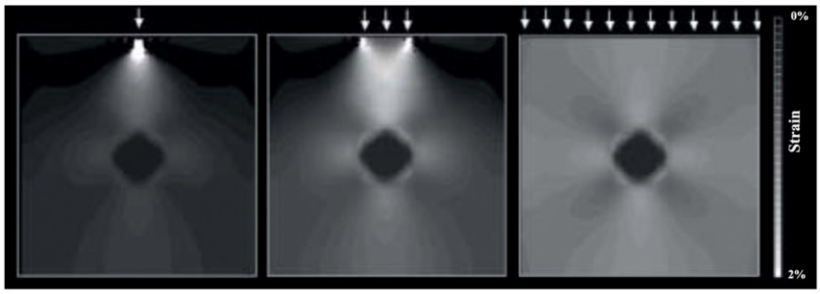

Figure 2.6 Effect of probe size in strain elastography [16]. The darker the grey, the smaller the strain.

SE was firstly described by Ophir and his colleagues in 1991, where they computed the tissue strain based on a cross-correlation analysis of pre- and post-compression with ultrasound probe [20]. During the next decades, from the studies of signal decorrelation [23, 24] to zero-crossing tracking [25], from the studies of strain increments [26, 27] to the estimation of the signal envelope with a two-dimensional window [28], major engineering efforts have been focusing on improving signal

processing and systems' implementation to increase the accuracy and signal-to-noise ratio of SE. Nowadays, SE have been proven in many clinical applications such as breast [29, 30] and thyroid [31, 32] malignant detections, and a few commercial machines are able to implement SE, such as Esaote, GE, Hitachi-Aloka, Philips, Siemens and Toshiba.

Strain Elastography can also be obtained using internal force deformations engendered by passive physiologically induced force (mainly cardiovascular) and acoustic radiation forces (ARF). The passive method is mainly used on the estimation of vessel wall elasticity, where the motion of vessel wall caused by pulsation is tracked [33]. Elastography obtained with the passive method is used in intravascular applications [34]. Compared with the passive force, ARF is a dynamic force that generated by the interaction of ultrasound and tissue. Specifically, ARF is a force resulting from the transfer of the momentum from ultrasound due to its attenuation along the propagation path [35]. The direction of ARF is along the direction of the ultrasound propagation and its magnitude (F) can be approximately described by [36]

$$\boldsymbol{F = \frac{2\alpha\langle I\rangle_T}{c}}, \qquad \textbf{(2-15)}$$

where the α is the acoustic absorption coefficient of tissue, c represents the speed of the sound in tissue, I is the intensity of the sound while $\langle \quad \rangle_T$ means the average within the time period T. Figure 2.7(a) portrays the geometry of a typical ARF field at 0.6 ms after stimulating a focused ultrasound pulse in tissue. The field was simulated by a finite-element method model where brighter pixels indicated greater magnitude of ARF [36]. As shown, the ARF maximizes at the focal region (around 20 mm in axial direction) of the ultrasound pulse where the power of ultrasound is the greatest. Figure 2.7 (b) and (c) plot the axial displacement of tissue along the two dotted lines

indicated in Figure 2.7(a), showing that tissue motion maximizes at focus region of the ultrasound pulse and decays rapidly outside. Therefore, ARF generated by focused ultrasound is regarded as a localized force that can locally deform tissues within its focal region.

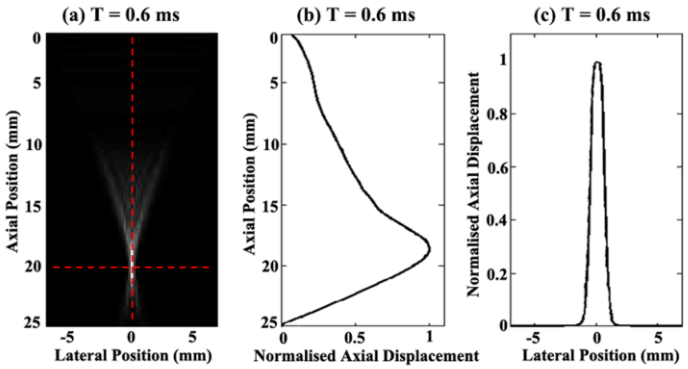

Figure 2.7 A finite element simulation of ARF at T = 0.6 ms after stimulating an ultrasound pulse. (a) Normalised displacement field with region of interest; (b) Normalised axial displacement along axial axis; (c) Normalised axial displacement along lateral axis. [36] Copyright © 2005, IEEE

In 1990, Sugimoto et al. was the first to use the ARF to deform tissue and acquried information on localized strain [37]. However, it was not until in 2002 when a technique called acoustic radiation force impulse imaging (ARFI) was devised [38], that the ARF method began to be appreciated. Utilizing the ARF by a transient pulse, ARFI produces strain elastography by scanning the ultrasound focus within the region of interest and tracking the displacement of tissue at each position [39]. Since the stress is also not easy to estimate in ARFI, it still gives only qualitative strain image. However, compared with the external methods, because it is the ultrasound beam that generates the displacing force, ARF is more uniaxial than the force created by hand. ARFI also shows better spatial resolution, suffers less from boundary effects and has higher SNR at depth compared with the external SE [40]. Nevertheless, because ARF is generated by the absorption of the ultrasound in tissue, the contrast of the image

depends on not only the mechanical property of the tissue but also on the absorption of ultrasound. In addition, the thermal effect induced by the absorption may also produce side effects, such tissue heating [41]. Other types of ARF-based elastography have also been developed, such as vibrao-acoustography (VA) [42] and harmonic motion imaging (HMI) [43] where oscillatory radiation forces were generated. In VA, the tissue is vibrated with a oscillatory radiation force generated using either two continuous ultrasound waves with slightly different frequencies that are transmitted simultaneously and focused at the same location or an amplitude modulated continuous burst. A hydrophone is used to detect the acoustic echoes emitted by the vibrating tissue which were then related to its mechanical properties. VA has been studied in several clinical situations, such as micro-calcification in arteries [44] and the breast [45]. VA may provide quantitative elasticity with an inverse problem approach [46], but this has only been demonstrated with solids immersed in fluids. In HMI, the displacement of tissue generated by an oscillatory radiation force is calculated as the signal for imaging, which may provide better contrast than the hydrophone signals [47]. HMI was used to visualize the thermal ablation created during focused ultrasound therapy [48] .

In summary, the force-based deformation can be external or internal. Strain is displayed as the elastic property of tissue. SE refers to the images of strain induced by static (or quasi-static) force while ARFI displays strain induced by the dynamic ARF. Compared with SE, ARF-based methods have advantages including better spatial resolution, deeper imaging depth and fewer artefacts at boundaries. However, all provide only qualitative elasticity measurement of tissues and a few factors other than elasticity properties influence the contrast of the images. Although effort has been

made to reconstruct the Young's modulus image based on numerical analysis [49-51], the accuracy is poor due to the high degree of heterogeneity of biological tissues [52]. Recently, shear wave elastography has been proposed, providing a quantitative measurement of tissue with shear wave propagation.

The generation of shear wave is closely related to the deformation of forces, externally or internally. Sonoelasticity imaging utilizes external vibrators to vibrate the surface of tissue with low frequency in order to generate shear wave propagating into tissue. The vibrating patterns of shear wave are measured with Doppler imaging to show the abnormalities in the tissue [53, 54]. Transient elastography (TE) uses an external mechanical piston driven by a pulse excitation (e.g. a single cycle of a 50 Hz sinusoid) to thump the tissue surface and generate the shear wave pulse in tissue. TE was firstly proposed by Catheline et al [55, 56] in 1999. By estimating the evolution of displacement in time with successive A-scans, shear wave speed was obtained as the slope of a straight line fitted to the arrival time of shear wave versus depth data. This method provides 1D information and requires the propagation of shear wave to be parallel with the A line. Sandrin et al [12, 57] improved TE into 2D by calculating the shear modulus with Equation 2-9. However, it is difficult for either Sonoelasticity imaging or TE to image at depth due to the attenuation of the shear wave when it propagates into tissue (especially in obese patients). The main method to generate shear waves at depth in tissue uses ARF which allows shear waves to be generated at the region of interest. Like the piston used in TE, ARF generated by an ultrasound pulse thumps tissues from within them and creates a transient shear wave.

Figure 2.8(a) shows axial displacement field of a transient shear wave at 10 ms after stimulating an impulse at the point indicated by the arrow in the figure. I calculated

the field based on an analytical model described in [58] with MATLAB. The shear wave speed was set as 2.5 m/s. The colours in the image indicate magnitude of displacement where the red represents a large displacement and blue a small displacement. The two curved coloured regions in the field are the positions of the shear wave wavefront at 10 ms after the impulse. Figure 2.8(b) plots the evolution of tissue displacement at a few points (4 mm intervals) along the lateral axis indicated in Figure 2.8(a). The y-axis is the normalised displacement and the x-axis is the time after the impulse. The propagation of the shear wave can be observed through the time delays of the peak displacement at each point. Meanwhile, the decreased amplitude of the peak displacement shows the attenuation of the shear wave during the propagation.

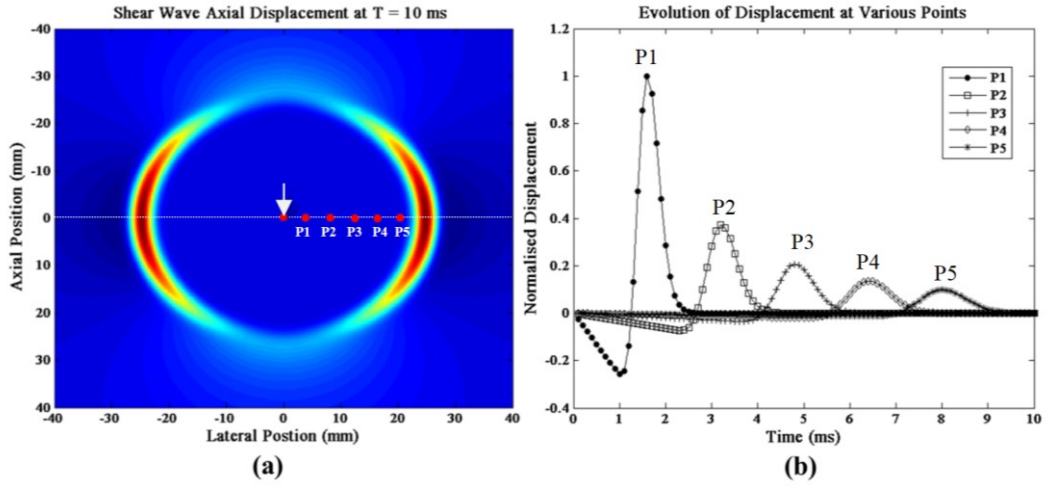

Figure 2.8 (a) Shear wave field at 10 ms after the ultrasound impulse; (b) Evolution of displacement at different points indicated in (a)

The use of ARF to generate shear wave in tissue was first demonstrated by Sugimoto et al [37] and more thoroughly described by Sarvazyan et al [18, 59]. In their work, shear wave generation was studied mathematically and the shear wave was detected with optical and magnetic resonance imaging systems in tissue-mimicking phantoms.

Further, Nightingale et al. [60] has demonstrated the generation and measurement of shear waves with ultrasound probes.

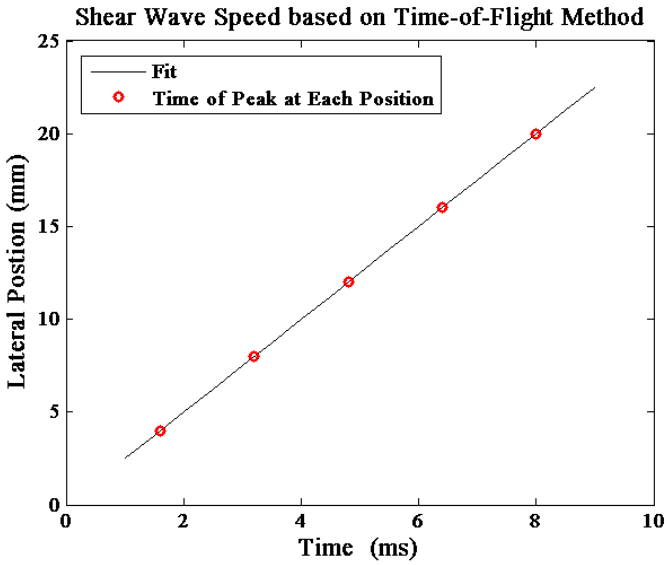

Figure 2.9 TOF method: linearly fitted time-to-peak data versus lateral position data (Simulation)

As mentioned in previous section, there are two ways to reconstruct tissue elasticity based on the shear wave propagation: wave equation inversion and wave speed. By measuring the displacement field of shear wave, the inversion method with the wave equation has been demonstrated for TE [12], while the wave speed method requires measurement of the shear wave speed. One way to measure the speed is a time-of-flight (TOF) method which traces the shear wave at several spatial locations along the direction of the propagation. By determining the arrival time of the shear wave as a function of spatial location along the propagation direction, the shear wave speed can be calculated. The arrival time of shear wave at a certain location could be accomplished by obtaining the time of either the peak displacement [61] or the leading edge of the shear wave wavefront [62]. The shear wave speed could then be calculated with, for example, the level set based inversion method [63] or the linear regression method [61]. Figure 2.9 illustrates the linear regression method based on

the displacement field in Figure 2.8. In the figure, the y-axis is the spatial position and x-axis is time. The red circles are the times of the peak displacement of the five locations shown in Figure 2.8. The solid line is the linear fit with a slope of 2.5 which is constant with the simulated speed of shear wave.

Both the inversion and wave speed methods have been shown to produce similar results in tissue-mimicking phantoms and tissue samples [60], but they suffer from different problems: the inversion method requires accurate displacement measurements in three-dimensions, which is problematic for conventional ultrasound imaging which only images within one tomographic plane. Additionally, it is sensitive to the noise in the displacement estimation which causes errors in the estimation of the shear wave speed. The wave speed method is not robust in heterogeneous tissues where the speed is deviated by the reflection of shear wave at boundaries within tissue. Compared with the inversion method, the wave speed estimator is more resistant to noise because the time/phase information is less sensitive to noise than the displacement. On the other hand, the wave speed method is simpler mathematically than the inversion method which needs to calculate the Laplacian and/or second derivative of the displacement field. For these reasons, the wave speed estimator is now more frequently used by assuming the homogeneity of tissue within the region of interest. ARFI quantification (ARFIq) is a TOF-based method that gives 1D elasticity information. It has been implemented on commercial systems by Philips and Siemens. Supersonic shear imaging (SSI) is another TOF-based method that can produce shear wave elastography within a 2D area in real time [58]. In SSI, the ultrasound focus is swept down along the acoustic axis faster than the shear wave speed to generate ARFs along the acoustic axis almost simultaneously. This produces a plane wavefront

(rather than the curved wavefront in Figure 2.8) which attenuates less and meets the assumption that the shear wave propagates exclusively along lateral axis at different depths compared with the curved wavefront from a point-like ARF. An ultrafast scanner achieving a frame rate of up to 20 kHz was developed and the shear wave is tracked in real time. Shear wave elastography with a cm-by-cm region can be then displayed with a frame rate of 3 - 4 Hz based on the TOF method. The resolution of SSI (1 – 2 mm) is a little worse than ARFI but it provides quantitative information. The SSI has been studied in several clinical situations, including breast lesions [64] and liver fibrosis [65, 66]. Crawling wave spectroscopy (CWS) generates two shear waves propagating towards each other and the slow-moving crawling wave that is generated between two shear wave sources is monitored. The speed of crawling wave is quantitatively related to the elasticity [67]. More recently, a method named spatially modulated ultrasound radiation force (SMURF) has been devised [68]. They set up a unique spatial frequency within a region of tissue by applying a spatially modulated ultrasound pattern. By measuring the temporal frequency of displacements, local shear wave speed was obtained. This method has been validated on a phantom and ex vivo porcine liver [69].

2.1.3 Viscoelasticity and visco-elastography

Viscosity is a measure of the resistance of a material to the deformation by shear stress and is related to both shear stress and its rate. In many studies, tissue is considered as purely elastic and the effect of viscosity is neglected. However, some biological tissues have the property of viscoelasticity that exhibit both viscous and elastic characteristics when undergoing deformation. The viscosity may have non-

negligible effects on the tissue responses.

A pure elastic tissue deforms linearly under the load and can quickly return to its original state once the stress is removed, while in a viscoelastic tissue, responses creep to the stress and lose energy during the compression and release phases. Compared with the linear relation between strain and stress in a purely elastic tissue, the strain and stress relation of a viscoelastic tissue is determined by both the elastic component and viscous component. The strain-stress relation for a pure elastic tissue or the elastic component of a viscoelastic tissue is given by

$$\boldsymbol{\sigma_{elastic} = \mu_1 \varepsilon,} \tag{2-16}$$

where σ is stress, μ_1 is elastic modulus and ε is strain. The strain-stress relation for the viscous component is expressed as

$$\boldsymbol{\sigma_{viscous} = \mu_2 \frac{d\varepsilon}{dt},} \tag{2- 17}$$

where the μ_2 is the viscosity of the tissue and $\frac{d\varepsilon}{dt}$ is the time derivative of strain. In one aspect, neglecting viscosity could cause bias on the elasticity measurement. Taylor et al. showed that the contrast of elastography degrades in liver tissue when the vibration frequency (and thus the time derivative of the strain) is increased [70]. Bercoff et al. studied the role of viscosity in a transient shear wave field induced by ARF and found a great difference between the shear wave fields generated in elastic and viscoelastic tissues [71]. In another aspect, since elasticity is not the only discriminant property for tissues, neglecting viscosity may cause loss of important information on the state of tissue [72, 73].

The measurement of viscoelasticity involves measurement of the dispersion of shear wave, that is, the frequency dependence of the shear wave propagation. When

considering a viscoelastic tissue, the shear modulus G is a complex value whose real part is called the storage modulus (μ') related to the elastic property while the imaginary part is called the loss modulus μ'' and is related to the viscosity. As a result, the wavenumber k is also a complex number based on 2-12 and it satisfies

$$\frac{\omega}{Re\{k\}} = v_s;\ -Im\{k\} = a_s, \tag{2-18}$$

where v_s is the speed of shear wave and a_s is the attenuation of shear wave.

The complex shear modulus G could also be obtained from rheological models that describe strain-stress relation in viscoelastic solid, such as the Maxwell model, the Kevin-Voigt model and the Standard Linear Solid Model. In tissue, the Kevin-Voigt model is mostly used because not only it is simple but also it fits better with tissue behaviour under shear waves [74]. In the Kevin-Voigt model, the stress $\sigma(\omega)$ and strain $\varepsilon(\omega)$ are connected as

$$\sigma(\omega) = \mu_1 \varepsilon(\omega) + i\mu_2 \omega \varepsilon(\omega), \tag{2-19}$$

where μ_1 is elasticity and μ_2 is viscosity. Hence, the complex shear wave G, which is the ratio of strain and stress, can be obtained as

$$G(\omega) = \frac{\sigma(\omega)}{\varepsilon(\omega)} = \mu_1 + i\mu_2 \omega. \tag{2-20}$$

Based on 2-18, by substituting Equation 2-20 into Equation 2-19, the relation of shear wave dispersion and tissue viscoelasticity is expressed as

$$c_s = \sqrt{\frac{2(\mu_1^2+\omega^2\mu_2^2)}{\rho(\mu_1+\sqrt{\mu_1^2+\omega^2\mu_2^2})}}; \tag{2-21}$$

$$a_s = \sqrt{\frac{\rho\omega^2(\sqrt{\mu_1^2+\omega^2\mu_2^2}-\mu_1)}{2(\mu_1^2+\omega^2\mu_2^2)}}. \tag{2-22}$$

The viscoelasticity (μ_1 and μ_2) of tissue can be then inversely obtained by measuring either the frequency-dependence of the shear wave speed (2-21) or the attenuation (2-22).

Experimentally, the shear wave speed at a certain frequency can be estimated with the phase change of a shear wave with ultrasound. Considering a simple 1D shear wave displacement field $u(x,t)$ in Equation 2-23

$$\boldsymbol{u(x,t) = ae^{i(\omega_0 t - kx)}}, \tag{2-23}$$

where a is shear wave amplitude, ω_0 is the angular frequency of the shear wave and k is the wavenumber. Given $k = k' + ik''$, Equation 2-23 can be re-written as

$$\boldsymbol{u(x,t) = ae^{i(\omega_0 t - k'x)}e^{k''x}}. \tag{2-24}$$

The Fourier transform of Equation 2-24 yields

$$\boldsymbol{U(x,\omega) = A\delta(\omega - \omega_0)e^{-ik'x}e^{k''x}}, \tag{2-25}$$

where the phase of the shear wave at frequency ω_0 at position x is

$$\boldsymbol{\varphi(\omega_0, x) = -k'x}. \tag{2- 26}$$

As a result, k' can be calculated by the ratio of $\varphi(\omega_0, x)$ and x, and thus the shear wave speed can be calculated with Equation 2-18 by substituting into k'which was calculated by the gradient of $\varphi(\omega_0, x)$ or the phase change at two positions separated by a known distance.

The study of viscosity measurement with ultrasound only started recently and not many methods have been investigated. The main two methods are shear wave dispersion ultrasound vibrometry (SDUV) and shear wave spectroscopy (SWS). SDUV [14, 75] combines the vibro-acoustography, to create monochromatic shear waves, with ARFI quantification, to track the shear wave propagation at several off-

axis positions. A shear wave with a certain frequency is produced by the oscillatory ARF generated either by two wave beams at slightly different frequencies or an amplitude modulated wave beam. Consequently, the shear wave speed is calculated by measuring the phase shift of two locations separated with a known distance. Applying the calculation over a range of frequencies, viscoelasticity is quantified by inversely solving Equation 2-22. SDUV has been used to estimate the shear wave speed in blood vessels[76], kidney tissue [77] and the prostate [78]. As an extension of SSI, SWS generates a quasi-plane shear wave and applies Fourier transforms to the propagating shear waves to evaluate the phase as a function of frequency [79]. Using the SSI system, SWS can estimate the shear wave speed dispersion much faster than SDUV which used a conventional probe whose frame rate is around one percent of the SSI system.

2.1.4 Summary

Table 2-1 gives a summary of ultrasound based elastography methods. As seen, ultrasound based elastography has been intensively studied and various methods have been proposed. Many of these, such as SE, SSI and ARFI, have been integrated into commercial ultrasound machines and are used for clinical examinations on liver, breast, thyroid, lymph nodes and elsewhere [1]. However, the quantification of tissue mechanical properties still has space to explore, especially regarding the viscosity, anisotropy and their changes in disease that have only recently been estimated. Furthermore, the integration of mechanical property measurement with other tissue property (e.g. optical property) measurement has a great potential as an advanced diagnostic tool for cancer and other diseases.

Table 2 - 1 Summary of ultrasound based elastography methods

Method	Name	Location of applied force	Method to apply force	Type of force	Measurement	Viscosity
Force-based on-axis measurement	SE	External	Probe	Quasi-static	Strain	No
		Internal	Passive force	Quasi-static		
	ARFI	Internal	ARF	Transient		
	VA[1]	Internal	ARF	Harmonic		
	HMI	Internal	ARF	Harmonic		
Shear wave - based off-axis measurement	TE	External	Piston	Transient	Shear wave speed	
	ARFIq[2]	Internal	ARF	Transient		
	SSI	Internal	ARF	Transient		
	CWS	Internal	ARF	Harmonic	Crawling wave speed	
	SMURF	Internal	ARF	Transient	Shear wave speed and wavelength	Not known
	SDUV	Internal	ARF	Harmonic	Shear wave speed and frequency	Yes
	SWS	Internal	ARF	Transient		

1.VA = Vibro-acoustography; 2.ARFIq is also called SWEI in the literature

2.2 Optics-based elastography (Opto-elastography)

As an alternative modality to characterise tissue, optics-based elastography has three main advantages compared to ultrasound elastography:

(1) Multi-mode measurements. Optics-based elastography can measure not only the mechanical properties of tissue but also its optical properties. As changes in the mechanical properties of tissue have not been proven to be a discriminant indicator for diseases, examining both properties could improve the sensitivity and specificity;

(2) High mechanical sensitivity. Light is sensitive to sub-nanometre displacement which enables the measurement of very small changes in mechanical properties;

(3) High spatial resolution. The high spatial resolution refers to the resolution of optical coherence elastography (OCE) which is a few micrometres and 10-100 times

better than the resolution of ultrasound elastography. However, because light is heavily scattered in biological tissues, optical resolution depends on the imaging depth, e.g. OCE can only image within 2 mm. There is a compromise between the resolution and imaging depth for optics-based elastography.

At the surface, OCE measures the tissue elastography with optical coherence tomography (OCT) which is an interferometric imaging method that utilises broadband light to obtain precise three-dimensional reconstruction of the scattered medium with micrometre-resolution [80, 81]. OCT imagimg is similar to the ultrasound imaging where the intensity indicates the reflectivity profile of the sample and hence depends on tissue structures. The applications of OCT are mainly in ophthalmology [82, 83] and cardiology [84-86] and clinical systems are commercially available. The application of OCT in the field of elastography is a relatively recent development. Schmitt [87] demonstrated the feasibility of measuring displacement with OCT in pork meat and intact skin in 1998, where he used a cross-correlation method to track the displacement of tissue under compression. OCE has not been widely studied before the development of new OCT techniques which dramatically increase the accuracy of measuring displacements [88]. The principle of OCE is similar to that of ultrasound elastography, where elasticity is related to the displacement induced by forces or wave propagation externally or internally in the tissue. Compression OCE includes external mechanical compression and internal ARF compression. The compression in OCE is similar to the SE or ARFI in ultrasound elastography, and thus, it is a qualitative method measuring the relative change of strain under compression. In ultrasound elastography, ARF compression is better than external compression because ARF can generate a localised force (depending on the

focal region) deep in tissue (depending on the focus position) to estimate tissue properties at depth. However, these advantages are limited in OCE, as its working depth is very small (1-2mm) and the resolution (10s μm) is an order of magnitude better than the ultrasound focal region. Swept-Frequency method [89] is a newly developed variant of compression OCE where the deformation frequency sweeps from 20 Hz to 1000Hz. The swept-Frequency OCE can not only measure relative strain changes in tissue but also the mechanical resonances which potentially identify different tumours [90]. Surface acoustic wave (SAW) OCE is a quantitative method in which the SAW velocity is related to elasticity [91]. SAW is an acoustic wave propagating along the surface that can be generated by an external vibrator [92, 93] or the thermoelastic expansion by light absorption [94]. The main advantages of SAW over compression OCE are the ability to quantify elasticity and the non-contact generation of the wave [94, 95] whilst the disadvantage is the resolution (500 – 1000 μm) which is worse than compression OCE. Shear wave (SW) has also been proposed for OCE [96]. However, due to the imaging depth of OCE, a key problem is to differentiate SW and SAW, especially when using an external vibrator which is also used to generate SAW in SAW OCE [97]. SW OCE is still in the very early stage of development and it remains to be seen whether shear waves can be utilised effectively in OCE. There are also other methods being developed, such as the magnetomotive method [98, 99] which employs magnetic nanoparticles in tissue and produces localised displacement by using an external magnetic field. In general, OCE attracts increasing interest and is becoming a rapidly developing application for OCT techniques.

There are few studies investigating the optics elastography in the depth of tissue. The

needle OCE measures the deformation induces by inserting needle with OCT [100]. It can measure deep tissue with high resolution but is invasive and needs more investigation. Transient opto-elastography (TOE) was proposed by Bossy et al [101]. It utilises ultrasound modulated optical tomography (UOT, reviewed later) to sense the propagation of shear wave in deep tissue by calculating the autocorrelation of the UOT signal. They found that the decorrelation of the UOT signal was related to the properties of the phantoms - the decorrelation coefficient started to decrease at the boundary of a stiffer inclusion while it decreased within an optical absorber after the boundary of the absorber. TOE provides a noninvasive way to measure elasticity in deep tissue. However, TOE is qualitative and its sensitivity to mechanical change is unknown. There is a need for a quantitative opto-elastography to noninvasively measure tissue mechanical property at depth.

In summary, optics-based elastography, especially OCE, has been studied recently. OCE can achieve high resolution elastography but its imaging depth is limited to 1-2 mm. Some studies showed promising results on deep tissue opto-elastography, but they are either invasive or qualitative. There is a need for a new method that can noninvasively quantify mechanical and optical properties in deep tissue and this is the objective of my research.

2.3 Ultrasound modulated optical tomography (UOT)

In order to develop deep tissue opto-elastography, ultrasound modulated optical tomography (UOT) was used in my research. UOT is a hybrid technique that combines optics with ultrasound and promises to improving optical imaging resolution in deep biological tissue. It aims to maintain the advantages of optical imaging while utilizing the excellent the resolution of ultrasound (US) at depth. In

UOT, an ultrasound wave is used to focus into a specific part of tissue where a high coherence laser beam passes through and is modulated by the US wave. Detection of these modulated photons enables the measurement of tissue properties within ultrasound focal region. As a result, the contrast of UOT is based primarily on the optical properties of biological tissue while the resolution of UOT is determined by the US focal region which is typically at the order of sub-mm in the lateral direction and mm axially. UOT differs from photoacoustic which uses light to generate acoustic waves that consequently detected by an ultrasound transducer [102].

Intense effort has been made to improve UOT by improving the ultrasound excitation schemes, or by the innovation of the laser emission schemes and/or by increasing the optical detection sensitivity using different detection methods. Meantime, researchers have also made great effort in studying the physical theories behind UOT techniques, which helps to form a deeper understanding of UOT. The following content is an overview, including the mechanisms of ultrasonic modulation of optical signals, the modelling and simulation methods for UOT and the experimental systems that have been designed to detect ultrasound modulated light. Afterwards, the UOT system used in my research is introduced and investigated.

2.3.1 UOT Overview

Figure 2.10 illustrates a basic UOT system consists of three parts: a light source (laser), an acoustic source (ultrasound) and a light detector. The light source is usually a laser with long coherence length and high power in order to obtain a clear speckle pattern after the propagation of light in tissue. The US beam is traditionally perpendicular to the optical axis and focused within the tissue to produce local

modulation. The optical detector is normally aligned with the laser and located at the other side of the tissue. There are also reflection-detection [103] and side-detection [104] geometries which may be used to detect signals from very thick tissue that light cannot penetrate.

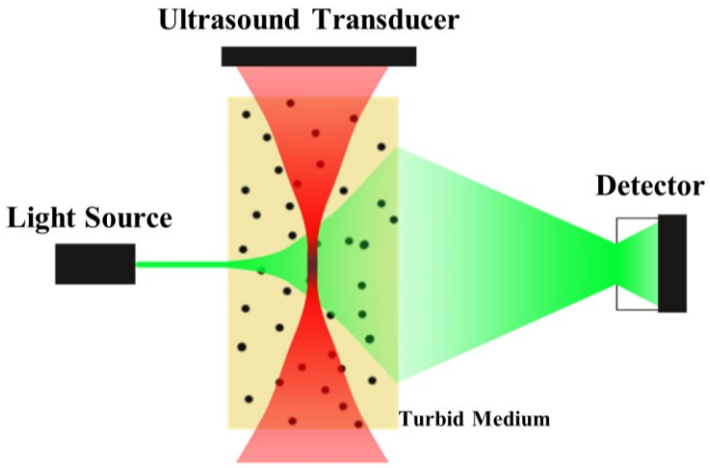

Figure 2. 10 A typical UOT system

Two mechanisms have been recognised as the origin of the ultrasound modulation of coherent light: optical scatterers displacement and change in optical refractive index. Both factors will modulate the path and thus the phase of photons are modulated [105]. Ultrasound could also modulate light with a low coherence by modifying the density of samples as propagating. However the modulation is small and hard to detect [105]. As shown in Figure 2.11 (a) and (b), when ultrasound is focused into tissue it causes a periodic compression and rarefaction of the tissue that will vary the local refractive index and change the position of scatterers. Due to these two effects, the optical path lengths ($L_{light} = nL$, where n is the refractive index of the medium and L is the travel distance of the light in the medium) are periodically changed, causing the modulation of the photon phases ($\sigma_{ph} = 2\pi L_{light}/\lambda_0$, where λ_0 is the wavelength of light in vacuum). When detecting the light, an intensity pattern (black and bright

speckles, e.g. Figure 2.) resulting from the interference among different photon paths will form on the detector surface. The phase modulation of the photons subsequently results in the fluctuation of individual speckle intensity which is correlated with the US wave (Figure 2.1(c)) and the acoustic sidebands at both sides of the optical central frequency (Figure 2.1(d)), both of which could be utilised to measure the tissue properties within the US focal region. An analytical model [106] and a Monte Carlo based analytical model [105] have been developed by Lihong V. Wang et al. to model these two mechanisms, which contributed greatly to the current understanding of the physical principles behind UOT. Many updated results have been published following their work. For example, Wang and his group extended their analytic study to pulsed US excitation [107] , non-uniform continuous US excitation [108] and non-uniform pulsed US [109] excitation instead of pure continuous US stimulation, which provided further insight into the effect of US parameters on the optical modulation. The analytical model is discussed in detail and adopted to my opo-elastography system in Chapter 4.

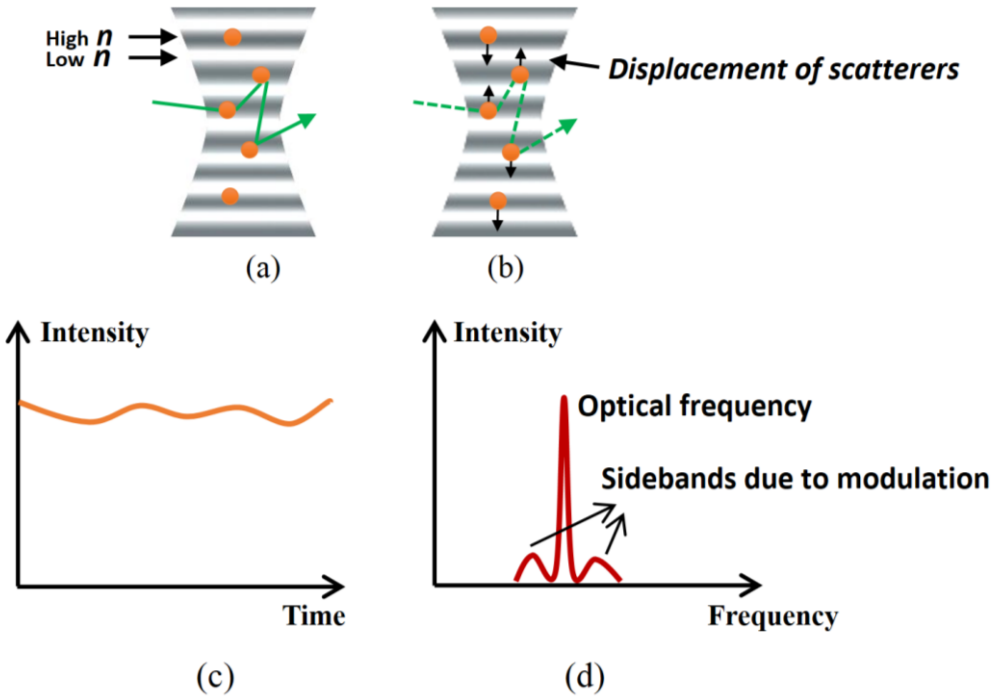

Figure 2.11 (a) Mechanism I: Refractive index (*n*) variation. The green arrows indicate the path of photons, and the grey stripes mean a high *n* while the white stripes for low *n*, which caused by the propagation of ultrasound. (b) Mechanism II: Displacement of scatterers. The black arrows indicate the displacement of the scatterers due to the ultrasound wave. (c) Optical intensity fluctuation with the frequency of the ultrasound wave and (d) the frequency spectrum of the modulated light. Due to the ultrasound modulation, the optical frequency of modulated photons is shifted by ultrasound frequency (sidebands) from the original frequency (optical frequency). The scale of the sidebands depends on the portion of photons that is modulated.

In Figure 2.11(c), an AC signal (fluctuation) and a DC signal (offset) can be observed. The AC signal is due to the ultrasound modulation and the DC signal comes from the unmodulated light. The ratio of these two signals, which is called modulation depth, is usually used as the UOT signal to represent the tissue property. Early detectors used a single element detector to detect the speckle pattern and calculate the modulation depth [110, 111]. Because the phase of the modulated speckles is random and thus the spatial averaging of the speckles could cancel the modulation, leading to the decrease in modulation depth, an iris is usually positioned in front of the detector to match the detector size with one speckle, such that the modulation depth is maximised.

However, since the modulated photons spread over the whole volume of light and exit the tissue in random directions, detecting only one speckle loses useful signals whose proportion is already low because of the small size of the US focus compared with the large illuminated volume in tissue. Therefore, the detected signal by one speckle could be overwhelmed by the shot noise carried by the unmodulated light. One way to improve this is to remove the unmodulated light, based on the spectral feature of signal (Figure 2.11(d)). Since the modulated light is frequency-shifted by the ultrasound compared with the unmodulated light, a Fabry-Perot interferometer [112] was proposed to filter out the unmodulated light and leave only the modulated light to be detected by the detector. The Fabry-Perot interferometer method works efficiently when using high frequency of ultrasound, sacrificing the imaging depth [112, 113]. An alternative technique, the spectral hole burning method [114] was proposed recently to work with lower ultrasound frequency. It used a spectral hole-burning crystal to transmit the modulated light and absorb the unmodulated light by exciting the crystal with ultrasound frequency-shifted light, causing saturation and relative transparency to the modulated light afterwards. As a new method, it needs more exploration. Another way to improve is to unify the phase of modulated light so that a large detector can be used (averaging speckles will not cancel the modulation). This can be done with photorefractive crystals [115, 116]. A photorefractive crystal can record the wavefront of the signal exiting the tissue by changing their refractive indexes. As a result, a reference beam passing through will have the same wavefront as the signal, while the random phases presenting in the signal disappear. Consequently, a detector larger than one speckle may be used to detect more modulated photons. The problem with this method is that the modulation from other

motions, such as Brownian motion and pulsation will affect recording of the wavefront, causing bias in the detected signal.

Instead of single-element detection, multi-element detectors, such as charge-coupled device (CCD), were proposed to detect more speckles. The signal-to-noise ratio increases as the square root of the number of the elements employed. However, the frame rate of a multi-element detector or CCD is not fast enough to directly detect megahertz modulation. Hence, various schemes have been proposed to detect the modulated light. The simplest scheme is to analyse the spatial statistical properties of the speckle. If the scatterers in the tissue are stationary, the speckle pattern on the CCD is stationary. If the scatterers move, the speckle pattern on the CCD moves, causing a blur on the final image. The degree of blurring can be quantified by the contrast of the image which is correlated to the modulation depth [117]. Parallel lock-in detection [118, 119] is an alternative approach where laser light is modulated at the same frequency of ultrasound and four images are captured for different phases between the laser and ultrasound. The modulation depth is then calculated from these images for each pixel. Heterodyne parallel speckle detection [120] uses a reference beam whose frequency is shifted by the ultrasound frequency to amplify the intensity of the signal without any background amplification. The modulation depth is calculated from four images for different phases between the reference beam and the signal. Compared with single element detection, parallel speckle detection intrinsically has higher SNR, but it suffers from the speckle decorrelation caused by other motions in tissue, such as pulsation and Brownian motion due to a long acquisition time, especially for the parallel lock-in and heterodyne detections where four images are required. The laser speckle approach has an advantage over the other

two approaches because it needs only one image and thus the speckle decorrelation may be reduced. Also, the experimental set up for the laser speckle approach is the simplest as it requires no filter or extra reference beam. This method is the basis of my research and is introduced in next section.

Besides the investigations on the detection techniques, there are explorations on the emitting of either the ultrasound or the laser to increase the light modulation. Most UOT systems use focused US transducers because the focused US can provide larger intensity at the focal zone and give a better lateral resolution compared with the unfocused ultrasound. In the early stages, continuous wave (CW) US was used to modulate the light. This gives little information on the location of objects coupled along the US penetration axis [121]. To address this problem, pulsed US waves [122] were proposed to modulate the light, such that the axial resolution is determined by the length of the pulsed US wave. However, due to the broad frequency spectrum of the pulsed US, an advanced detector sensitive to a wide bandwidth of frequency is required. As a compromise, Zemp et al. [123] used acoustic burst in the UOT system, allowing greater US intensity to be achieved compared with the CW US with a narrower bandwidth compared with the pulsed US. In the meantime, they also found that acoustic bursts can generate acoustic radiation force (ARF) which generates larger particle displacements (several micrometres) compared with the pure US modulation (nanometres). Li et al. [124, 125] continued these investigations and found experimentally that ARF can enhance the modulation. Li's work is the basis of my research and is introduced in the next section. A study on the laser aspect has also started recently by Rousseau, G et al [126]. The laser power has a safety limit to avoid tissue burn while high laser intensity is supposed to enhance the modulated signal and

penetration depth. Rousseau et al. use a flashlamp-pumped chamber to produce a pulsed laser source with a high peak power but low average power. Utilizing the pulsed laser source and photorefractive crystal, they detected modulated photons in a 60-mm thick scattering medium. More advanced methods to increase the modulation signal includes time-reversed light focusing [127] which has been demonstrated in a 90-mm tissue mimicking phantom.

To conclude, UOT is a novel imaging technique that has the potential to optically image tissue with US resolution. Although it is still in its early stage, many studies have shown its ability to image tissues at depth. In this thesis, by using UOT, I studied the possibility to obtain both mechanical and optical properties at ~cm depth within tissue-mimicking phantoms.

2.3.2 Ultrasound modulated optical tomography with laser speckle analysis

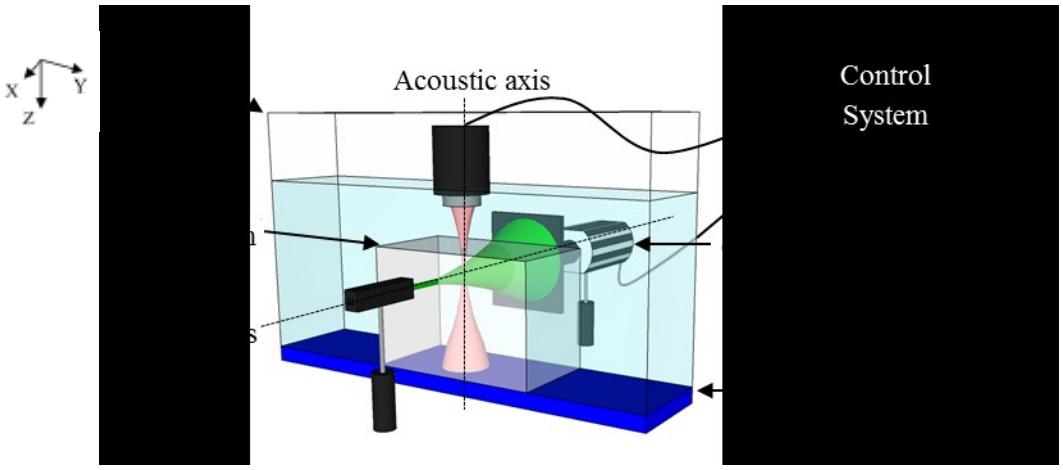

Figure 2.12 Experimental set up. Laser and CCD camera are position along the optical axis. The oblongs below them are their holders. US is perpendicular to the optical axis and propagates from the top. The ultrasound focus is aligned with the optical axis in the phantom. The acoustic absorber below the phantom absorbs the transmitted ultrasound, preventing the reflection. For clarity, the motorised slide beneath the water tank is not shown.

Previously, Li et al. at Imperial College London developed an ARF-UOT system

which could improve the optical contrast compared with the pure ultrasound modulated optical tomography. The first part of this section is an introduction to our ARF-UOT system. The second part is a study of laser speckle, demonstrating its ability to track motion. These two subjects are fundaments of my research.

ARF-UOT system

Figure 2.12 shows the configuration of our UOT system. A tissue mimicking phantom is fixed in a water tank made from Perspex. The Perspex is transparent to light so it will not affect the light propagation before and after the phantom. The phantom is made of agar and intralipid which will be described in next chapter. A 532 nm Nd:YAG laser (Excelsior 532, Newport Inc., Irvine, CA) illuminates the phantom horizontally while a CCD camera (Qimaging Retiga EXi, Surrey, BC, Canada) is aligned to detect the scattered light on the other side of phantom. In order to match the speckle size with CCD pixel, an iris (Ø 0 – 12 mm, Thorlabs) is placed in front of the camera (as will be explained later). Ultrasound is generated by a focused single element transducer (Central frequency = 5 MHz, Aperture = 1'', Focal length = 1.96'', Panametrics NDT Videoscan 307, Olympus, Essex, UK) and propagates vertically towards the bottom of the tank. The acoustic axis crosses the optical axis at a right angle and their intersection is within the focal region of ultrasound which is measured with a hydrophone as 1 mm laterally and 10 mm axially. An acoustic absorber is positioned beneath the phantom to absorb the ultrasound that passes through and thus avoid reflections from the bottom of the tank. The focal length of the transducer is about 4.55 cm, resulting in a gap between the upper surface of the phantom and transducer. To minimise the acoustic mismatch, the tank is filled with degased water

to immerse both the phantom and transducer. There is a motorised slide under the tank (not shown in the figure), which can move the tank with a resolution of 2.5 μm. By moving the phantom and thus the focus of ultrasound, the slides can make 1-dimensional (1D) or 2-dimentional (2D) scans of the phantom. In addition, the whole system is placed on an optical table to minimise external motions.

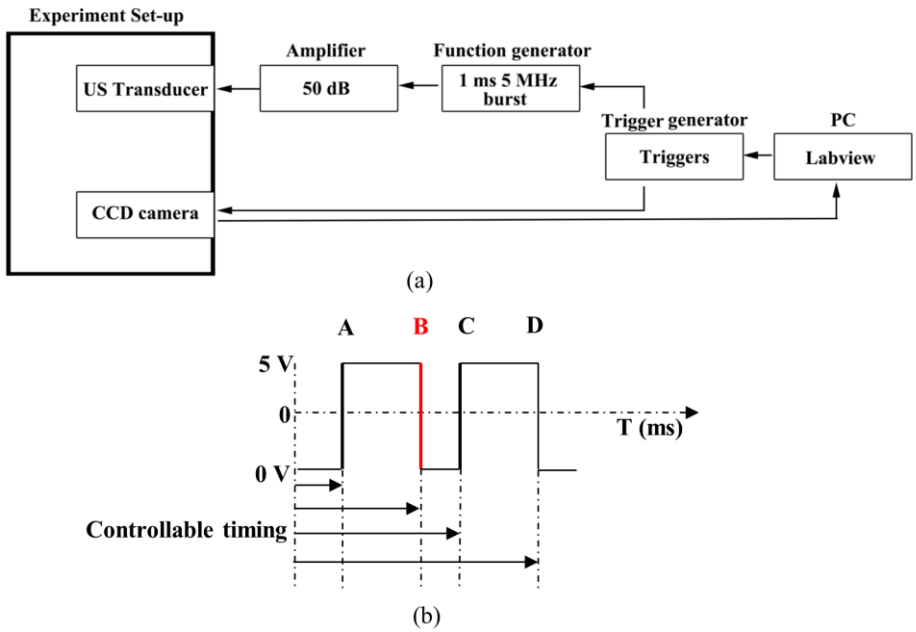

Figure 2.13 Control system. (a) Illustration of the system where the transducer and the camera are synchronised by the delay generated controlled by the PC. (b) The control wave generated by the delay generator where the rising edges were used to trigger the CCD while the falling edge B was to trigger the function generator.

The control system is shown in Figure 2.13 (a), consisting of a function generator (Agilent 33220A, South Queensferry, West Lothian, UK), an amplifier (ENI, Inc., 240L, Rochester, NY, USA), a delay generator (DG535, Stanford Research, Sunnyvale, CA, USA) and a PC. The ultrasound transducer is linked to the amplifier and function generator - the amplifier has a fixed amplification factor of 50 dB for a 5 MHz wave and the function generator controls the amplitude and shape of the waves that are sent to the transducer. The CCD acquisition and function generator are synchronised by a delay generator controlled by Labview in a PC and the recorded

images are transferred back to the PC for post-processing. The control of the laser is not shown in the figure because the laser is a continuous laser and switched on manually before the CCD acquisition. The synchronization of the transducer and the CCD is accomplished by sending triggers with the trigger generator.

In UOT (Figure 2.13(b)), two cycles of bursts with controllable burst length and duty cycle were sent, where rising edges triggered the CCD to expose and falling edges triggered the function generator and thus the transducer to transmit ultrasound. As a result, the CCD will obtain an image (triggered by the first rising edge *A* in Figure 2.13(b)) before the ultrasound (by the falling edge *B*) and another image (second rising edge *C*) after the ultrasound. The falling edge D is not used in UOT but it is essential to trigger the delay generator to return to the initial level. The timing of each edge (arrows) can be controlled by Labview via the delay generator. Due to isolation from external motion by the optical table, the speckle decorrelation is negligible in the phantom study. The timing of edge A and C are thus flexible. In the future, when the system is studied in *in vitro* or *in vivo* situations, this needs to be minimized to reduce the effect of the speckle decorrelation.

In addition, apart from the advantage of ARF-UOT over other UOT methods where light is modulated by pure ultrasound, the ARF-UOT system could be sensitive on both optical and mechanical contrasts.

Figure 2.14 shows the UOT result for a heterogeneous phantom from Li's paper [125]. There were two inclusions in the phantom, one was a mechanical inclusion whose stiffness was higher than the surrounding phantom but had a similar optical absorption, the second was an optical inclusion whose optical absorbance was higher but the stiffness was similar. The thickness of the phantom was 22 mm and the

ultrasound was focused within the middle layer of phantom whose depth was about 11 mm viewed from the laser. Figure 2.14(a) is a picture of the scan layer where the optical inclusion appears darker than the background and the mechanical inclusion is indicated by a red circle.

(a)

(b)

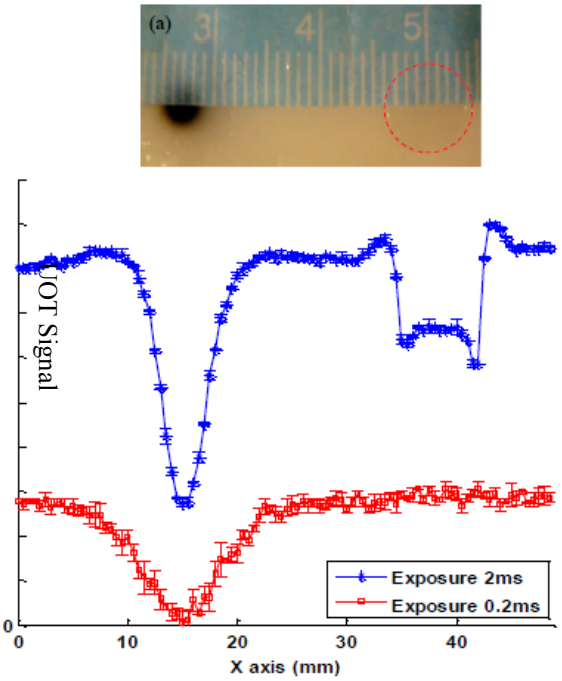

Figure 2.14 (a) a picture of a cross-section of the phantom. The black area is the optical inclusion whose optical absorption is higher than the background while the stiffness stays the same. The red circle indicates the mechanical inclusion who is stiffer than the background while has the same optical property. (b) UOT 1-dimensional scan signal with different exposure times. The two curves are obtained by changing the CCD exposure time. The signal increases by increasing the exposure time which captures ARF modulation. And the short exposure time (red) seems less sensitive on the mechanical contrast. [125]

Figure 2.14(b) shows the 1D scan result by moving the water tank and phantom with 1 mm steps while the light, CCD and transducer were fixed. The x-axis shows the different steps of the water tank and hence the lateral position of the ultrasound focus. The y-axis is the UOT signal which alters with the intensity of the modulated photons (detail of how the UOT signal was obtained is explained later). In the figure, two curves were obtained with different CCD exposure times. A short exposure time, such

as 0.2 ms, captures only the pure ultrasound modulation while a long exposure time captures the ultrasound and ARF modulations. Therefore, the blue curve indicates UOT signal from both modulations and the red shows the ultrasound-only modulation. There is an obvious increase in the UOT signal by utilising the ARF. Furthermore, the results shows two troughs when the long exposure time was used but only one trough with the short exposure time. This demonstrates that the UOT can be sensitive to both mechanical and optical contrast, which inspired us to further investigate the feasibility of quantification of the mechanical and optical properties with UOT.

Laser speckle analysis

When a laser beam illuminates a turbid medium a laser speckle pattern can be formed on detector. The speckle pattern is an intensity pattern produced by the interference of many waves of the same optical frequency but different amplitudes and phases. Due to the random scattering and thus the random phases of light, the speckle pattern appears as a granular pattern consisting of many randomly distributed bright and dark speckles as shown in Figure 2.15(a). The speckle pattern can be observed both in free space (without a lens in front of the detector) and in an imaging geometry (with a lens). UOT observes the speckle pattern in free space and there is no lens between the exit of light from the tank (called exit facet) and the CCD camera. The light at a given point in the speckle pattern could be contributed by the light from the whole exit facet. Consequently, the speckle pattern imaged contains no local information about the speckle pattern on the exit facet. On the contrary, if a lens is put between the light and the CCD camera, a speckle image of the exit facet can be formed on the CCD. The light at a given point in the speckle image is contributed by the corresponding

point in the exit facet and thus can reveals the local movement.

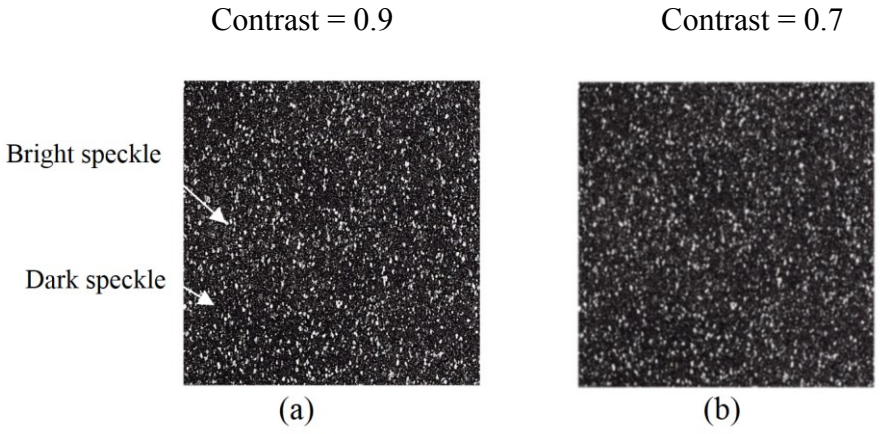

Figure 2.15 Speckle patterns formed on a CCD camera in free space geometry. (a) Speckle pattern without ultrasound and (b) pattern with ultrasound.

Speckle is considered as noise in some applications, such as Laser television where the speckles affect the smoothness of the displayed images, and in ultrasound images where the speckles are not correlated to underlying structures, but in UOT they carry information on the ultrasound modulation and are vital to extract useful information from these speckles to measure the ultrasound modulation. The method of using the contrast of the speckle pattern as a metric for the ultrasound modulation was proposed by Li et al [117]. The contrast of a speckle pattern is defined by

$$\boldsymbol{C = \frac{\sigma_{sp}}{\bar{I}}}, \tag{2-27}$$

where σ_{sp} is the standard deviation of speckle intensity and $\bar{I}$ is the spatial mean of the intensity. A speckle pattern captured by a CCD camera with a certain exposure time can be regarded as a superposition of serial instantaneous speckle patterns. Due to the movement of the optical scatterers caused by ultrasound, the instantaneous speckle patterns fluctuate and the superposition of these instantaneous speckle patterns will result in blurring and hence a reduction in the contrast of the final

speckle pattern. Figure 2.15 is a comparison between the speckle patterns before (a) and after (b) a 1 ms ultrasound burst. With the ultrasound modulation, Figure 2.15(b) looks more blurred than (a) and its contrast is reduced by 0.2 compared with (a). In UOT, the contrast difference ($\boldsymbol{\Delta C}$, Equation 2-28) of the speckle pattern before (C_b) and after (C_a) the modulation is often used as the signal and an indicator for the ultrasound modulation – large contrast difference usually means large modulation. Moreover, the subtraction helps reduce system fluctuations such as light intensity drifts. As a result, as shown in Figure 2.13(b), two rising edges controlling the CCD exposure were generated to enable the capture of two images before and after the ultrasound burst which is controlled by the falling edge between the two rising edges.

$$\Delta \boldsymbol{C} = \boldsymbol{C_b} - \boldsymbol{C_a}. \quad \textbf{(2- 28)}$$

In addition to the ultrasound modulation, there are other factors influencing the contrast difference, including CCD exposure time, other motions such as Brownian motion and external vibrations, speckle size and detected intensity.

Figure 2.14 shows an example of the influence of CCD exposure time on the contrast difference (as the left part of the curves). Comparing the contrast difference of the two different exposure times, a longer exposure time (blue) obtained a higher signal than a short exposure time (red). Motions could also change the contrast difference in the same way as the ultrasound does, where they both add modulation into the signal and result in the reduction of the speckle contrast. The motions such as Brownian motion and external vibrations are noise in the UOT and need be minimised. A way to reduce the noise is to subtract the background contrast from the modulated contrast, such that the modulation by the noise may be cancelled out. Another possible way is to use a short exposure time at the expense of SNR. In my study, I used exposure times

between 1.5 and 2 ms as a compromise between the signal SNR and the decorrelation. The speckle size is an important parameter in the experiment as the CCD is used to detect the speckle pattern. The CCD is a spatially discrete sampling device, so the sampling criterion cannot be ignored. In order to maximise the signals, the speckle size should to be at least twice as large as a CCD pixel size based on the Nyquist sample theorem. However, as the speckle size increases the detected area on the observed plane decreases. To optimise the detection, the speckle size is normally twice as large as the pixel size.

In Figure 2.15, the values of the contrast was calculated globally by finding the standard deviation and the mean of the speckle intensity of the whole speckle image and a single contrast value was obtained (above the figures), presenting the averaged modulation of penetrated light in the exit facet. The contrast could also be calculated locally within a small window. By moving the small window across the whole image, a contrast image could be obtained. Each contrast value in the contrast image corresponds to a local modulation in the exit facet. In UOT, when the ultrasound focus is positioned within the phantom (as in Figure 2.12), modulated light on the observed plane distributes randomly due to the random scattering of photos. Therefore, the exit facet has no local information about the ultrasound modulation and a speckle pattern is detected in a free space (without a lens) and a global contrast is calculated. This situation was adopted in following chapters where I developed a dual mode UOT system for use at depths in the tissue. However, if the ultrasound is focused in the back surface of the phantom (or the phantom is light-transparent), modulated light on the exit facet contains the local modulation corresponding to different spatial parts of the ultrasound beam since there is no further scattering after the ultrasound

modulation. Therefore, a contrast image may be generated with an imaging geometry (with a lens) to characterise the ultrasound beam and also the corresponding shear wave. In the next chapter, a UOT system with an imaging geometry is studied to visualise the ultrasound modulation and the propagation of shear wave generated by ARF in a special designed phantom, which is not only an alternative application for UOT but also a preparation for the dual mode UOT at depths in the phantom.

2.4 Summary

In this chapter, a thorough literature review related to my study has been made. The current status of opto-elastography gave me the motivation of developing an opto-elastography system for use at depths. Ultrasound elastography provided me the guidance for its development, while the ARF-UOT made the detection of ultrasound and shear wave modulations at depths in the tissue possible.

In the subsequent chapters, by improving and modifying the current UOT system, I developed a dual-mode UOT system that detected both mechanical and optical properties of samples. Chapter 3 is an investigation of the ability of the UOT to detect ultrasound and shear wave modulations at the surface of a phantom with an imaginary geometry (with lens). It not only proposes an alternative way to map an ultrasound field, but also allows me to better understand the UOT system and laser speckle contrast analysis. Chapter 4 contains the development of an opto-elastography system to measure the elasticity of tissue mimicking phantoms. Chapter 5 shows a dual-mode UOT system that can be sensitive to both mechanical and optical properties of phantoms. Chapter 6 presents an investigation on measuring the viscosity of the phantom with the opto-elastography system, including both experimental and simulation results. Finally, Chapter 7 is a summary and discussion of my study.

References

1. D. Cosgrove, et al., *EFSUMB Guidelines and Recommendations on the Clinical Use of Ultrasound Elastography.Part 2: Clinical Applications.* Ultraschall in Med, 2013. **34**(3): p. 238-253.

2. Lin, P.C., *Optical imaging and tumor angiogenesis.* Journal of Cellular Biochemistry, 2003. **90**(3): p. 484-491.

3. Tang, M.X., et al., *Photoacoustics, thermoacoustics, and acousto-optics for biomedical imaging.* Proceedings of the Institution of Mechanical Engineers, Part H: Journal of Engineering in Medicine, 2010. **224**(2): p. 291-306.

4. Wang, L.V. and H. Wu, *Biomedical Optics: Principles and Imaging*. 2007: Wiley.

5. Sadd, M.H., *Elasticity: Theory, Applications, and Numerics*. 2009: Elsevier Science.

6. Treloar, L.R.G., *The Physics of Rubber Elasticity*. 2005: OUP Oxford.

7. Fung, Y., *Biomechanics: mechanical properties of living tissues*. 1981: Springer-Verlag.

8. http://www.instron.co.uk/wa/home/default_en_gb.aspx.

9. Lai W, R.D., Krempl E, *Introduction to Continuum Mechanics.* 1999, Woburn, MA: Butterworth-Heinmann.

10. Achenbach, J., *Wave Propagation in Elastic Solids*. 1999, New York, NY: Elsevier Science.

11. Madsen, E.L., H.J. Sathoff, and J.A. Zagzebski, *Ultrasonic shear wave properties of soft tissues and tissuelike materials.* The Journal of the Acoustical Society of America, 1983. **74**(5): p. 1346-1355.

12. Sandrin, L., et al., *Shear modulus imaging with 2-D transient elastography.* Ultrasonics, Ferroelectrics and Frequency Control, IEEE Transactions on, 2002. **49**(4): p. 426-435.

13. Rouze, N.C., et al., *Robust estimation of time-of-flight shear wave speed using a radon sum transformation.* Ultrasonics, Ferroelectrics and Frequency Control, IEEE Transactions on, 2010. **57**(12): p. 2662-2670.

14. Shigao, C., et al., *Shearwave dispersion ultrasound vibrometry (SDUV) for measuring tissue elasticity and viscosity.* Ultrasonics, Ferroelectrics and Frequency Control, IEEE Transactions on, 2009. **56**(1): p. 55-62.

15. Oestreicher, H.L., *Field and Impedance of an Oscillating Sphere in a Viscoelastic Medium with an Application to Biophysics.* The Journal of the Acoustical Society of America, 1951. **23**(6): p. 707-714.

16. Bamber, J., et al., *EFSUMB Guidelines and Recommendations on the Clinical Use of Ultrasound Elastography. Part 1: Basic Principles and Technology.* Ultraschall in

Der Medizin, 2013. **34**(2): p. 169-184.

17. Gao, L., et al., *Imaging of the elastic properties of tissue—A review.* Ultrasound in Medicine & Biology, 1996. **22**(8): p. 959-977.

18. Sarvazyan, A.P., et al., *Shear wave elasticity imaging: a new ultrasonic technology of medical diagnostics.* Ultrasound in Medicine & Biology, 1998. **24**(9): p. 1419-1435.

19. Kolen, A., *Elasticity imaging for monitoring thermal ablation therapy in liver*. 2003, University of London.

20. Ophir, J., et al., *Elastography: A quantitative method for imaging the elasticity of biological tissues.* Ultrasonic Imaging, 1991. **13**(2): p. 111-134.

21. Thitaikumar, A. and J. Ophir, *Effect of Lesion Boundary Conditions on Axial Strain Elastograms: A Parametric Study.* Ultrasound in Medicine & Biology, 2007. **33**(9): p. 1463-1467.

22. Ponnekanti, H., et al., *Fundamental mechanical limitations on the visualization of elasticity contrast in elastography.* Ultrasound in Medicine & Biology, 1995. **21**(4): p. 533-543.

23. Varghese, T. and J. Ophir, *Estimating tissue strain from signal decorrelation using the correlation coefficient.* Ultrasound in Medicine & Biology, 1996. **22**(9): p. 1249-1254.

24. Bamber, J. and N. Bush, *Freehand Elasticity Imaging Using Speckle Decorrelation Rate*, in *Acoustical Imaging*, P. Tortoli and L. Masotti, Editors. 1996, Springer US. p. 285-292.

25. Srinivasan, S. and J. Ophir, *A zero-crossing strain estimator for elastography.* Ultrasound in Medicine & Biology, 2003. **29**(2): p. 227-238.

26. Chen, E.J., et al., *Young's modulus measurements of soft tissues with application to elasticity imaging.* Ultrasonics, Ferroelectrics and Frequency Control, IEEE Transactions on, 1996. **43**(1): p. 191-194.

27. Huini, D., et al., *Optimizing multicompression approaches to elasticity imaging.* Ultrasonics, Ferroelectrics and Frequency Control, IEEE Transactions on, 2006. **53**(1): p. 90-99.

28. Lopata, R.G.P., et al., *Performance Evaluation of Methods for Two-Dimensional Displacement and Strain Estimation Using Ultrasound Radio Frequency Data.* Ultrasound in Medicine & Biology, 2009. **35**(5): p. 796-812.

29. Cho, N., et al., *Distinguishing Benign from Malignant Masses at Breast US: Combined US Elastography and Color Doppler US—Influence on Radiologist Accuracy.* Radiology, 2012. **262**(1): p. 80-90.

30. Zhi, H., et al., *Could ultrasonic elastography help the diagnosis of small breast cancer with the usage of sonographic BI-RADS classification?* European Journal of Radiology, 2012. **81**(11): p. 3216-3221.

31. Moon, H., et al., *Clinical Implication of Elastography as a Prognostic Factor of Papillary Thyroid Microcarcinoma.* Annals of Surgical Oncology, 2012. **19**(7): p. 2279-2287.

32. Cantisani, V., et al., *Prospective evaluation of multiparametric ultrasound and quantitative elastosonography in the differential diagnosis of benign and malignant thyroid nodules: Preliminary experience.* European Journal of Radiology, 2012. **81**(10): p. 2678-2683.

33. Ryan, L.K. and F.S. Foster, *Ultrasonic Measurement of Differential Displacement and Strain in a Vascular Model.* Ultrasonic Imaging, 1997. **19**(1): p. 19-38.

34. de Korte, C.L. and A.F.W. van der Steen, *Intravascular ultrasound elastography: an overview.* Ultrasonics, 2002. **40**(1–8): p. 859-865.

35. Torr, G., *The acoustic radiation force.* Am. J. Phys., 1984. **52**(5): p. 402.

36. Palmeri, M.L., et al., *A finite-element method model of soft tissue response to impulsive acoustic radiation force.* Ultrasonics, Ferroelectrics and Frequency Control, IEEE Transactions on, 2005. **52**(10): p. 1699-1712.

37. Sugimoto, T., Ueha, S. and K. Itoh. *Tissue hardness measurement using radiation force of focused ultrasound. In Proc. .* in *IEEE Ultrason. Symp.* 1990. Honolulu, HI: NY: IEEE.

38. Nightingale, K., et al., *Acoustic radiation force impulse imaging: in vivo demonstration of clinical feasibility.* Ultrasound in Medicine & Biology, 2002. **28**(2): p. 227-235.

39. Nightingale, K., *Acoustic Radiation Force Impulse (ARFI) Imaging: a Review.* Curr Med Imaging Rev, 2011. **7**(4): p. 328-339.

40. Melodelima, D., et al., *Transient Elastography Using Impulsive Ultrasound Radiation Force: A Preliminary Comparison With Surface Palpation Elastography.* Ultrasound in Medicine & Biology, 2007. **33**(6): p. 959-969.

41. Palmeri, M.L. and K.R. Nightingale, *On the thermal effects associated with radiation force imaging of soft tissue.* Ultrasonics, Ferroelectrics and Frequency Control, IEEE Transactions on, 2004. **51**(5): p. 551-565.

42. Urban, M.W., et al., *A Review of Vibro-acoustography and its Applications in Medicine.* Curr Med Imaging Rev, 2011. **7**(4): p. 350-359.

43. Konofagou, E.E. and K. Hynynen, *Localized harmonic motion imaging: Theory, simulations and experiments.* Ultrasound in Medicine and Biology, 2003. **29**(10): p. 1405-1413.

44. Pislaru, C., et al., *In vivo vibroacoustography of large peripheral arteries.* Invest Radiol, 2008. **43**(4): p. 243-52.

45. Fatemi, M., et al., *Vibro-acoustic tissue mammography.* IEEE Trans Med Imaging, 2002. **21**(1): p. 1-8.

46. Aguilo, M.A., et al., *An Inverse Problem Approach for Elasticity Imaging through Vibroacoustics.* Ieee Transactions on Medical Imaging, 2010. **29**(4): p. 1012-1021.

47. Konofagou, E.E. and K. Hynynen, *Localized harmonic motion imaging: theory, simulations and experiments.* Ultrasound in Medicine & Biology, 2003. **29**(10): p. 1405-1413.

48. Maleke, C. and E.E. Konofagou, *Harmonic motion imaging for focused ultrasound (HMIFU): a fully integrated technique for sonication and monitoring of thermal ablation in tissues.* Physics in Medicine and Biology, 2008. **53**(6): p. 1773.

49. Skovoroda, A.R., et al., *Theoretical analysis and verification of ultrasound displacement and strain imaging.* Ultrasonics, Ferroelectrics and Frequency Control, IEEE Transactions on, 1994. **41**(3): p. 302-313.

50. Skovoroda, A.R., S.Y. Emelianov, and M. O'Donnell, *Tissue elasticity reconstruction based on ultrasonic displacement and strain images.* Ultrasonics, Ferroelectrics and Frequency Control, IEEE Transactions on, 1995. **42**(4): p. 747-765.

51. Skovoroda, A.R., et al., *Reconstructive elasticity imaging for large deformations.* Ultrasonics, Ferroelectrics and Frequency Control, IEEE Transactions on, 1999. **46**(3): p. 523-535.

52. Paul, E.B. and C.B. Jeffrey, *Quantitative elasticity imaging: what can and cannot be inferred from strain images.* Physics in Medicine and Biology, 2002. **47**(12): p. 2147.

53. Lerner, R.M. and K.J. Parker, *Sonoelasticity imaging*, ed. L.W. Kessler. 1988, New York: Plenum Press.

54. Gao, L., et al., *Sonoelasticity imaging: Theory and experimental verification.* The Journal of the Acoustical Society of America, 1995. **97**(6): p. 3875-3886.

55. Catheline, S., F. Wu, and M. Fink, *A solution to diffraction biases in sonoelasticity: The acoustic impulse technique.* The Journal of the Acoustical Society of America, 1999. **105**(5): p. 2941-2950.

56. Catheline, S., et al., *Diffraction field of a low frequency vibrator in soft tissues using transient elastography.* Ultrasonics, Ferroelectrics and Frequency Control, IEEE Transactions on, 1999. **46**(4): p. 1013-1019.

57. Sandrin, L., et al., *Shear elasticity probe for soft tissues with 1-D transient elastography.* Ultrasonics, Ferroelectrics and Frequency Control, IEEE Transactions on, 2002. **49**(4): p. 436-446.

58. Bercoff, J., M. Tanter, and M. Fink, *Supersonic shear imaging: a new technique for soft tissue elasticity mapping.* Ultrasonics, Ferroelectrics and Frequency Control, IEEE Transactions on, 2004. **51**(4): p. 396-409.

59. Sarvazyan, A.P., *Method and device for shear wave elasticity imaging*, U.S.P. 5606971, Editor. 1997.

60. Nightingale, K., S. McAleavey, and G. Trahey, *Shear-wave generation using acoustic radiation force: in vivo and ex vivo results.* Ultrasound in Medicine & Biology, 2003.

29(12): p. 1715-1723.

61. Palmeri, M.L., et al., *Quantifying Hepatic Shear Modulus In Vivo Using Acoustic Radiation Force.* Ultrasound in Medicine & Biology, 2008. **34**(4): p. 546-558.

62. Joyce, M. and R. Daniel, *Shear wave speed recovery in transient elastography and supersonic imaging using propagating fronts.* Inverse Problems, 2006. **22**(2): p. 681.

63. Joyce, M. and R. Daniel, *Using level set based inversion of arrival times to recover shear wave speed in transient elastography and supersonic imaging.* Inverse Problems, 2006. **22**(2): p. 707.

64. Tanter, M., et al., *Quantitative Assessment of Breast Lesion Viscoelasticity: Initial Clinical Results Using Supersonic Shear Imaging.* Ultrasound in Medicine & Biology, 2008. **34**(9): p. 1373-1386.

65. Muller, M., et al., *Quantitative Viscoelasticity Mapping of Human Liver Using Supersonic Shear Imaging: Preliminary In Vivo Feasability Study.* Ultrasound in Medicine & Biology, 2009. **35**(2): p. 219-229.

66. Bavu, É., et al., *Noninvasive In Vivo Liver Fibrosis Evaluation Using Supersonic Shear Imaging: A Clinical Study on 113 Hepatitis C Virus Patients.* Ultrasound in Medicine & Biology, 2011. **37**(9): p. 1361-1373.

67. Hah, Z., et al., *Crawling Waves from Radiation Force Excitation.* Ultrasonic Imaging, 2010. **32**(3): p. 177-189.

68. McAleavey, S.A., Menon, M. and J. Orszulak, *Shear-modulus estimation by application of spatially-modulated impulsive acoustic radiation force.* Ultrason. Imaging, 2007. **29**: p. 87-104

69. McAleavey, S.A., Menon, M. and E. Elege, *Shear modulus imaging with spatially-modulated ultrasound radiation force.* Ultrason. Imaging, 2009. **31**: p. 217–234.

70. Taylor, L.S., et al., *Viscoelastic effects in sonoelastography: Impact on tumor detectability.* 2001 Ieee Ultrasonics Symposium Proceedings, Vols 1 and 2, 2001: p. 1639-1642.

71. Bercoff, J., et al., *The role of viscosity in the impulse diffraction field of elastic waves induced by the acoustic radiation force.* Ultrasonics, Ferroelectrics and Frequency Control, IEEE Transactions on, 2004. **51**(11): p. 1523-1536.

72. Huwart, L., et al., *Liver fibrosis: non-invasive assessment with MR elastography.* Nmr in Biomedicine, 2006. **19**(2): p. 173-179.

73. Salameh, N., et al., *Hepatic viscoelastic parameters measured with MR elastography: Correlations with quantitative analysis of liver fibrosis in the rat.* Journal of Magnetic Resonance Imaging, 2007. **26**(4): p. 956-962.

74. Catheline, S., et al., *Measurement of viscoelastic properties of homogeneous soft solid using transient elastography: An inverse problem approach.* The Journal of the Acoustical Society of America, 2004. **116**(6): p. 3734-3741.

75. Chen, S., M. Fatemi, and J.F. Greenleaf, *Quantifying elasticity and viscosity from measurement of shear wave speed dispersion.* The Journal of the Acoustical Society of America, 2004. **115**(6): p. 2781-2785.

76. Bernal, M., et al., *Material property estimation for tubes and arteries using ultrasound radiation force and analysis of propagating modes.* Journal of the Acoustical Society of America, 2011. **129**(3): p. 1344-1354.

77. Amador, C., et al., *Shearwave dispersion ultrasound vibrometry (sduv) on swine kidney.* Ultrasonics, Ferroelectrics and Frequency Control, IEEE Transactions on, 2011. **58**(12): p. 2608-2619.

78. Mitri, F.G., et al., *Shear Wave Dispersion Ultrasonic Vibrometry for Measuring Prostate Shear Stiffness and Viscosity: An In Vitro Pilot Study.* Biomedical Engineering, IEEE Transactions on, 2011. **58**(2): p. 235-242.

79. Deffieux, T., et al., *Shear Wave Spectroscopy for <emphasis emphasistype="italic">In Vivo</emphasis> Quantification of Human Soft Tissues Visco-Elasticity.* Medical Imaging, IEEE Transactions on, 2009. **28**(3): p. 313-322.

80. Zysk, A.M., et al., *Optical coherence tomography: a review of clinical development from bench to bedside.* Journal of Biomedical Optics, 2007. **12**(5): p. 051403-051403-21.

81. Fercher, A.F., et al., *Optical coherence tomography - principles and applications.* Reports on Progress in Physics, 2003. **66**(2): p. 239.

82. Costa, R.A., et al., *Retinal assessment using optical coherence tomography.* Progress in Retinal and Eye Research, 2006. **25**(3): p. 325-353.

83. Hee, M.R., et al., *QUantitative assessment of macular edema with optical coherence tomography.* Archives of Ophthalmology, 1995. **113**(8): p. 1019-1029.

84. Bouma, B.E., et al., *Evaluation of intracoronary stenting by intravascular optical coherence tomography.* Heart, 2003. **89**(3): p. 317-320.

85. Jang, I.-K., et al., *In Vivo Characterization of Coronary Atherosclerotic Plaque by Use of Optical Coherence Tomography.* Circulation, 2005. **111**(12): p. 1551-1555.

86. Luo, W., et al., *Three-dimensional optical coherence tomography of the embryonic murine cardiovascular system.* Journal of Biomedical Optics, 2006. **11**(2): p. 1014-8.

87. Schmitt, J., *OCT elastography: imaging microscopic deformation andstrain of tissue.* Optics Express, 1998. **3**(6): p. 199-211.

88. Leitgeb, R., C. Hitzenberger, and A. Fercher, *Performance of fourier domain vs. time domain optical coherence tomography.* Optics Express, 2003. **11**(8): p. 889-894.

89. Adie, S.G., et al., *Spectroscopic optical coherence elastography.* Optics Express, 2010. **18**(25): p. 25519-25534.

90. Liang, X., et al., *Dynamic spectral-domain optical coherence elastography for tissue characterization.* Optics Express, 2010. **18**(13): p. 14183-14190.

91. Zhang, X. and J.F. Greenleaf, *Estimation of tissue's elasticity with surface wave speed.* The Journal of the Acoustical Society of America, 2007. **122**(5): p. 2522-2525.

92. Li, C., et al., *Quantitative elastography provided by surface acoustic waves measured by phase-sensitive optical coherence tomography.* Optics Letters, 2012. **37**(4): p. 722-724.

93. Mohan, K.D. and A.L. Oldenburg, *Elastography of soft materials and tissues by holographic imaging of surface acoustic waves.* Optics Express, 2012. **20**(17): p. 18887-18897.

94. Li, C., Z. Huang, and R.K. Wang, *Elastic properties of soft tissue-mimicking phantoms assessed by combined use of laser ultrasonics and low coherence interferometry.* Optics Express, 2011. **19**(11): p. 10153-10163.

95. Wang, S., et al., *Noncontact measurement of elasticity for the detection of soft-tissue tumors using phase-sensitive optical coherence tomography combined with a focused air-puff system.* Optics Letters, 2012. **37**(24): p. 5184-5186.

96. Razani, M., et al., *Feasibility of optical coherence elastography measurements of shear wave propagation in homogeneous tissue equivalent phantoms.* Biomedical Optics Express, 2012. **3**(5): p. 972-980.

97. Song, S., Z. Huang, and R.K. Wang, *Tracking mechanical wave propagation within tissue using phase-sensitive optical coherence tomography: motion artifact and its compensation.* Journal of Biomedical Optics, 2013. **18**(12): p. 121505-8.

98. Oldenburg, A.L., et al., *Imaging and Elastometry of Blood Clots Using Magnetomotive Optical Coherence Tomography and Labeled Platelets.* Selected Topics in Quantum Electronics, IEEE Journal of, 2012. **18**(3): p. 1100-1109.

99. Crecea, V., et al., *Magnetomotive nanoparticle transducers for optical rheology of viscoelastic materials.* Optics Express, 2009. **17**(25): p. 23114-23122.

100. Kennedy, K.M., et al., *Needle optical coherence elastography for tissue boundary detection.* Optics Letters, 2012. **37**(12): p. 2310-2312.

101. Bossy, E., et al., *Transient optoelastography in optically diffusive media.* Applied Physics Letters, 2007. **90**(17): p. 174111-174114.

102. Xu, M. and L.V. Wang, *Photoacoustic imaging in biomedicine.* Review of Scientific Instruments, 2006. **77**(4): p.041101-.041110

103. Leveque-Fort, S., et al., *In situ local tissue characterization and imaging by backscattering acousto-optic imaging.* Optics Communications, 2001. **196**(1-6): p. 127-131.

104. Li, J., et al., *Transmission- and side-detection configurations in ultrasound-modulated optical tomography of thick biological tissues.* Applied Optics, 2003. **42**(19): p. 4088-4094.

105. Wang, L.V., *Mechanisms of Ultrasonic Modulation of Multiply Scattered Coherent Light: An Analytic Model.* Physical Review Letters, 2001. **87**(4): p. 043903.

106. Wang, L.V., *Mechanisms of ultrasonic modulation of multiply scattered coherent light: a Monte Carlo model.* Optics Letters, 2001. **26**(15): p. 1191-1193.

107. Sakadzic, S. and L.V. Wang, *Modulation of multiply scattered coherent light by ultrasonic pulses: An analytical model.* Physical Review E, 2005. **72**(3): p. 036620.

108. Sakadžić, S. and L.V. Wang, *Correlation transfer equation for ultrasound-modulated multiply scattered light.* Physical Review E, 2006. **74**(3): p. 036618.

109. Sakadzic, S. and L.V. Wang, *Correlation transfer equation for multiply scattered light modulated by an ultrasonic pulse.* J. Opt. Soc. Am. A, 2007. **24**(9): p. 2797-2806.

110. Wang, L., S.L. Jacques, and X. Zhao, *Continuous-wave ultrasonic modulation of scattered laser light to image objects in turbid media.* Optics Letters, 1995. **20**(6): p. 629-631.

111. Wang, L. and X. Zhao, *Ultrasound-modulated optical tomography of absorbing objects buried in dense tissue-simulating turbid media.* Applied Optics, 1997. **36**(28): p. 7277-7282.

112. Sakadzic, S. and L.V. Wang, *High-resolution ultrasound-modulated optical tomography in biologicaltissues.* Opt. Lett., 2004. **29**(23): p. 2770-2772.

113. Kothapalli, S.-R. and L.V. Wang, *Ultrasound-modulated optical microscopy.* Journal of Biomedical Optics, 2008. **13**(5): p. 054046-054046-8.

114. Li, Y., et al., *Pulsed ultrasound-modulated optical tomography using spectral-hole burning as a narrowband spectral filter.* Applied Physics Letters, 2008. **93**(1): p. 011111-3.

115. Gross, M., et al., *Theoretical description of the photorefractive detection of the ultrasound modulated photons in scattering media.* Opt. Express, 2005. **13**(18): p. 7097-7112.

116. Ramaz, F., et al., *Photorefractive detection of tagged photons in ultrasound modulated optical tomography of thick biological tissues.* Opt. Express, 2004. **12**(22): p. 5469-5474.

117. Li, J., G. Ku, and L.V. Wang, *Ultrasound-Modulated Optical Tomography of Biological Tissue by Use of Contrast of Laser Speckles.* Applied Optics, 2002. **41**(28): p. 6030-6035.

118. Ruan, H., M.L. Mather, and S.P. Morgan, *Pulsed ultrasound modulated optical tomography with harmonic lock-in holography detection.* Journal of the Optical Society of America A, 2013. **30**(7): p. 1409-1416.

119. Lévêque, S., et al., *Ultrasonic tagging of photon paths in scattering media: parallel speckle modulation processing.* Optics Letters, 1999. **24**(3): p. 181-183.

120. Atlan, M., et al., *Pulsed acousto-optic imaging in dynamic scattering media with heterodyne parallel speckle detection.* Optics Letters, 2005. **30**(11): p. 1360-1362.

121. Lesaffre, M., et al., *Acousto-optical coherence tomography using random phase*

jumps on ultrasound and light. Opt. Express, 2009. **17**(20): p. 18211-18218.

122. Lev, A. and B.G. Sfez, *Pulsed ultrasound-modulated light tomography.* Opt. Lett., 2003. **28**(17): p. 1549-1551.

123. Zemp, R.J., C. Kim, and L.V. Wang, *Ultrasound-modulated optical tomography with intense acoustic bursts.* Appl. Opt., 2007. **46**(10): p. 1615-1623.

124. Li, R., et al., *Parallel detection of amplitude-modulated, ultrasound-modulated optical signals.* Opt. Lett., 2010. **35**(15): p. 2633-2635.

125. Li, R., et al., *Effects of acoustic radiation force and shear waves for absorption and stiffness sensing in ultrasound modulated optical tomography.* Optics Express, 2011. **19**(8): p. 7299-7311.

126. Rousseau, G., A. Blouin, and J.-P. Monchalin. *Improvement of sensitivity of acousto-optical imaging using a powerful long pulse laser*. in *Proceedings of the SPIE*. 2008. San Jose, CA: Society of Photo-Optical Instrumentation Engineers (SPIE).

127. Xu, X., H. Liu, and L.V. Wang, *Time-reversed ultrasonically encoded optical focusing into scattering media.* Nat Photon, 2011. **5**(3): p. 154-157.

Chapter 3

Imaging the ultrasound field and shear wave propagation at the boundary of phantoms using ultrasound modulated optical tomography and laser speckle contrast analysis

In this Chapter, a method based on ultrasound modulated optical tomography (UOT) to visualize both the ultrasound (US) beam and shear wave propagation at an optical boundary of phantoms is presented. By synchronising the CCD exposure time and the US burst, a contrast-difference image of the US beam was obtained with the imaginary detection (with a lens) of speckle pattern, revealing the features of the beam which agreed with the measurement by a hydrophone. The contrast-difference images of the shear wave obtained by exposing the CCD at different times after the US burst showed the propagation and spread of the shear wave generated by the acoustic radiation force (ARF). The purpose to investigate the shear wave imaging is to obtain a better understanding of the interaction between shear waves and light in optically transparent mediums and get prepared for the shear wave tracking in optically turbid mediums. The imaging of ultrasound field, as an additional finding, provides an alternative fast way to map the ultrasound field, which holds the potential to be a tool for the characterisation of an ultrasound transducer. This work was in collaboration with Dr Lipei Song from the Department of Cancer and Surgery in Imperial College London, where she was focused on the modelling of the method [1] and I was responsible for the experimental validation. The modelling is not included in this chapter since it is independent from my work and I am not involved. Part of the results shown in this chapter has been included in [2] .

3.1 Introduction

Several methods have been developed to map the US field, such as hydrophone, Schlieren imaging [3] and so on [4], but they either are complicated to accomplish or are expensive and slow. For example, the hydrophone, which is the most popular method to map the US field, is a point-detection device and requires a point-by-point scanning for the whole field. In this chapter, we propose an alternative way to map the US field based on a UOT system and local laser speckle analysis. The local laser speckle analysis has been applied to motion detection, especially to blood flow detection where the speckle contrast is correlated to blood flow [5]. The proposed method could map the US field with a single CCD exposure (ms). We also extend this method to track the propagation of the shear wave at the edge of a turbid media, where the shear wave fronts are observed in both homogenous and heterogeneous phantoms. In the following sections, experimental design, including the setup and the method, is firstly described. The results are then represented and discussed.

3.2 Experimental design

Figure 3.1 shows a side view of the experimental setup modified from the UOT system illustrated in Figure 2.12. The imaging lens (focal length =30 mm, Thorlabs) is positioned between the iris and the observed plane (an imaging geometry), such that the speckle pattern on the CCD is a duplicate of that in the observed plane. To satisfy the Nyquist sampling criterion and to increase the contrast of the speckle pattern imaged [6], the size of speckle was adjusted to be more than twice the size of the image pixel (pixel size of 6.45 μm) by adjusting the iris size based on $SS = 2.44\lambda(1+M)F$ [7], where SS is the speckle size, λ is the wavelength of the coherent

light, M is the magnification (4 for our set up) and F is the ratio of the focal length of the image lens (30 mm) and the iris size. The phantom is specially designed to have two layers. The first layer is a turbid layer made from 0.8 % agar powder and 4% intralipid. This layer is used to diffuse light for a large illuminating area and thus a large US field could be imaged for one single shot of the CCD. In the experiment, the illuminating area was around 27 mm in diameter and a 27 mm US field was captured by the CCD with a single shot. The field-of-view of the CCD is adjustable by modifying the distance between the phantom and camera – a longer distance will result in a smaller field of view. In the experiment, this distance was chosen to match the optical illumining area with the field-of-view of the CCD. The second layer is a layer made of 0.8% agar only. This layer is to maintain the local speckle pattern after the modulation so as to visualise the local US and shear wave modulation because agar hardly scatters light.

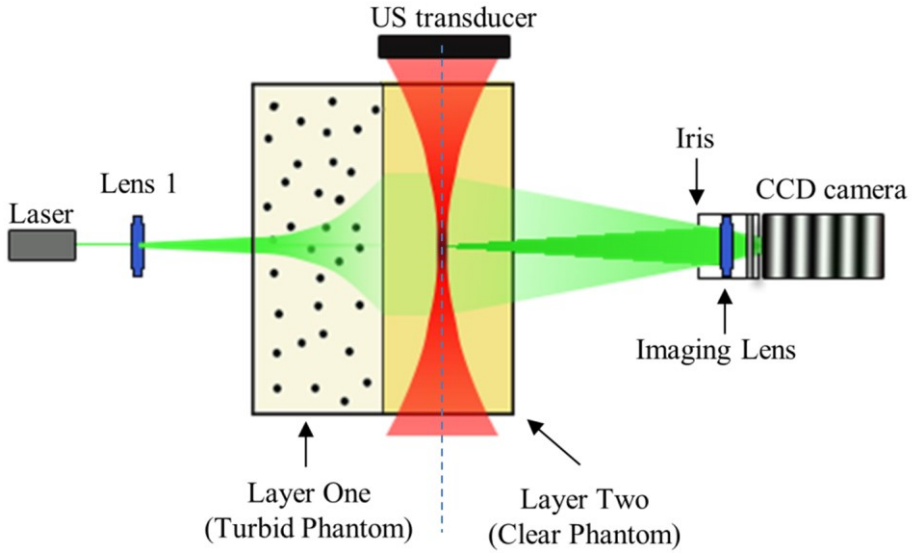

Figure 3.1 System setup. The laser is a 532 nm solid-state laser. The ultrasound (US) transducer is a single element focused transducer. The central frequency of the transducer is 5 MHz. Lens 1 is used to spread the light beam (green). The iris controls the speckle size and the imaging lens is to map the speckle pattern on the observed plane (dashed line) to the CCD camera.

Figure 3.2 shows the timing scheme for triggers. The control system for the scheme is the same as in Figure 2.13(a) where the triggers from the trigger generator synchronises the US and the CCD. The upper arrows are the timings of the US burst, while the lower arrows are the timings of the CCD exposure. The image at 0 ms is obtained immediately after the US burst to capture the US modulation while the shear wave propagation is captured by delaying the exposure of the CCD by 1, 2 and 3 ms after the cessation of US burst.

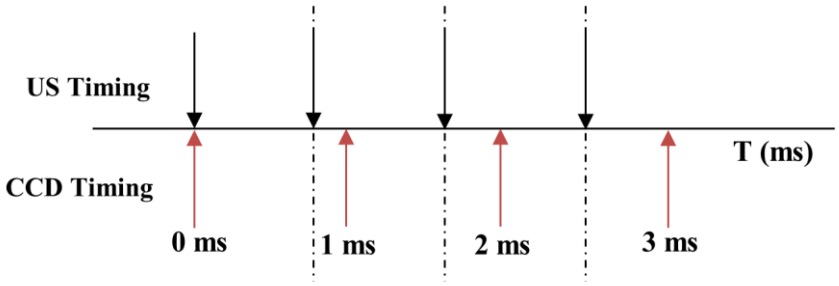

Figure 3.2 Time scheme for visualisation of the US beam and the shear wave. The upper row is the timings for the US bursts. The lower row is the timings of the CCD exposure.

The frame rate of the CCD is 10 fps, which cannot track the shear wave in real time. Therefore, the shear wave was repeatedly generated in the experiment and the CCD exposure was delayed by certain times to track the progression of the shear wave. A 7 x 7 pixels （about 170 μm x 170 μm in the observation plane）moving window was used to calculate the local contrast of the CCD images ($C = \frac{\sigma}{\bar{I}}, \sigma$ is the standard deviation of the speckle intensity and $\bar{I}$ is the spatial mean of the intensity) and then the contrast difference was derived by subtracting the contrast values after the US burst from those before ($\Delta C = C_{before} - C_{after}$). The timing for the CCD exposure before the US burst is not shown in Figure 3.2: it was always 200 ms before the US burst in the experiment.

In the first experiment where the US field was captured, the US focus was positioned

within the second layer. One reason for the position was to obtain a clear image of the US field because agar hardly scatters light and thus the local modulation due to the displacement of scatterers and the change of refractive index caused by US wave is retained; another reason was to minimise the ARF since agar hardly absorbs US and thus the ARF is ignored. The ARF needs to be minimised so as to the contrast difference may correlate to the pressure of the ultrasound. A 2 ms US burst and a 2 ms exposure time were used to capture the US field so that the US modulation was stable within the exposure time. 20 images were recorded before and immediately after the US burst (0 ms). The final contrast-difference image of the US field was an average over the 20 images to reduce noise. Due to the limited size of the field of view (27 mm x 27 mm), the final US-field image was reconstructed by moving the CCD along the US beam and combining different parts of the US fields together. A hydrophone (Precision Acoustics Ltd., tip diameter = 0.5 mm) was used to map the US field with the same peak-negative pressure in water and the result was compared with the contrast-difference map. The hydrophone was placed in the focal zone of the transducer in distilled water and motorized to scan the US beam along both axial and lateral direction with fixed step sizes - 1 mm for the axial scan and 0.2 mm for the lateral scan. At each scan position, the peak-negative pressure was then read by an oscilloscope.

In the second experiment, the shear wave propagation was imaged. The US focus was positioned in the intersected plane of the two-layer phantom, such that the shear wave was generated at the edge of the turbid phantom and imaged by the CCD through the clear layer of the phantom. In this experiment, the first layer not only helped expand the light beam but also was used to generate shear waves since it attenuates

ultrasound. The shear wave modulation on light is mainly contributed by the displacement of scatterers resulting from the shear wave propagation. The modulation caused by the refractive index change is small due to the slow motion during the CCD exposure [8]. One, 2 and 3 ms delay times were set to record the propagation of the shear wave and a series of contrast-difference images were calculated.

In the third experiment, the shear wave propagation in a heterogeneous phantom was imaged. An inclusion made of 1.0% agar and 4% intralipd was embedded in the first layer of the phantom. The inclusion was stiffer than the surrounding phantom while its optical properties were kept the same. Other settings remained the same as in the second experiment.

3.3 Result

3.3.1 Ultrasound field

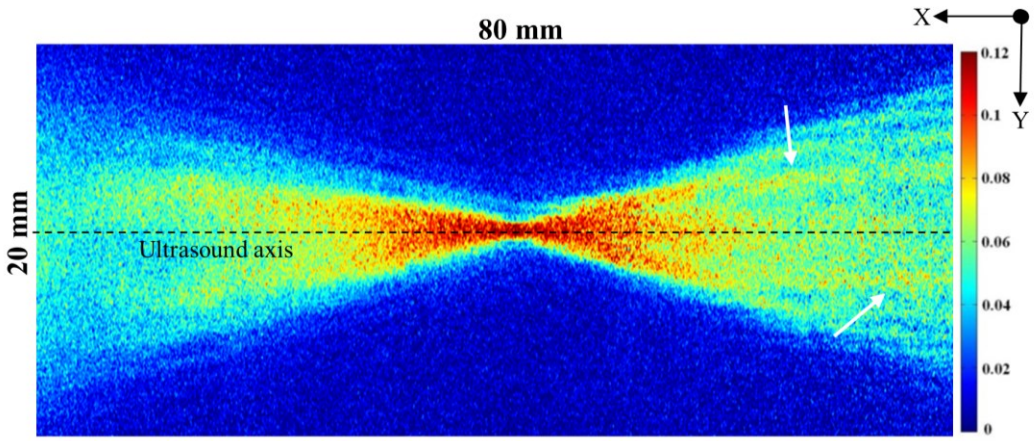

Figure 3.3 Contrast-difference image for the US field. The US propagates along the +x direction. The colour represents the magnitude of the contrast difference and the arrows indicate the near-field heterogeneity of the US.

Figure 3.3 shows a contrast-difference image of an 80mm x 20 mm US field propagating from right to left (+x direction). The colour represents the magnitude of the contrast difference - the warmer the colour the larger the magnitude. In the region

of the US focus, the magnitude of the contrast difference is large, indicating a large modulation of the US within this area. In the near field (right part of the image), the field heterogeneity (white arrows) is observed, which matches the features in the near field of a single element US transducer [9].

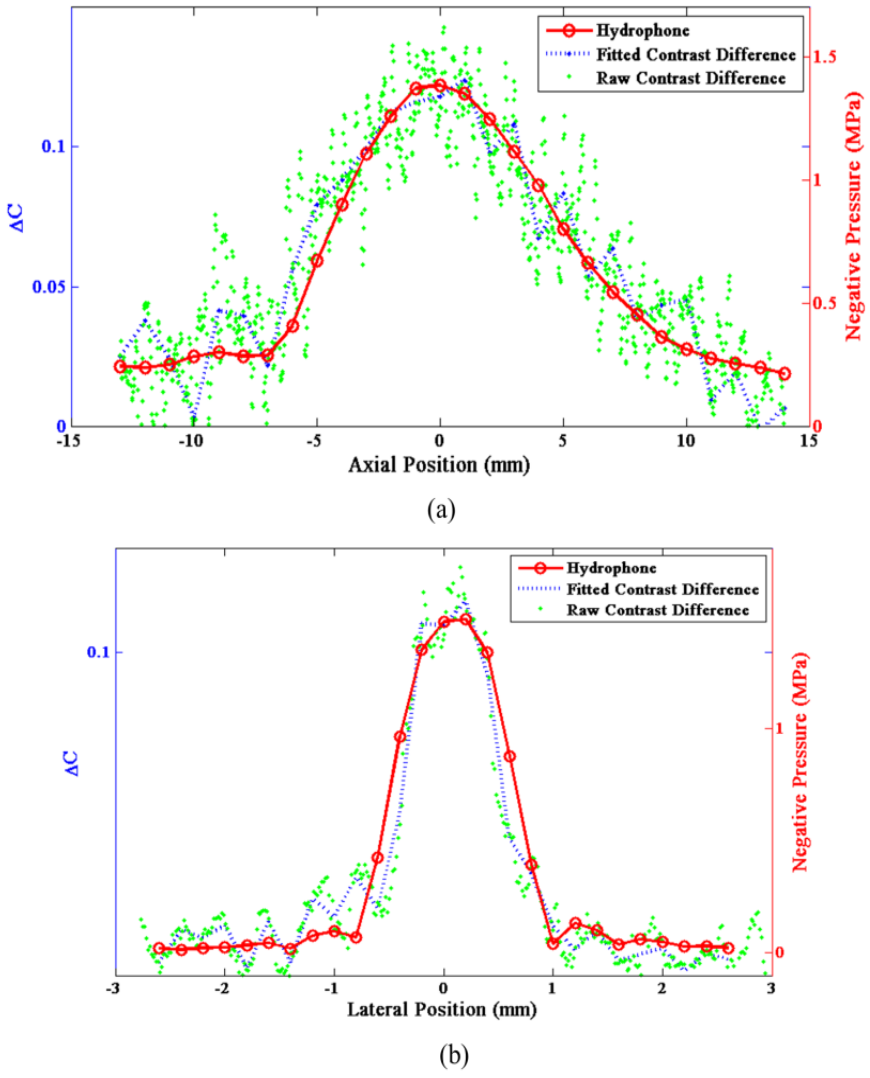

Figure 3.4 Overlap of UOT result and hydrophone result. (a) Axial profile and (b) transverse profile. It should be noted that the profiles were scaled based on their peak and baseline values and then overlapping the peak values from the two measurements to register their lateral positions.

Figure 3.4 shows the comparisons between the contrast-difference signals and the hydrophone measurements within the US focal region along the axial direction and

the transverse direction respectively. In order to make a comparison, the profiles were scaled based on their peak and baseline values and then overlapping the peak values from the two measurements to register their lateral positions. Figure 3.4(a) is the overlap of the axial profiles (along the US axis). The green dots are the raw contrast-differences along the US axis and the blue dotted line is their smoothing spline fit (MATLAB R2011b, spaps). The red marked line is the hydrophone measurement result. They show a good agreement in the figure and the full width at half maximum (FWHM) of both measurements is calculated to be around 10 mm which matches the axial dimension of the focal zone of the transducer reported in the manufacture sheet. Figure 3.4(b) is the overlap of the transverse profile. The FWHM is calculated to be around 0.8 mm using both methods, which also matches the represented manufacture's dimension.

3.3.2 Shear wave propagation

Figure 3.5 demonstrates the progression of the shear wave generated by ARF. The images in the first row are acquired in the homogenous phantom while the images in the second row are in the heterogeneous phantom. For the homogenous phantom, the image in (a) is acquired at 1 ms after the burst. The profile of US beam is still perceivable but less clear than in Figure 3.3. A blurred shape is seen in (b) which is acquired at 2 ms after the burst. Compared with (a), the image in (b) suggests the propagation of the shear wave is mainly along the lateral direction. (c) shows the shear wave at 3 ms after the burst. The shear wave further expands along the lateral direction and the position of the wavefront is about 6 mm from the US focus, suggesting the shear wave speed is about 2 mm/ms. For the heterogeneous phantom, (d), (e) and (f) are acquired at 1 ms, 2 ms and 3 ms after the burst respectively. The

white circles indicate the position of the inclusion, and as a comparison the same region is depicted in (a), (b) and (c). Without the inclusion, shear wave reaches the depicted region at around 3 ms after the burst while it starts propagating in the inclusion only after 1 ms of the burst, suggesting the shear wave propagates faster in stiffer medium. This is consistent with Equation 2-14 which shows the shear wave speed increases as the elastic modulus increases.

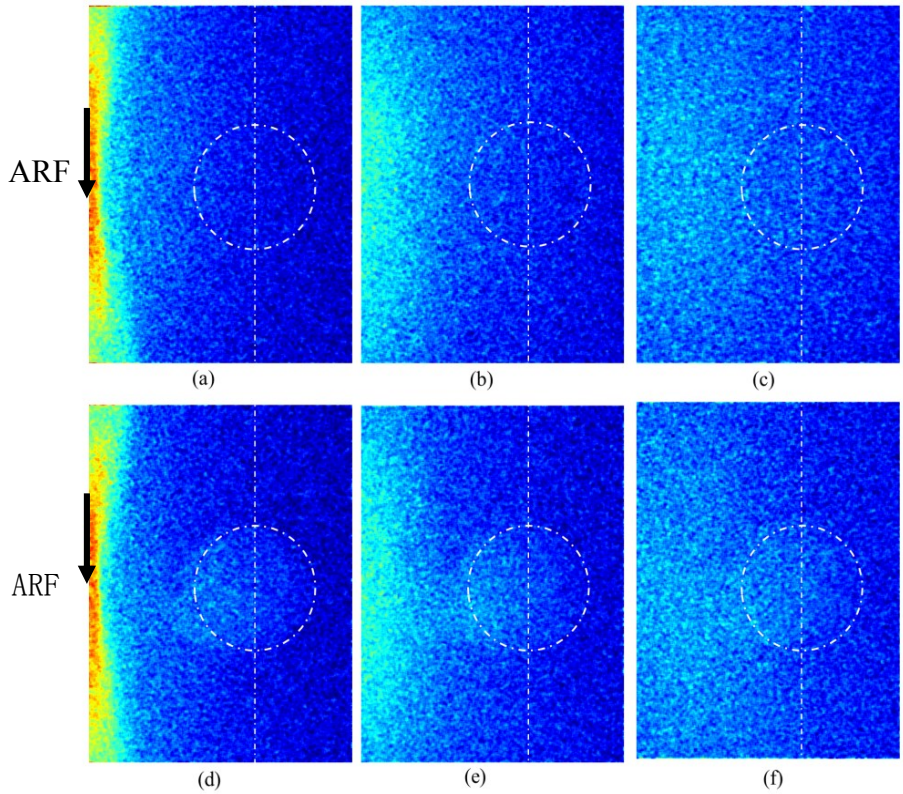

Figure 3.5 Shear wave propagation at 1, 2 and 3 ms after a 2 ms US burst. The first row shows the propagation in a homogenous phantom, and the second row shows the propagation in a heterogeneous phantom where a stiff inclusion is embedded. The arrows indicate the direction and position of the acoustic radiation force. The dotted circles in the second row indicate the position of stiff inclusion. The same area in the homogenous phantom (the first row) is also depicted (dotted circles) and aligned (dotted lines) with the lower images, such that the difference at the same time of the shear wave propagation can be compared in both phantoms.

3.3 Discussion

In this chapter, a method that maps the whole US field within a few milliseconds was

proposed. Compared with hydrophone measurements, firstly, the speed of the acquisition is much quicker, and given this very high speed, it holds the potential to be a 3-dimensiomal mapping if the US beam was rotated. Secondly, the mapping resolution for the field is controllable, depending on the field of view of the system and the size of windows used to calculate the local contrast, whereas the resolution of the hydrophone measurement is determined by the size of its tip. Thirdly, the hydrophone measures the US field in water which could be biased by the complex structure of biological tissues. This may be overcome by the proposed method where a US field could be generated at the shallow surface of samples, such that the modulation may be retained and the US field in the samples may be obtained. In the experiment, the US was focused in the clear gel in order to minimise the effect of the ARF modulation. This may also be accomplished by reducing the exposure time of camera since the ARF modulation is slow compared with the US modulation. However, reducing the exposure time could also reduce the signal-to-noise ratio.

In current system, only a single image lens was used without considering any aberration. To optimise the image quality, a more sophisticated imaging system is required. Secondly, the laser beam was mainly expanded by the first turbid layer of the phantom. The resulting laser beam was not collimated and the illumination area was fixed. It needs to be replaced by beam expanders so that the laser beam is well controlled. Finally, the system is limited by the fact that the relations between the local optical contrast value and the US pressure/shear wave displacement have not been established. The relations are affected by a few factors, such as the camera exposure time and laser speckle size. Given their complex relationships, it may not justify to compare between the US pressure and the contrast difference as shown in

Figure 3.4. Therefore, either a theoretical approach (which may be able to relate contrast difference to pressure [10]) or a calibration process (which may establish the relation between pressure/displacement with a certain system setup such as a fixed CCD exposure time and speckle size [8]) needs to be further investigated.

3.4 Conclusion

In one aspect, this work provided me a chance to be acquainted with our UOT system. In another aspect, by imaging the shear wave propagation, the illustrated modulation of shear wave inspired me when proposing the tracking of shear wave in turbid media in the following chapters. In addition, the shear wave imaging also provides a potential way to quantify the elasticity of tissue without mechanical scanning and would be interesting to further develop it. Meanwhile the US field mapping is also an interesting alternative use of the system.

References

1. Song, L., *Endoscopic Laser Speckle Contrast Analysis for Tissue Perfusion*, in *Surgery and Cancer*. 2013, Imperial College London: London.

2. Song, L., et al. *Imaging the ultrasound field and shear-wave propagation using acousto-optic laser speckle contrast analysis (AO-LASCA)*. 2012.

3. Neumann, T. and H. Ermert, *Schlieren visualization of ultrasonic wave fields with high spatial resolution.* Ultrasonics, 2006. **44, Supplement**(0): p. e1561-e1566.

4. Yao, G. and L.V. Wang, *Full-field mapping of ultrasonic field by light-source-synchronized projection.* The Journal of the Acoustical Society of America, 1999. **106**(4): p. L36-L40.

5. Briers, J.D. and S. Webster, *Laser speckle contrast analysis (LASCA): a nonscanning, full-field technique for monitoring capillary blood flow.* Journal of Biomedical Optics, 1996. **1**(2): p. 174-179.

6. Kirkpatrick, S.J., D.D. Duncan, and E.M. Wells-Gray, *Detrimental effects of speckle-pixel size matching in laser speckle contrast imaging.* Optics Letters,

2008. **33**(24): p. 2886-2888.

7. Boas, D.A. and A.K. Dunn, *Laser speckle contrast imaging in biomedical optics.* Journal of Biomedical Optics, 2010. **15**(1): p. 011109.

8. Li, S., et al., *Tracking shear waves in turbid medium by light: theory, simulation, and experiment.* Optics Letters, 2014. **39**(6): p. 1597-1600.

9. Bushberg, J.T., et al., *The Essential Physics of Medical Imaging*. 2011: Wolters Kluwer Health.

10. Zemp, R., S. Sakadžić, and L.V. Wang, *Stochastic explanation of speckle contrast detection in ultrasound-modulated optical tomography.* Physical Review E, 2006. **73**(6): p. 061920.

Chapter 4

Shear wave laser speckle contrast analysis for the quantification of tissue elasticity

In this chapter, I propose an optical elastography system that could work at centimetre depths within tissue-mimicking phantoms. With speckle contrast analysis, the speeds of shear waves in the tissue mimicking phantom were quantified. A differential measurement scheme involving generation of shear waves at two different positions was used to improve the accuracy and spatial resolution of the elasticity measurements. The results on both homogeneous and heterogeneous phantoms were compared with the results from an independent compression test with the Instron bench system, demonstrating the feasibility and accuracy of the technique for imaging and quantifying elasticity. The relative error in the estimation of shear wave speed can be as low as 3.3% with a spatial resolution of 2 mm, increasing to 8.8% with a spatial resolution of 1mm for the medium-stiffness phantom. The system was shown to be highly sensitive and able to track shear waves propagating over several centimeters, given the US excitation amplitude and the phantom material used in this study. I also found that the reflection of shear waves from boundaries between regions with different elastic properties can cause significant bias in the estimation of elasticity, which also applies to other shear wave tracking techniques. This bias can be reduced at the expense of reduced spatial resolution.

4.1 Introduction

Tissue elasticity is closely related to the speed of shear waves propagating in biological tissue. Currently, ultrasound (US) and magnetic resonance imaging are the

main modalities used to track shear waves and both have been proven in several clinical applications such as cancers and cardiovascular diseases. Compared with these two modalities, optics-based elastography may bring extra information on optical properties that are also correlated to pathological changes of tissue. In this chapter, a highly sensitive optical measurement technique based on ultrasound modulated optical tomography (UOT) is proposed as an alternative way to track shear waves. The system can achieve spatial resolution comparable to the ultrasound-based system. To my knowledge, this is the first optics-based elastography system that could measure quantitative information on tissue at centimetre depths. In the following sections, experimental design, including the setup and the method, is firstly described. Then, the results are represented and the reflection of shear wave at boundaries is investigated. Finally, the work is summarised and discussed.

4.2 Theory

The theory has been reviewed in Chapter 2. Here I give a brief summary of the basic equations. Acoustic radiation force (ARF) is a force resulting from the momentum transfer between the propagating US wave and the tissue. Having the same direction as the US wave propagation, the magnitude of ARF can be approximated by [1]:

$$\boldsymbol{F = \frac{2aI}{c}}, \tag{4-1}$$

where F (kg/(s^{2}m^2)) is the ARF, a (Np/m) is the absorption coefficient of tissue, I (W/m^2) is the temporal average intensity and c (m/s) is the sound speed in tissue. The force is in the form of a body force and capable to deform soft tissues in the order of micrometres. When ARF is applied to tissue, shear waves are generated and propagate away from the excitation region. The speed of shear waves can be directly related to

the mechanical properties of tissue by:

$$\boldsymbol{s = \sqrt{\frac{\mu}{\rho}};\ \mu = \frac{E}{2(1+\gamma)}},\tag{4-2}$$

where s (m/s) is shear wave speed, μ (Pa) is the shear modulus, ρ (kg/m^3) is density, E (Pa) is Young's modulus and γ is Poisson's ratio which is assumed to be 0.5 for incompressible tissues, providing the relationship $E = 3\mu$. Consequently, Young's modulus can be directly related to shear wave velocity by:

$$\boldsymbol{E = 3\rho s^2}.\tag{4-3}$$

As reviewed in Chapter 2, there are two main ways to measure the speed of shear waves: direct inversion of the Helmholtz equation [2-4] and the time-of-flight [5-7] that uses the wave arrival time. These methods mainly use US to detect tissue displacement caused by shear waves and the detection sensitivity is typically limited to several micrometres and above.

Optical detection of diffused coherent light from within tissue is known to be highly sensitive to tissue displacement. Tissue vibration as a result of diagnostic US excitation is typically ≤ hundreds of nanometres, while such vibration can be readily detected optically. This has been utilised in US modulated optical tomography to image local tissue optical properties in millimetre to centimetre depth [8]. Simulations have shown that tissue displacements at the level of tens of nanometres can be detected by using coherent light and detecting the phase changes of diffused photons from tissue [9]. In this chapter, an ARF-based shear wave elasticity imaging technique using a modified US-modulated optical tomography system using coherent light and a camera using charge-coupled device (CCD) camera is proposed.

4.3 Method

4.3.1 Experimental set up

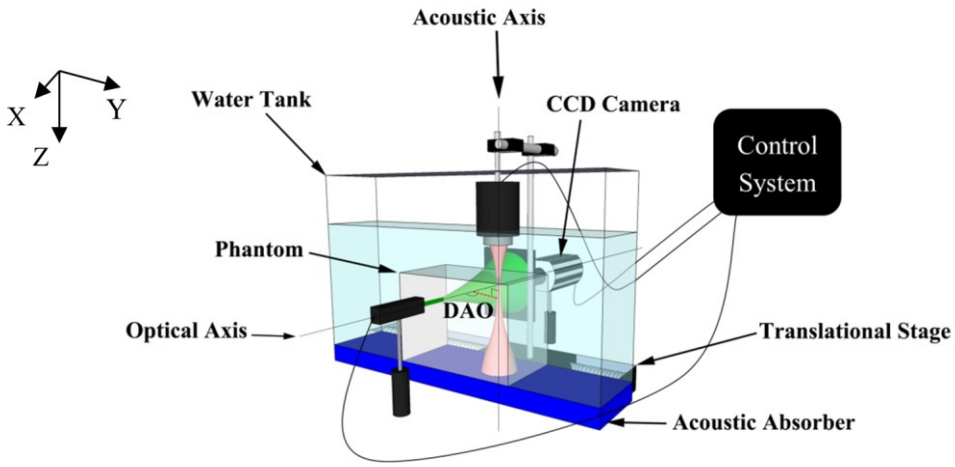

Figure 4.1 Experimental set up. The US and light are perpendicular to each other and intersect within the phantom. The acoustic axis is moved several millimetres away from the optical axis (DAO) by a translational stage. The phantom and US transducers are both immersed in a water tank to minimise the density mismatch at the phantom surface. An acoustic absorber is positioned under the phantom to avoid reflected US from the tank bottom. The camera and transducer are synchronised by the control system. CCD is short for charge-coupled device.

Figure 4.1 illustrates the experimental set up. A broadband focused US transducer is excited using a 1 ms 5 MHz US burst to generate shear waves within the tissue mimicking phantoms. The US burst is transmitted along the Z-axis and shear waves are generated and propagated along the Y-axis. An acoustic absorber is placed underneath the phantoms to avoid acoustic reflections from the bottom of a water tank, made of Perspex which is transparent to laser light. The transducer is positioned on a translational stage so it could be stepped along the direction of shear wave propagation. A continuous 532 nm Nd:YAG laser beam and a CCD camera are positioned along the X-axis and perpendicular to the acoustic axis. The US focus is deliberately displaced away from the optical axis to facilitate tracking of the shear

wave (the distance between the acoustic and the optical axes is signified as DAO in Figure 4.1).

An iris diaphragm was placed in front of the CCD to control the speckle size. The speckle size L_{sp} is determined by the optical wavelength (λ), the area of iris (A) and the distance between iris and observed plane (z) as

$$\mathbf{L_{sp}} = \frac{(\lambda z)^2}{\mathbf{A}}. \quad \textbf{(4-4)}$$

In my experiment, the wavelength of light was 532 nm and the speckle size was 12.9 μm which was the size of two CCD pixels. According to the equation, the ratio of the distance square (z^2) and the area of iris (A) was calculated as 45.7. Many pairs of the distance and iris area could be realised and I used 120 mm for the distance between the iris and the CCD and 7 mm for the iris diameter. The final speckle size was approximated using a Fast Fourier Transform and a desired system setup captured a maximum frequency of the half of the image dimension (512 pixels for our CCD camera). There is no lens in the system, the speckle patter is capture in a free space.

The control system is shown in Figure 4.2(a). The function generator is programed to generate a 1 ms 5 MHz burst for the US transducer and the amplifier magnified the burst amplitude before it is transmitted to the transducer to obtain the desired US pressures at the focus. Labview is used to control the trigger generator which sent triggers for the US excitation and image acquisition with the CCD camera. Finally, the captured images are stored in the PC for post-processing. In the experiment, since the modulated photons were randomly scattered after the modulation, photons were detected in free space and global contrast was calculated by the ratio of the standard deviation and mean of the intensities in the whole image.

Due to the limitation of the CCD frame rate (10 Hz), the shear wave was tracked by generating the shear wave multiple times and delaying the interval between the shear wave launch and the CCD capture. Figure 4.2(b) illustrates the trigger scheme for the trigger generator. The trigger cycle depicts the cycle for the shear wave generation, which is chosen, on the one hand, to save experimental time, and on the other hand, to prevent the US transducer from overheating. A 1.5 s trigger cycle was used in the experiment and within each trigger cycle, the trigger generator was programed to generate three triggers. Trigger 1 was produced for the CCD camera at the beginning of each trigger cycle to obtain the background image without the shear wave modulation (C_{BG} for background). Trigger 2 was after trigger 1 and used for triggering the shear wave generation via the function generator. Trigger 3 is then produced for the CCD camera to record the shear wave modulation (C_M for modulation). Two CCD images are obtained for each trigger cycle (Triggers 1 & 3) and the contrast difference (ΔC) was difference between C_{BG} and C_M (Equitation 4-5). The timing of triggers 1 and 2 was fixed for every trigger cycle while the timing of trigger 3 was delayed with a 0.2 ms step. By delaying the trigger 3, the change of the contrast difference with time ($\Delta C(t)$, Equation 4-5) was produced and the shear wave propagation was tracked regardless of the slow CCD frame rate.

$$\Delta \boldsymbol{C(t)} = \boldsymbol{C_{BG}(t) - C_M(t)}. \quad \textbf{(4- 5)}$$

Motions could also change the contrast difference in the same way as the shear wave does, where they both add modulation into the signal and result in decrease of speckle contrast. Motions such as external vibrations are noise in the shear wave tracking and needs to be minimised. As a feasibility study, these motions in my study were minimised by keeping the experimental setup on an optical table and storing the

phantom in degased water at 21ºC.

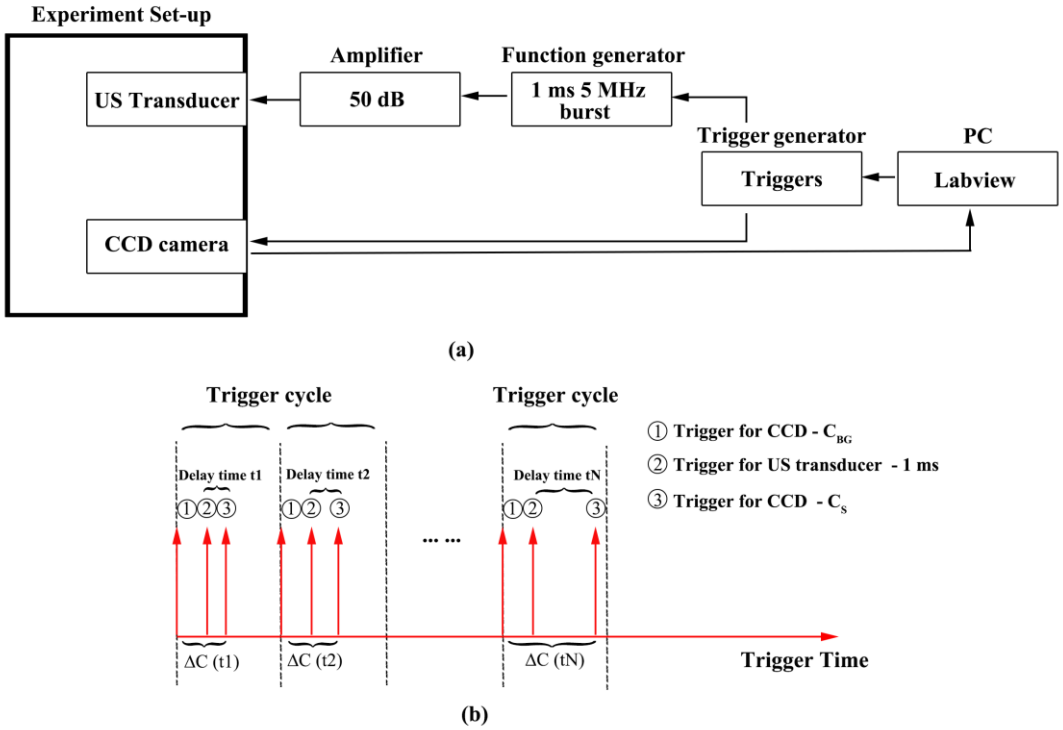

Figure 4.2 (a) Control system. The ultrasound (US) transducer and CCD camera are synchronised by the trigger generator controlled by Labview. (b) Trigger scheme. Three triggers within one trigger cycle and the delay time between trigger 2 and 3 (t1, t2, … ,tN) is increased by 0.2 ms successively. Trigger 1 and 3 are the triggers for the CCD exposure and trigger 2 is for the US burst generation.

4.3.2 Time-of-flight based calculation of shear wave speed

Figure 4.3 illustrates the method to obtain the shear wave speed, where Figure 4.3(a) is the front view of the set-up and Figure 4.3(b) is the expected signal of the shear wave. The acoustic axis (position A in Figure 4.3(a) is separated from the optical axis (position O) by a certain distance (DAO: distance between acoustic and optical axis). A shear wave is generated by transient ARF (1 ms US burst) at the position A, propagating toward the optical axis. The contrast difference ΔC increases as the shear wave approaches the optical axis and will have a peak when the peak of the shear wave arrives at the optical axis (position O). Figure 4.3(b) shows the expected ΔC

change with time. Δ*C* gradually increases until the peak and then decreases as the shear wave propagates away from the optical region. The time to peak (TTP1 in Figure 4.3b) is related to the distance between acoustic position A and the optical detection axis O (DAO1 in Figure 4.3a) and the shear wave speed.

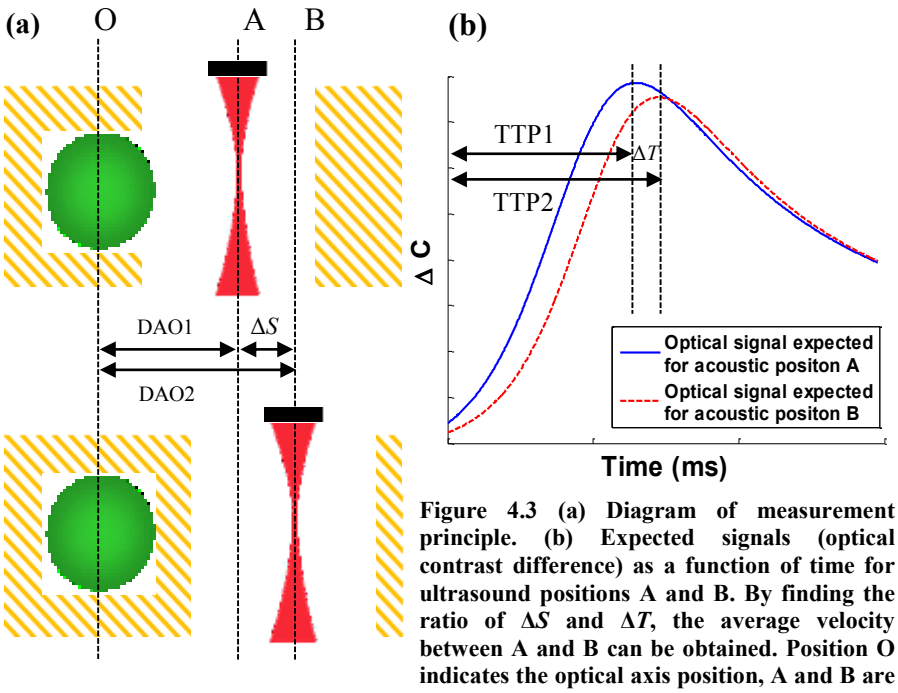

Figure 4.3 (a) Diagram of measurement principle. (b) Expected signals (optical contrast difference) as a function of time for ultrasound positions A and B. By finding the ratio of Δ*S* and Δ*T*, the average velocity between A and B can be obtained. Position O indicates the optical axis position, A and B are two different acoustic axis position.

Although the shear wave speed can be obtained by dividing DAO1 by TTP1 in Figure 4.3, a differential technique is proposed involving the ARF excitation at two positions (A and B in Figure 4.3a) in order to achieve improved spatial resolution and accuracy. If the position of the acoustic axis (and hence the shear wave origin) moves by ΔS from position A to position B while the optical axis stays unchanged, the peak in ΔC will shift in time by ΔT (Figure 4.3b). Through the knowledge of the time shift of the peak and the spatial distance between position A and B, the local shear wave speed between these two positions can be obtained by dividing ΔS by ΔT. In order to improve the accuracy, the timing of the peak was estimated after fitting each time of

flight curve shown in Figure 4.3(b) with a smoothing spline of a proper tolerance (MATLAB R2011a, spaps). Note that the decrease in the peak value of ΔC is due to the attenuation of the shear wave.

4.3.3 Phantoms

Homogeneous phantoms (93.5 mm × 42 mm × 20 mm) were created with three different agar concentrations (0.8%, 1.0%, and 1.2% agar powder) and 4% intralipid liquid to simulate the scattering properties of biological tissue [10]. A heterogeneous phantom consisting of two different stiffnesses was made. The phantom (93.5 mm × 42 mm × 20 mm) was created by two conjoined slabs of the same dimensions, one of which contained 0.8% agar and another one contained 1.2% agar. The intralipid was the same for both slabs, which was 4%. Finally, a phantom with a cylindrical mechanical inclusion was made. The background was made by 0.8% agar and inclusion was made by 1.2% agar. For both background and inclusion, 4% intralipid was added, giving a reduced scattering coefficient of 5 cm^{-1}. The radius of the inclusion was 3.5 mm.

Agar is chosen since the stiffness of phantom could be controlled by the agar concentration. In addition, agar solution hardly scatters light, which makes the optical scattering property is fully controllable with intralipid.

4.3.4 Initial measurements and validation

Initial measurements were made on the homogeneous phantoms to optimise the measurement parameters of the system. The optical axis (shown in Figure 4.1) was fixed and the US transducer was translated relative to it from 3 mm to 25 mm in steps of 1 mm (DAO in Figure 4.1 varied from 3 mm to 25 mm with 1 mm step size). By

quantifying the time shift of the peak in the speckle contrast for different DAOs, the shear wave velocity was obtained. This experiment allowed us to evaluate the influence of and determine the optimal values for the following two measurement parameters: a) the distance between the acoustic and optical axes (DAO) on the estimation of the time to peak (TTP); and b) the distance between the two US positions on the estimation of the shear wave velocity.

To independently test the Young's modulus obtained from the optical shear wave tracking method, a mechanical testing machine (Tinius Olsen H5KS) was used to compress phantoms and the obtained stress-to-strain curves were used to calculate the corresponding Young's modulus by

$$\boldsymbol{E = \frac{L}{A} \cdot \frac{F}{\Delta L}}, \tag{4-6}$$

where F is the compression stress measured with a force sensor, ΔL is the phantom strain along the direction of compression, and L and A are the phantom height and the size of phantom surface. [11]

Testing phantoms were the same homogeneous phantoms used in the optical measurement. The length of testing phantoms (46.6 mm) was cut to be half the length of the experiment phantom (93.5 mm) so that the contacted area (area of phantom up surface: 46.6 mm × 42 mm) was smaller than the area of the applicators (about 80 mm × 80 mm) and a uniform compression stress was ensured on the phantom surface during the test. Oil was applied to the applicators so the friction was minimised. The strain rate was kept to be 10e-2/s for all testing phantoms. The pre-load was kept as small as possible - the applicator was stopped once the reading meter changed to be nonzero. In addition, the slop of strain-stress curve could vary, depending on which

part is chosen in the strain-stress curve. Given the small strain due to the shear wave propagation in the optical experiment, I chose the part whose strain ranged between 0 and 3 mm to find the slope and thus the Young's modulus.

4.3.5 Measurement of the heterogeneous phantom

One-dimensional scan

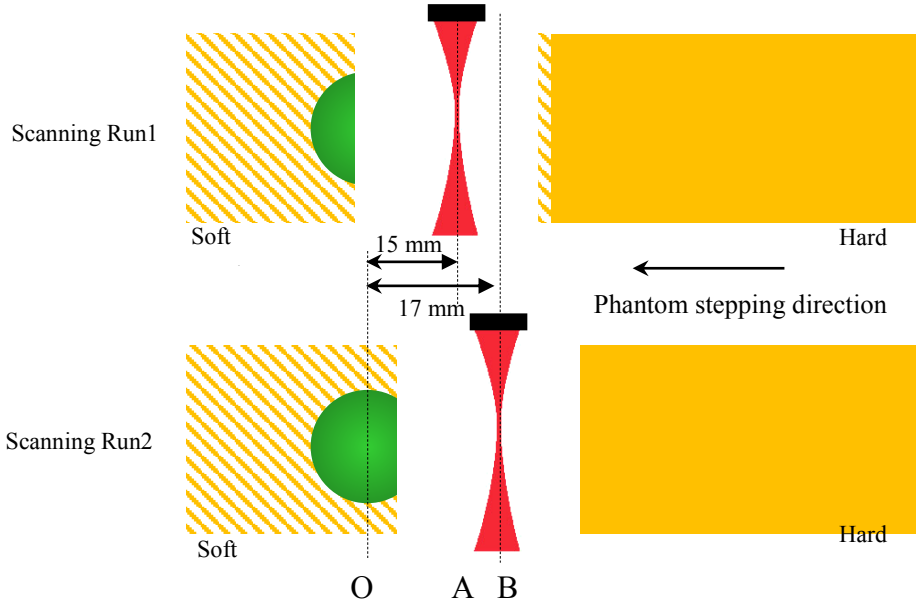

Figure 4.4 The scanning scheme for heterogeneous phantom. Position O indicates the starting position for optical axis in two scanning runs. A&B are two different acoustic axis positions.

Whereas the experiments carried out with the homogenous phantom where the optical axis and phantom were fixed and the acoustic axis was moved, in experiments with heterogeneous phantoms, only two DAOs (15mm and 17 mm) were chosen based on the initial study on the homogeneous phantoms (results shown in the results section). Figure 4.4 illustrates the scanning scheme for the heterogeneous phantom. For scanning run 1, 15 mm DAO is used and the phantom stepps along the direction indicated in the figure with 1 mm step size. For scanning run 2, the phantom is back to the original place to make sure the optical axis is the same with run 1 and the DAO

is modified to 17 mm. The scanning started with the US axis fully in the softer section of the phantom and was stepped toward the stiffer part. The measurement was repeated three times to evaluate the repeatability and noise.

Two-dimensional scan

The phantom with a mechanical inclusion was scanned in two-dimensions (2-D) at a spatial step of 1 mm in both directions. A spatial map of the Young's modulus was built based on a single scan with DAOs of 15 and 17 mm. A spatial smoothing Gaussian kernel (size: 5 mm, sigma: 2 mm) was used to post-process the image.

Finally in order to test the sensitivity of optical detection of weak shear waves, the homogeneous phantoms was measured with a fixed optical axis while the acoustic axis was moved in 1 cm step from 4 cm to 7 cm away from the optical axis.

4.4 Results

4.4.1 Initial measurements on the homogenous phantom and validation

The shear wave propagation in the homogeneous phantoms with different stiffnesses was studied. The experimental results are shown in Figure 4.5, where the y-axis presents different DAOs, the x-axis is the time and the colour is the speckle contrast difference (ΔC), which is warmer for larger ΔC. The maximum value of ΔC is decreasing as the DAO rises due to the attenuation of shear wave, and different phantoms have different ΔC values due to different stiffnesses. To further analyse the data and calculate the shear wave speed, TTP for each phantom at each DAO was found and plotted in Figure 4.6, where the x-axis is the DAO and the y-axis is the TTP. Regardless of the different optical volumes through the phantom due to different optical scattering, the relationship between different DAOs and TTPs was found to be linear when the acoustic axis was not close to the optical axis, as

expected. However, the slopes deviate from the linear trend for smaller DAOs for reasons described in the discussion section. The rate at which TTP changed for different transducer positions was evaluated using linear fitting for the data from a 10 mm DAO onwards. The inverse of the slopes for these three fitted lines represent the shear wave speed of the respective material.

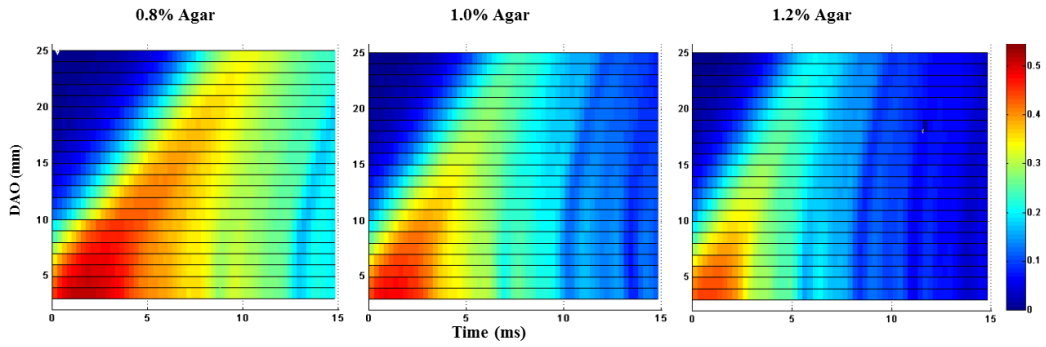

Figure 4.5 Optical contrast difference (Δ*C*) as a function of time for 23 different DAOs (from 3-25 mm in 1 mm steps) in three homogenous phantoms of different stiffness.

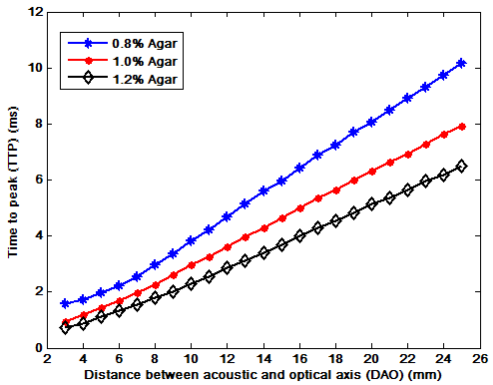

Figure 4.6 TTP changes with DAO (3-25 mm, 1 mm step size)

Table 4 - 1 Young's modulus of phantoms measured from mechanical testing machine and optical detection

Phantoms	Shear wave velocity (Optical method)	Young's modulus (Optical method)	Young's modulus (Mechanical test)	Deviation
0.8% agar	2.37 m/s	16.86 kPa	17.96 kPa	6.52 %
1.0% agar	3.01 m/s	27.18 kPa	26.52 kPa	2.47 %
1.2% agar	3.57 m/s	38.23 kPa	35.47 kPa	9.78 %

Table 4.1 compares the results when using the optical and mechanical methods. The

Young's modulus was found to increase with the increase of agar concentration. The deviation between the optical and mechanical methods is small and is no more than ± 10%. Note that all the density of phantoms was assumed to be 1000 kg\m^3.

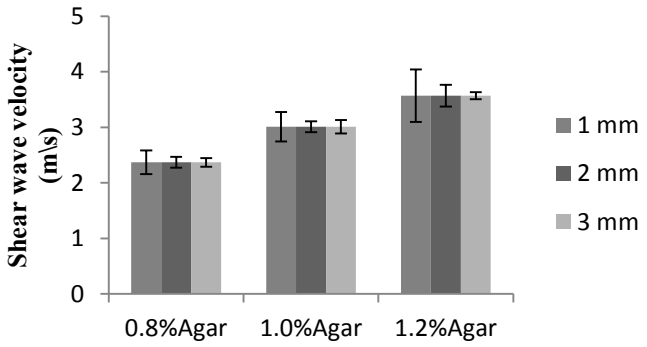

Figure 4.7 Estimated shear wave velocities in different phantoms with three separations between two DAOs (DAO ranged from 10 mm to 25 mm).

To calculate the local shear wave velocity, two DAOs were required for our proposed differential method. DAO determines the signal-to-noise ratio (SNR) for optical detection as the larger the DAO, the smaller the shear wave amplitude due to attenuation. On the other hand, the relationship between the DAO and time to peak becomes nonlinear when DAO is small (see the beginning part of the curves in Figure 4.6). Considering both factors, 15 mm was chosen to be one of the DAO. For the other DAO, two conditions were considered: a) the separation for the two DAOs determines the spatial resolution of the system so the smaller the separation the better resolution; b) the separation for the two DAO also affects the accuracy of the shear wave speed estimation. The results in Figure 4.7 were calculated when the separation of two DAOs was 1 mm, 2 mm and 3mm respectively. It can be seen that generally the larger the separation, the smaller the standard deviations in the calculated shear wave speed. The standard deviations for the hard phantom are calculated to be 0.47

(13%), 0.20 (5.5%) and 0.07 (1.9%) for the three differences in DAO, respectively, comparing to 0.26 (8.8%), 0.10 (3.3%) and 0.21 (3.1%) for the medium stiffness phantom. Therefore, a balance must be made between the estimation SNR and spatial resolution. In the subsequent study, the distance between the two US positions was chosen to be 2 mm and two DAOs chosen for subsequent studies were 15 mm and 17 mm.

4.4.2 Results for the heterogeneous phantom

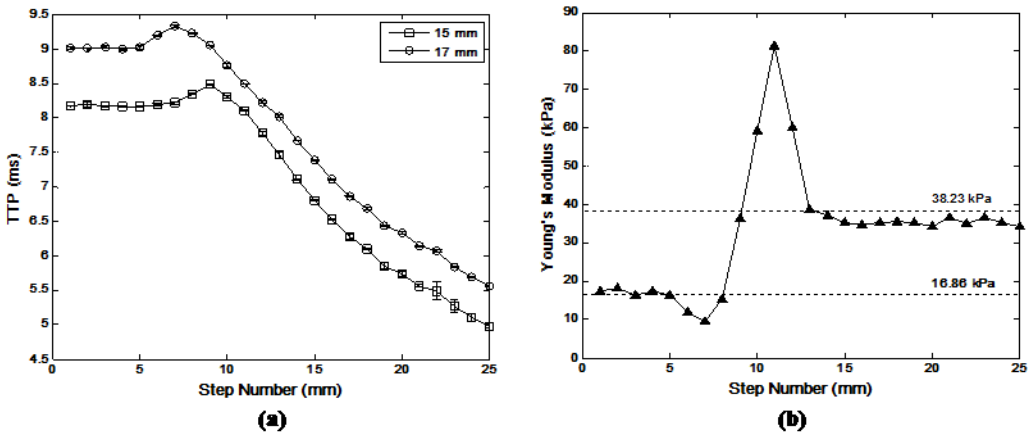

Figure 4.8 TTP at each step (a) and calculated Young's modulus (b). Error bars result from the optical variation. The dashed lines are the expected value from previous experiments.

Figure 4.8(a) shows the time to peak (TTP) as a function of spatial scanning steps for two DAOs. For each curve in Figure 4.8(a) the TTP value varies depending on the elasticity properties between the acoustic and optical axis, while the difference between the two curves corresponds to the time taken by the shear wave to travel between the two DAOs. Based on these, the Young's modulus (E) for the phantom were evaluated and shown in Figure 4.8(b). From Figure 4.8(b), it can be seen that the results are consistent with the expected values (dash lines) except for those at the boundary between the soft and hard slabs of the phantom. The slight difference

between the calculate Young's modulus and the expected value away from the soft-hard boundary is due to the variations in the phantom making process. It can also be seen that each TTP curve in Figure 4.8(a) shows an unexpected maxima when the US focus is close to the boundary. One possible reason for this is the shear wave reflection at the boundary where reflected wave constructively overlapped with the original wave and delayed the shear wave peak. This results in the delay of peak time in optical measurements. It should be noted that the variations in each measurement in Figure 4.8 were less than 1% and hence the error bars were omitted.

4.4.3 Investigation of shear wave reflection near the phantom soft-hard boundary

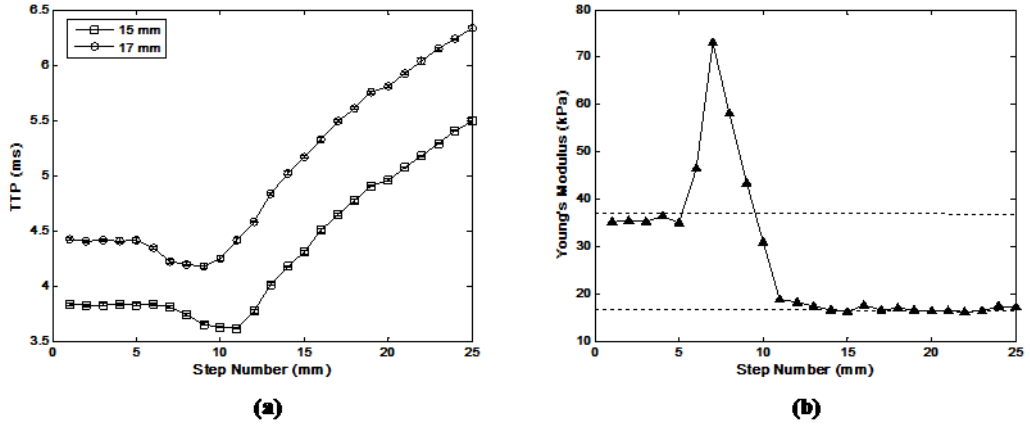

Figure 4.9 Time to peak (TTPs) for each scanning step (a) and calculated Young's modulus (b). The dashed lines are the expected value from table 4-1.

In order to investigate whether the shear wave reflection is the cause for the maxima in Figure 4.8(a) and estimation inaccuracy in elasticity in Figure 4.8(b), the phantom was rotated 180 degrees so the scanning was carried out starting from the stiff (1.2% agar) slab toward the soft (0.8% agar) slab. In this case the shear wave reflection should destructively interfere with the initial shear wave and makes the TTP shorter, causing dips in the TTP at the boundary. These expected dips are shown in Figure 4.9.

The calculation of Young's modulus shows the estimation accuracy of our system (Figure 4.9(b) where the dashed lines are the expected values) except for that near the soft-hard boundary. It is notable that the peak values of Young's modulus in two experiments differ slightly (around 85 kPa and 70 kPa respectively). This is likely because the distance between the acoustic axis and the soft-hard boundary was not the same in two experiments, resulting in changes of the overlap between reflected and original wave.

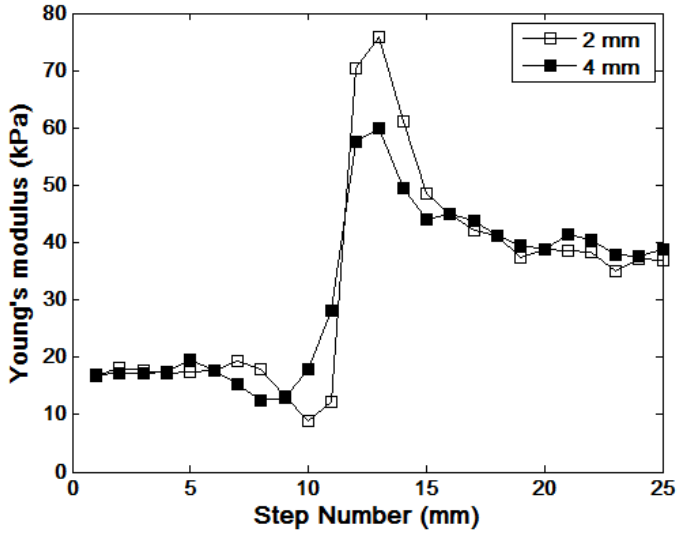

Figure 4.10 Comparison between 2 mm separation and 4 mm separation

One method to reduce the boundary effect is to increase the separation of the two transducer positions, as it will make the interference by reflection a lesser part of the total wave travel time. Figure 4.10 plots the results for 2 mm (15 mm and 17 mm for DAOs) and 4 mm (15 mm and 19 mm for DAOs) separations of two transducer positions. As shown, the accuracy of Young's modulus measured at the boundary is increased by increasing the separation between two transducer positions, at the expense of spatial resolution of the system.

4.4.4 Results for 2D scan

Figure 4.11 shows the result for the 2-dimensional scanning of the phantom with an inclusion. The DAOs of 15 and 17 mm were used to obtain these data. The position of the inclusion is indicated by the dashed circle with which the obtained 2-D image agrees well. The averaged estimated Young's modulus of the inclusion is approximately 55 kPa in the figure which is higher than the 38 kPa resulting from the homogenous phantom measurements. The overestimation of the Young's modulus is likely because of the wave reflection at the boundary as well as the variations during the fabrication of the phantoms.

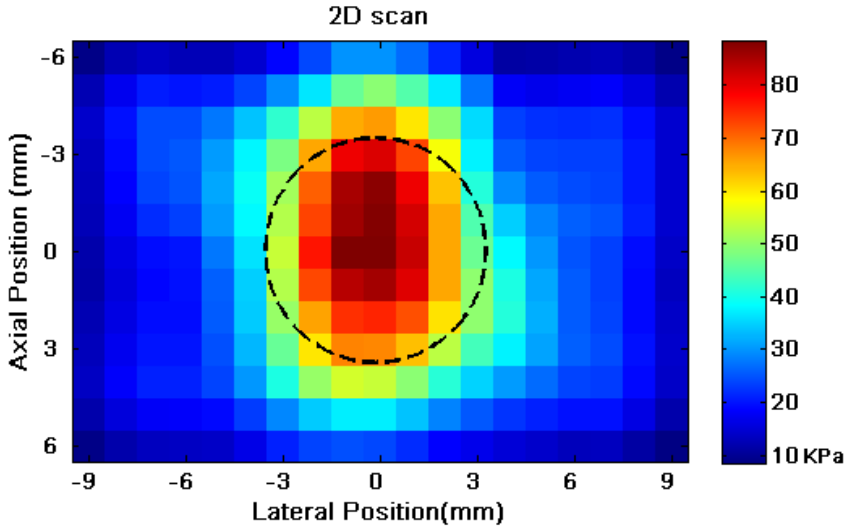

Figure 4.11 Two dimensional scan of a phantom with a cylindrical stiff inclusion (3.5 mm in radius). The figure shows only shows part of the phantom with the inclusion along the optical axis.

4.4.5 Sensitivity study

To study the sensitivity of our optical detection of the shear wave, some large DAOs were used for measurements. In this case the optical axis was fixed while the acoustic axis was positioned at various distances from the optical axis up to 7 cm with 0.4 cm interval starting from 4 cm away from the optical axis. Figure 4.12 shows that even

for 7 cm DAO, the shear wave propagation still can be detected with a decent SNR (see the last curve on the right in Figure 4.12).

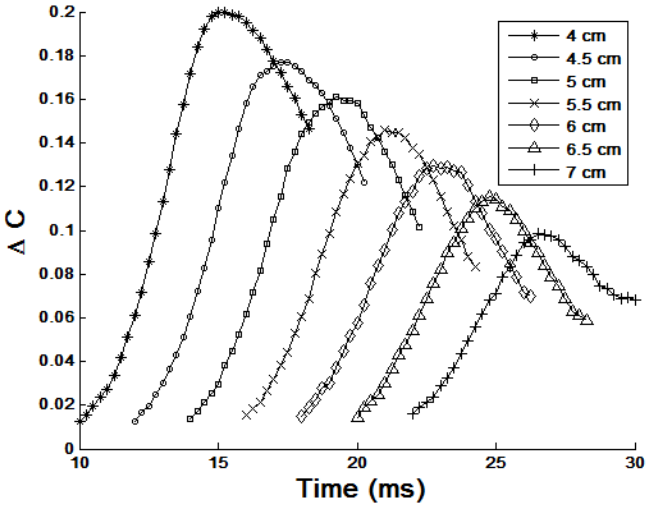

Figure 4.12 ΔC change as the function of time with various DAOs

4.5 Discussion and Conclusions

An experimental set-up based on a laser source and optical detection has been proposed that noninvasively measures the local speed of a shear wave generated by the transient acoustic radiation force. This potentially offers a useful tool for measuring tissue elasticity *in vivo*. By studying homogeneous and heterogeneous phantoms, it has been shown that the proposed technique is feasible for tracking the shear wave propagation in tissue mimicking phantoms and to quantify local tissue elasticity. It should be noted that the proposed technique is a differential technique that depends only on the difference in measurements for the two US positions. Any heterogeneity between the acoustic and optical axes should not affect the results significantly if the DAOs are much greater than the distance between the two ultra-sound positions.

Compared with existing techniques that mainly use US tracking, the proposed set-up

with optical tracking is potentially much more sensitive as it can detect tissue displacement of nanometres [9], which potentially allows for a much more reliable estimation of tissue stiffness. In this study, the optical measurements of tissue motion are still well above the noise even when the shear wave has propagated and been attenuated through 7 cm of the phantom. However, it should be noted that the propagation distances over which shear wave is still detectable are dependent upon the initial displacement of the tissue and the material properties. Therefore, further measurements in biological tissue are required to confirm the working range of the DAO for the system.

Compared with US detection of shear waves, optical measurements are less sensitive to tissue displacement at a depth beyond a few centimetres because light is highly scattered in tissues. However, the high sensitivity of the optical measurements means weak shear waves may still be detected as they propagate to the surface, that is to say, surface or subsurface optical measurements may detect a shear wave generated deep within tissue and with the differential method, the elasticity could be quantified even if the light cannot penetrate to the deep tissue.

The presence of elasticity boundaries and shear wave reflections has a significant impact on the elasticity estimation and introduces bias. I have shown that the reflection effect can be reduced at the expense of the spatial resolution. It should be noted that this reflection phenomenon is common to all techniques that are based on tracking the shear wave propagation. In ultrasound-based elastography, a directional filter could be used to remove the motions that move other than the shear wave propagation direction [12]. It would be interesting to test with my system in the further.

The speed estimation is biased when the US focus is close to the centre of the laser beam which is attributable primarily to the finite size of the volume that the laser illuminates. When the DAO is small, the shear wave is generated within the laser-illuminated volume. In this case, the optical detection tracks the shear wave propagation in both directions, which biases the time to peak measurements. This bias could also result from the shear wave near-field diffraction effects, which means the shear wave needs to be a few millimetres outside the excitation region to observe a linear propagation trend.

Due to the availability of the mechanical test machine, only one set of phantoms (one homogenous phantoms for each agar concentration) were tested and the corresponding optical measurements were listed in Table 4.1. Repeated tests are required to further validate my method. Secondly, the result of mechanical test is affected by several factors, such as the shape and size of the phantoms, the strain rate and the amount of pre-compression [11]. Therefore, the same protocol should be followed for each test to improve the reproducibility. In addition, the two experiments were conducted at different rooms in different days. It is desirable to test the same phantoms with both of the methods in the same room within a short gap time, such that the errors due to the temperature change, moisture change could be minimised.

As mentioned, the result in Table 4.1 needs to be further validated by repeating both of the experiments with more samples. However, the discrepancies between the two methods may result from the reflected shear waves from the phantom-tank boundaries which interfere with the original shear wave, deviating the timing of peak and thus the measured shear wave speed. These artificial boundaries do not exist in practical.

In conclusion, a highly sensitive shear wave elasticity imaging technique based on

optical measurements was proposed to quantify tissue mechanical properties. The feasibility and accuracy of this technique has been studied. The reflection of shear waves near elasticity boundaries and the bias caused to the estimation of elasticity were studied and by using larger distances between acoustic excitations, this effect was reduced at the expense of system resolution.

References

1. Sarvazyan, A.P., O.V. Rudenko, and W.L. Nyborg, *Biomedical Applications of Radiation Force of Ultrasound: Historical Roots and Physical Basis.* Ultrasound in Medicine & Biology, 2010. **36**(9): p. 1379-1394.

2. Oliphant, T.E., et al., *Complex-valued stiffness reconstruction for magnetic resonance elastography by algebraic inversion of the differential equation.* Magnetic Resonance in Medicine, 2001. **45**(2): p. 299-310.

3. Sandrin, L., et al., *Shear modulus imaging with 2-D transient elastography.* Ultrasonics, Ferroelectrics and Frequency Control, IEEE Transactions on, 2002. **49**(4): p. 426-435.

4. Bercoff, J., et al. *Ultrafast imaging of beamformed shear waves induced by the acoustic radiation force. Application to transient elastography*. in *Ultrasonics Symposium, 2002. Proceedings. 2002 IEEE*

5. Bercoff, J., M. Tanter, and M. Fink, *Supersonic shear imaging: a new technique for soft tissue elasticity mapping.* Ultrasonics, Ferroelectrics and Frequency Control, IEEE Transactions on, 2004. **51**(4): p. 396-409.

6. Rouze, N.C., et al., *Robust estimation of time-of-flight shear wave speed using a radon sum transformation.* Ultrasonics, Ferroelectrics and Frequency Control, IEEE Transactions on, 2010. **57**(12): p. 2662-2670.

7. Joyce, M. and R. Daniel, *Shear wave speed recovery in transient elastography and supersonic imaging using propagating fronts.* Inverse Problems, 2006. **22**(2): p. 681.

8. Elson, D.S., et al., *Ultrasound-mediated optical tomography: a review of current methods.* Interface Focus, 2011. **1**(4): p. 632-648.

9. Li, S., et al., *Tracking shear waves in turbid medium by light: theory, simulation, and experiment.* Optics Letters, 2014. **39**(6): p. 1597-1600.

10. Daoudi, K., A.-C. Boccara, and E. Bossy, *Detection and discrimination of*

optical absorption and shear stiffness at depth in tissue-mimicking phantoms by transient optoelastography. Applied Physics Letters, 2009. **94**(15): p. 154103-154103-3.

11. Wells, P.N.T. and H.-D. Liang, *Medical ultrasound: imaging of soft tissue strain and elasticity.* Journal of The Royal Society Interface, 2011.

12. Deffieux, T., et al., *On the effects of reflected waves in transient shear wave elastography.* Ultrasonics, Ferroelectrics and Frequency Control, IEEE Transactions on, 2011. **58**(10): p. 2032-2035.

Chapter 5

Detecting optical and mechanical properties with ultrasound modulated optical tomography in a reflection detection geometry

This chapter describes a dual-mode system capable of sensing both optical and mechanical properties in a reflection detection geometry. My system characterises both the optical and the mechanical properties of the material in comparison with ultrasound modulated optical tomography or elasticity measurement alone which only detect one or the other. Moreover, by detecting the backward scattered light in a reflection detection geometry, the system is more suitable for clinical applications compared with the transmission geometry.

5.1 Introduction

Measuring the optical and mechanical properties of biological tissue provides complementary information for clinical diagnosis. In this chapter, I combined the optical elastography system with UOT to create a dual-mode UOT system which is able to simultaneously sense tissue mechanical and optical properties. Qualitative optical property is obtained by UOT scans when the signal is reduced at locations with high optical absorption. Quantitative stiffness is measured by the differential method (SW-LASCA) proposed in Chapter 4. Tissue mimicking phantoms with multiple inclusions buried at 11 mm depth were experimentally scanned with the dual-mode system. The inclusions, with higher optical absorption and/or higher stiffness than background, were identified based on the dual results. I also designed the dual-mode UOT system operating in a reflection mode where the laser and the

CCD camera were positioned on the same side of tissue-mimicking phantoms. Compared with the transmission detection geometry, the reflection geometry is expected to be more practical in clinical applications where light cannot penetrate through the structure of interest.

5.2 Method

5.2.1 Experimental set-up

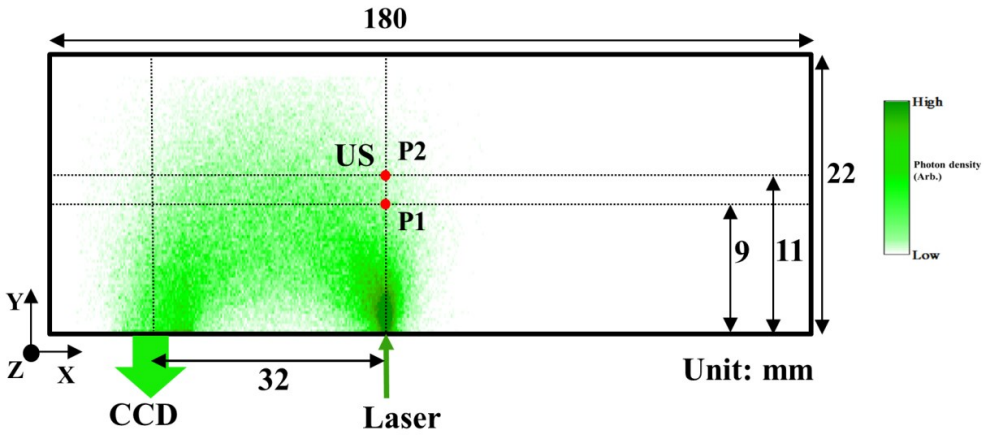

Figure 5.1 Top view of experimental set-up. The ultrasound (US) and laser are perpendicular with each other. The US propagates into the paper and is focused at P1 and P2 which are on the laser axis. The CCD camera and laser are positioned on the same side of the phantom to detect the photons in the reflection geometry.

A 50 mW continuous 532 nm Nd:YAG laser and a CCD camera were positioned 32 mm apart on the same side of tissue mimicking phantoms to collect the backward scattered photons (see Figure 5.1). A 5 MHz focused ultrasound transducer was used to deliver 2 ms ultrasound bursts propagating perpendicular to the laser axis into the phantom. The ultrasound bursts not only modulated the photons passing through but also generated the ARF and the subsequent shear wave. Figure 5.1 shows the top view of the experimental system. The green area in the phantom is the simulated photon probability density of the scattered light (log-compressed) predicted by Monte Carlo simulation [1]. In the simulation, the optical absorption coefficient $\mu_a =$

$0.2\ \mathrm{cm}^{-1}$, the optical scattering coefficient $\mu_s = 30\ cm^{-1}$ and the anisotropic coefficient g = 0.8, which were similar to the properties of the phantoms used in experiment [2]. As expected, a typical 'banana shape' light distribution is found where the highest photon probability density - indicating the most sensitive light detection area - is presented near the laser source. P1 and P2 are two positions separating by 2 mm along the laser axis and also where the ultrasound bursts were focused. The ultrasound burst (and thus the ARF) was launched at separate times at P1 and P2, modulating the light passing through the ultrasound focal region and generating a shear wave propagating towards the light detection volume. The ultrasound and ARF modulated light and the shear wave modulated light were both detected with a time-resolved CCD speckle contrast difference signal (ΔC (t)).

5.2.2 UOT and SW-LASCA measurement

At t = 0 ms, the signal (ΔC (0)) is acquired immediately after the ultrasound burst and before the spreading of the shear wave. Therefore, it mainly results from the modulation of the ultrasound/ARF and is regarded as the UOT signal. The resolution of UOT is about 1 mm, that is, equal to the lateral width of the ultrasound focal region. As the propagation of the shear wave away from the ultrasound focal region, ΔC (t) is caused by the modulation of the shear wave and thus regarded as the signal of the SW-LASCA. Therefore, the separation of the ultrasound/ARF modulation and shear wave modulation is based on the CCD delay time. ΔC (t) peaks when the shear wave propagates to the most sensitive optical detection area (near the laser source), and the timing for the peak is related to the shear wave speed.

In order to measure local shear wave speed, signals were acquired for both P1 and P2 and the difference in the timing of the peaks (Δt) in the two contrast difference signals

indicated the time-of-flight of the shear wave between P1 and P2 (ΔS = 2 mm). The averaged shear wave speed between P1 and P2 was then calculated by Cs=ΔS/Δt, and the shear modulus was calculated by $\mu = 3Cs^2\rho$, where ρ=1000 kg/m3 was the density of the phantom.

5.2.3 Phantom and data acquisition

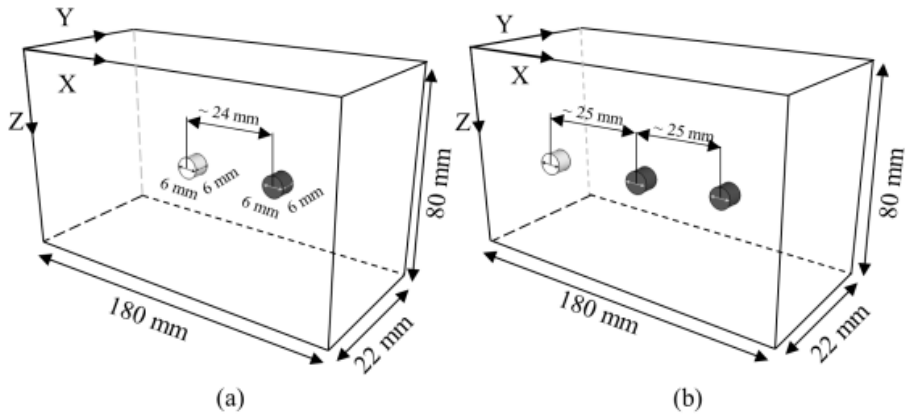

Figure 5.2 (a) Schematic of the two-inclusion phantom; (b) Schematic of the three-inclusion phantom

A 180 × 80 × 22 mm heterogeneous phantom was constructed with two cylindrical inclusions (6 mm diameter, 6 mm length, one mechanically stiff and one optically absorbing) separated by 24 mm and buried in the middle (Figure 5.2(a)). Figure 5.5(a) is a photo of the phantom cross section (X-Z plane). The surrounding medium was made of 0.8% agar powder and 4% Intralipid solution. By adding 0.1% black ink the optical inclusion had a larger optical absorption coefficient (dark area in the photo), and the mechanical inclusion was made stiffer by increasing the agar powder concentration to 1.2% (depicted by the red circle in the photo in Figure 5.5).

Another phantom was constructed with an additional third inclusion made of 1.2% agar powder, 4% Intralipid solution and a small amount of black ink (Figure 5.2(b) and Figure 5.6 (a)). Thus, it had higher stiffness and optical absorption than the

background. The size of the whole phantom and inclusions were the same as in the previous phantom while the distance between two adjacent inclusions was about 25 mm.

In a first experiment, the two-inclusion heterogeneous phantom was scanned twice with the ultrasound focused at P1 and P2, starting on the left side of the mechanical inclusion (Start point in Figure 5.5 (a)) and ending when the laser axis moved to the right side of the last inclusion (End point in Figure 5.5(a)). The 1D scans were recorded by stepping the phantoms with 1 mm intervals in the x-direction for 60 mm while the ultrasound, the light and the CCD were held stationary. At each position a contrast difference signal was acquired by delaying the 2 ms CCD exposure from 0 ms to 10 ms with time steps of 0.2 ms after the launch of the 2 ms ultrasound burst. Due to the limited frame rate of the CCD, the data could not all be acquired for a single shear wave and, instead, multiple cycles were used, with a delay between launching consecutive shear waves to allow for mechanical relaxation. The ultrasound negative-pressure at the focus was 5.6 MPa and the measurement was repeated three times at each position for averaging later. In a second experiment, the three-inclusion heterogeneous phantom was used and the same scanning scheme was adopted, but the phantom translation was 75 mm with 1 mm steps (Figure 5.6 (a)) and the ultrasound negative-pressure at the focus was reduced to 4.4 MPa to demonstrate the feasibility of reducing ultrasound pressure.

Table 5 - 1 Parameters in dual-mode UOT experiments

Ultrasound Frequency	5 MHz
Ultrasound Burst Length	2 ms
Ultrasound Negative Pressure at Focus	5.6 MPa/4.4 MPa
CCD Iris Size	11 mm
CCD Exposure Time	2 ms
CCD Delay Step Size	0.2 ms

Table 5.1 shows the parameters used for the dual-mode UOT. Instead of using 1 ms ultrasound burst length as in the previous chapter, I used 2 ms burst length in the work described in this chapter to accord with 2 ms CCD exposure time. In this way, the UOT signal could be maximised by continually modulating photons with ultrasound during the CCD exposure time. The ultrasound negative pressure at the focus used was 5.6 and 4.4 MPa. The reason to use a relatively high pressure was to maximise the signal-to-noise ratio in this proof-of-concept experiment. It can be further reduced by optimising other parameters and the system platform (as will discuss later). It should be noted that negative-peak pressure of ultrasound is directly linked to mechanical index which is a safety index of using ultrasound clinically [3]. The iris size used was 11 mm, which was chosen according to Figure 5.4 where the contrast difference reaches a plateaux around 11 mm. The CCD delay step size was 0.2 ms, meaning t(1) was 0 ms after the burst, t(2) was 0.2 ms after and so on.

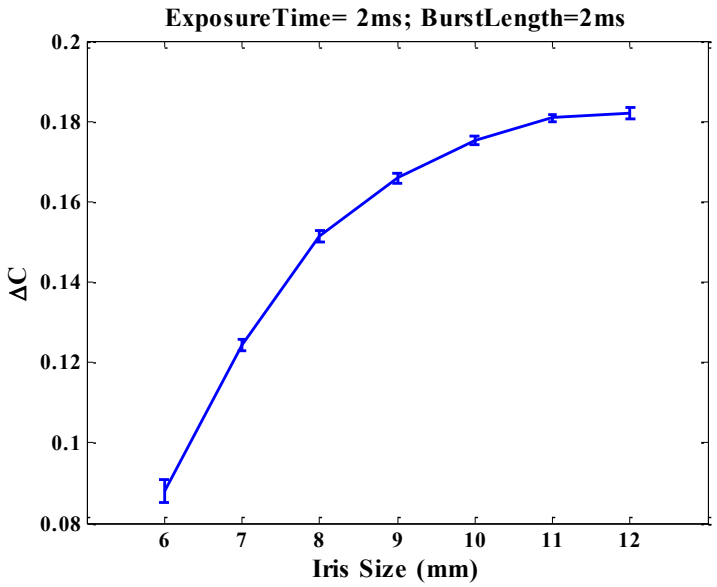

Figure 5.3 contrast difference change with CCD iris size

5.3 Results

5.3.1 UOT and SW-LASCA measurements

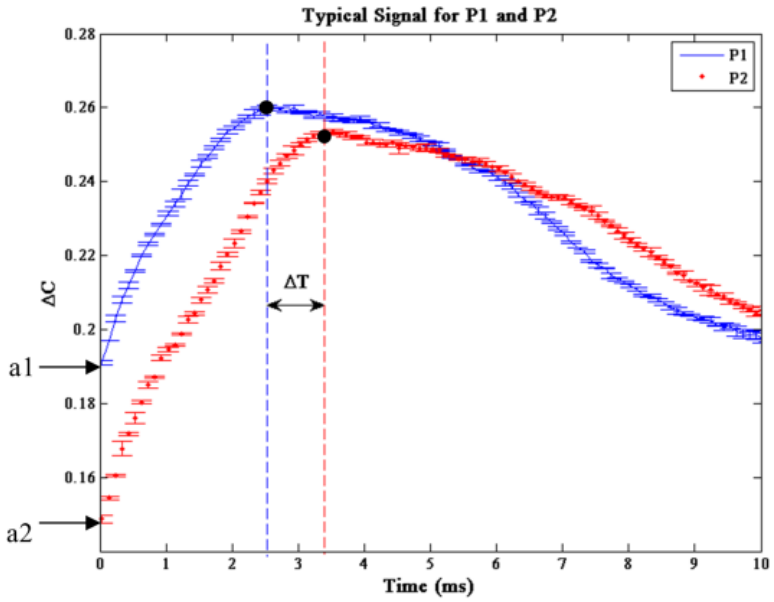

Figure 5.4 Typical contrast difference signals for P1 and P2. The time delay between the two peaks results from the 2 mm distance between P1 and P2. a1 and a2 are the UOT signal which results from the modulation of ultrasound/ARF. The error bars are from three repeated measurements.

Figure 5.4 presents the time-resolved contrast difference signals detected when the ultrasound was focused at P1 (blue curve) and P2 (red curve) for a translation step without inclusion in the light volume. Both signals peak when the shear wave reaches the most sensitive area near the laser source. The signals at t = 0 ms (a1 and a2 in Figure 5.4) were the UOT signals which resulted from the modulation of the ultrasound and ARF. The magnitude of a2 is smaller than that of a1 because P2 was further from the laser entry point than P1 and therefore fewer photons were modulated. The timing of the peaks of the two curves indicated by vertical dashed lines in Figure 5.4 corresponds to the time at which the shear wave arrived at the most sensitive detection volume. Therefore, the time difference (ΔT) was the time-of-flight of the shear wave between P1 and P2, which allows the shear wave speed to be

calculated as the ratio of 2 mm and ΔT, and thus the distance between P1 and P2, which is 2 mm in the experiment, is the resolution of the SW-LASCA measurement.

5.3.2 1D scan

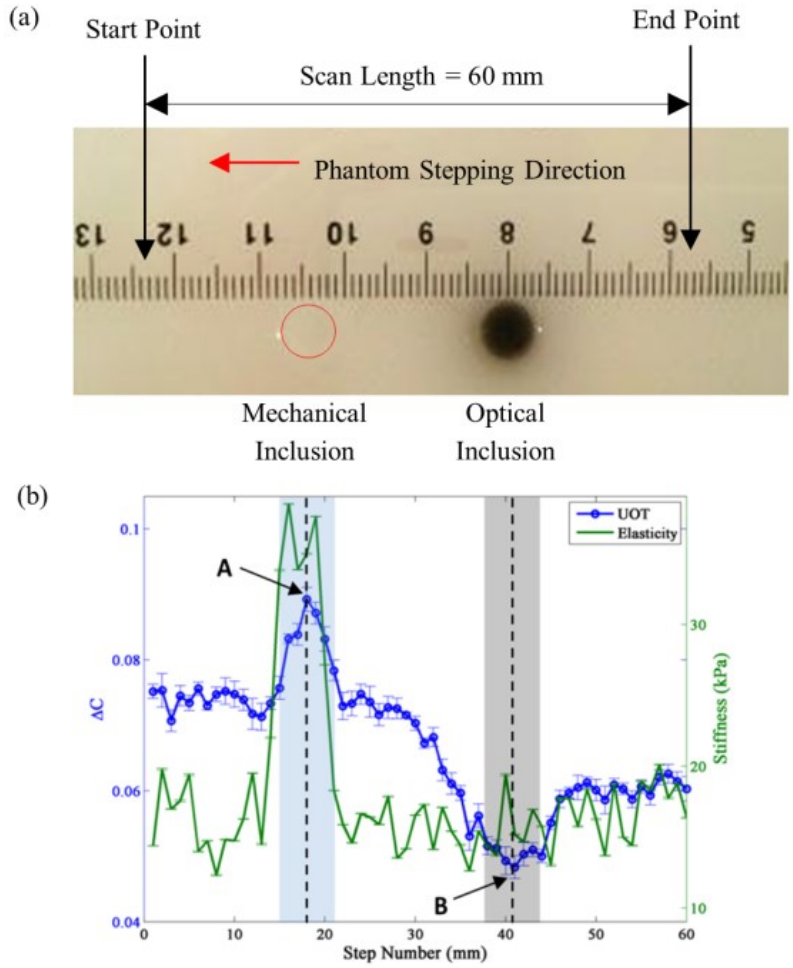

Figure 5.5 (a) Photo of the cross section of the two-inclusion heterogeneous phantom. (b) 1D scan result for the two-inclusion heterogeneous phantom. The standard deviation was from three repeated measurements at each step position. The locations of inclusions are indicated by the shaded areas. A and B are the positions of the maximum and minimum contrast difference.

The results of the 1D scan for the phantom are shown in Figure 5.5(b) where the blue curve is the UOT signal from P2 while the solid curve shows the stiffness of the phantom calculated using $\mu = 3Cs^2\rho$. The data when the ultrasound focus was at P2 was used as the UOT signal because it is 2 mm deeper than P1 in the phantom and

better demonstrated the image depth capability of UOT. The error bar at each scan position is the standard deviation from three repeated measurements at the same position. The positions of the inclusions are indicated in the photo of the phantom cross section (Figure 5.5(a)) and the shaded areas (Figure 5.5(b)) in the graph.

For the UOT measurement (blue curve), the signal alters within both inclusions, increasing in the mechanical inclusion and decreasing in the optical inclusion. The two positions that bound the maximum range of contrast difference are marked as A and B respectively. The distance between A and B is 23 mm which is 1 mm different from the inclusion separation of 24 mm, but the resolution of the UOT measurement is about 1 mm, equal to the lateral width of the ultrasound focus region. The full width at half maximum (FWHM) of the measurements of the two inclusions are 5.1 mm and 10.9 mm respectively, suggesting higher spatial accuracy for the UOT measurement of the mechanical inclusion. The FWHM is defined as the one-way distance between 50% of the maximum over the two baselines before and after the inclusion. The signal was firstly fitted by a smooth spline function (MATLAB, spaps) and the FWHM was then calculated.

Table 5 - 2 Stiffness of phantom measured with optical detection and an independent compression test

Phantom	Stiffness (Optical)	Stiffness(Mechanical)	Deviation
0.8% Agar	16.19 kPa	17.96 kPa	9.86%
1.2% Agar	34.12 kPa	35.47 kPa	3.55%

For the SW-LASCA measurement (green curve), the y-axis indicates the magnitude of the stiffness which increases within the mechanical inclusion but not in the optical inclusion, as expected. Table 5.2 is a comparison between the stiffnesses measured in the experiment and in a previous study where the stiffnesses were obtained with an

independent mechanical compression test [4]. As shown, the deviation between the optical (second column) and mechanical (third column) methods is no more than 10%.

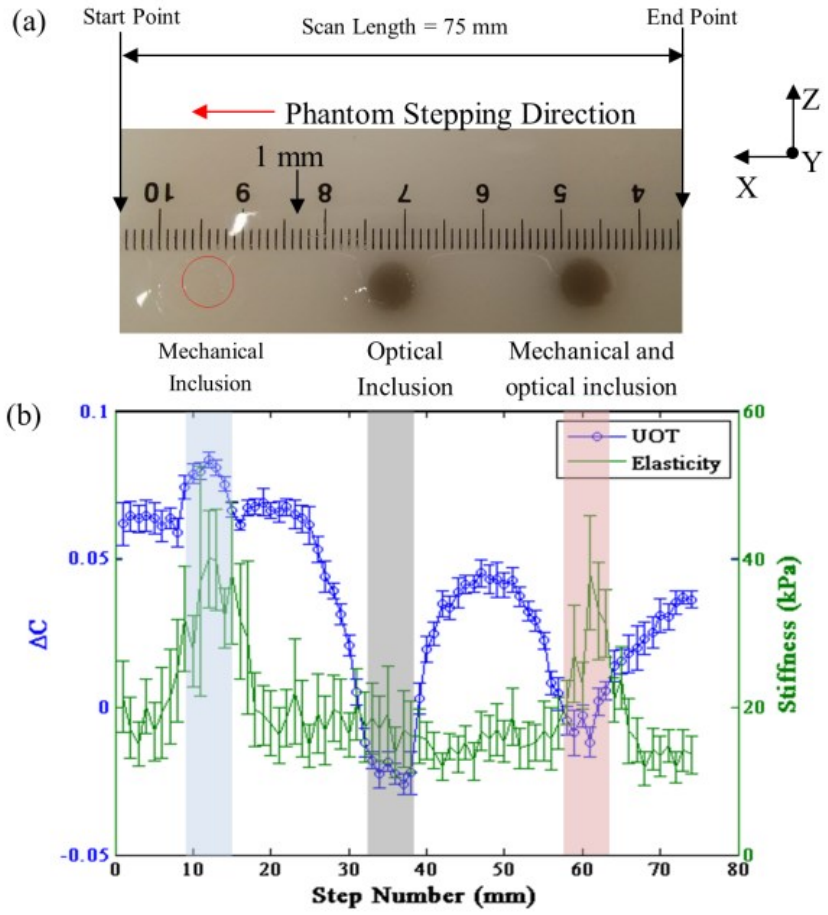

Figure 5.6 Dual shear wave results for the three-inclusion heterogeneous phantom. (a) Photo of the phantom cross section where the three inclusions from the left to right are for mechanical (red circle), optical (dark spot) and combined mechanical and optical contrast (dark spot). They are separated by ~25 mm from each other. The red arrow indicates the phantom stepping direction and the total stepping length is 75 mm. (b) UOT and elasticity measurements. The blue solid curve with circular points is the UOT signal for P2 and the green solid line is the stiffness. The error bars are the standard deviations of three repeated measurements at each stepping position. The positions of the inclusions are indicated by the shaded areas in the figure

Figure 5.6 shows the dual results for the three-inclusion phantom where the blue curve shows the UOT signal and the green curve is the stiffness measurement. The error bars are the standard deviation of the three repeated measurements at each

position. The UOT signal increased in the mechanical inclusion (FWHM 5.2 mm) and decreased in both the optical inclusion (FWHM 10.1 mm) and the combined mechanical and optical inclusion (FWHM 8.5 mm). The elasticity measurements showed that the stiffness of the mechanical inclusion and the combined mechanical and optical inclusion are higher than that of the optical inclusion and the background, as expected. The three inclusions were easily identified and their qualitative optical absorption and quantitative mechanical properties were obtained.

5.3.3 Investigation of the unexpected trend in the UOT signal

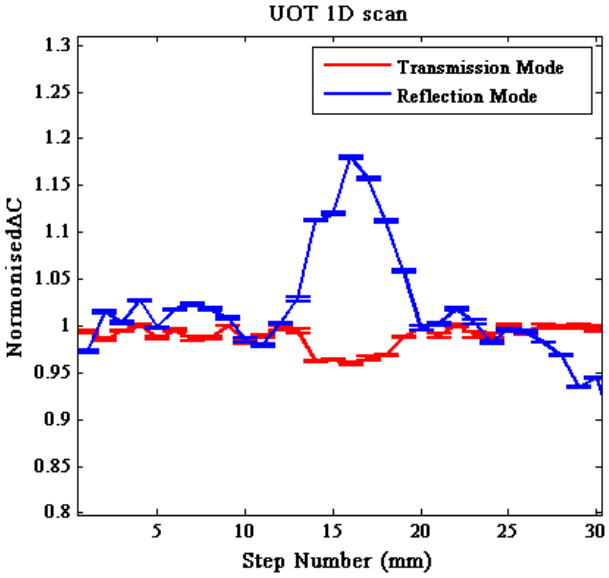

Figure 5. 7 UOT signals with transmission mode and reflection mode

In Figure 5.5 and 5.6, the UOT signal was expected to decline within the mechanical inclusion because the modulation from the ultrasound and ARF should decrease in the mechanical inclusions where the displacement of optical scatterers due to the ultrasound propagation is smaller compared with the surrounding medium given the same ultrasound pressure was applied. However, it increases, as shown in the figure. Figure 5.7 shows the 1D UOT signals from the transmission and reflection geometries for the two-inclusion phantom. The X-axis is the step number showing the distance

for the 1D scans. The Y-axis is the normalised contrast difference. In the transmission geometry (red), the laser and the CCD camera were positioned in a line at the opposite sides of the phantom while in the reflection geometry, they were positioned at the same side of the phantom (blue). With both setups, the 1D scans started at the same position in the phantom. Inverse signals were observed within the mechanical inclusion region - the signal increases in refection geometry while it decreases in transmission geometry.

There were three parameters varied for these two geometries: light intensity, ultrasound power and light distribution - (1) the light intensity was much higher in transmission than in reflection; (2) a higher ultrasound power was used in the reflection geometry to obtain a satisfactory signal-to-noise ratio; (3) light formed a 'banana shape' in reflection geometry while it is a 'cone shape' in transmission geometry. In the following, I investigated these three differences.

Light distribution

The hypothesis is that the UOT signal would alter its trend by focusing US at different parts of the 'banana shape' if the light distribution is the reason for the inversed signal.

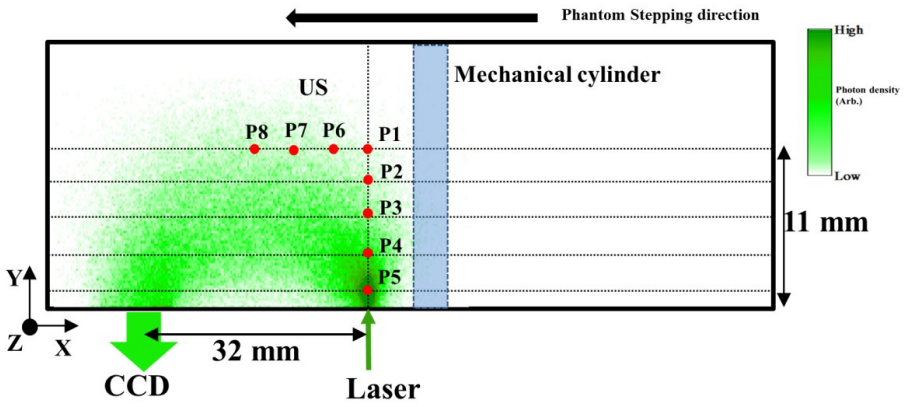

Figure 5.8 Top view of setup and experimental design

Figure 5.8 illustrates the experimental design. The optical configuration remained the same while the ultrasound focus was moved around within the light volume. The phantom used was a heterogeneous phantom where a stiffer cylinder was buried and positioned in parallel with the laser axis. In the figure, the blue shaded region is the mechanical cylinder. The diameter of the mechanical cylinder is 6 mm and its length is 22 mm. P1 – P7 are different ultrasound focus positions: P1 – P5 are in a line with the laser axis by 2 mm intervals and P6, P7 and P8 are separated along the X-axis by 5 mm intervals. By moving the phantom from the right to the left while keeping the whole configuration fixed, the scan was completed when the ultrasound focus had stepped across the cylinder. Figure 5.9 shows the 1D scan results for each ultrasound position. The standard deviations were calculated by repeating the measurements 5 times at each position. Based on these figures, the shapes of the signals within the inclusion may vary, but the increasing trend of the contrast difference within the mechanical inclusion is unchanged. This suggests that the geometry of light distribution is not the essential reason for the signal inversion.

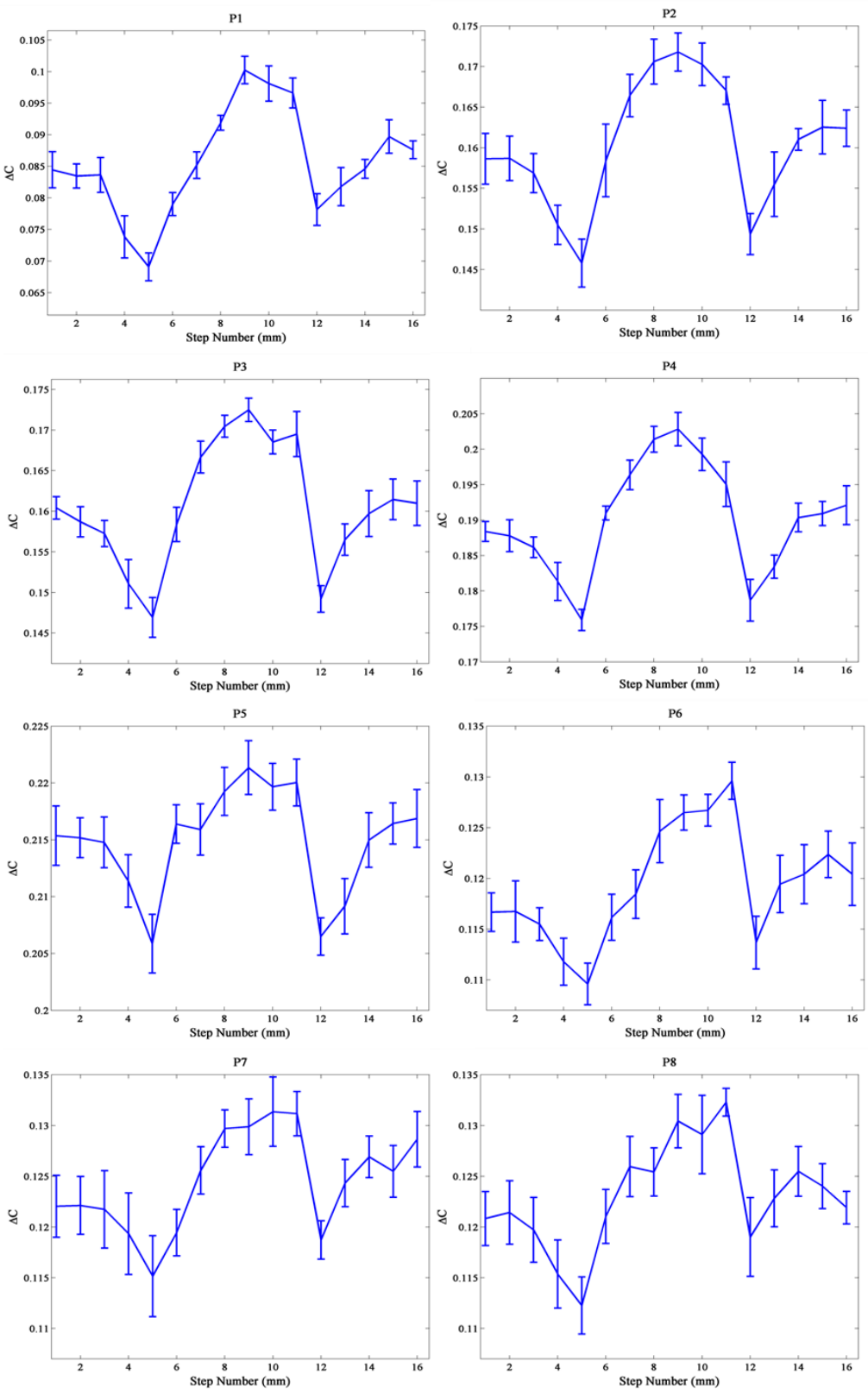

Figure 5. 9 UOT signals for each ultrasound position illustrated in Figure 5.8. The y-axis is the normalised contrast difference and the x-axis is the step number indicating the position of the ultrasound focus relative to the cylinder.

Light intensity and ultrasound power

Further experiments were made to investigate the influence of the ultrasound power and light intensity. Due to the low light intensity in the reflection geometry mode (low SNR at low US pressures, light intensity is hard to modify), the experiments were carried out with the transmission geometry. In a first experiment, the UOT signal was acquired at two different peak-negative pressures (4.4 MPa and 5.6 MPa) while the light intensity was fixed, and in a second experiment the light intensity was decreased and the ultrasound pressures were held the same as in the first experiment. Two homogenous phantoms with different stiffnesses were investigated, one of which was made of 0.8% agar powder and 4% Intralipid solution and the other was 1.2% agar powder.

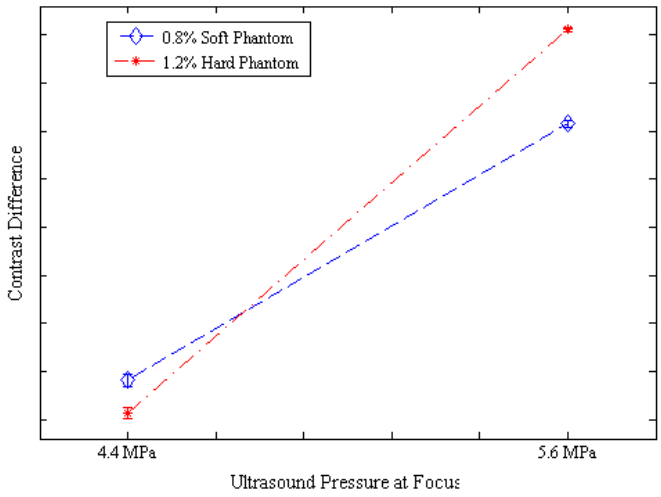

Figure 5.10 Signals at two ultrasound pressures within two homogenous phantoms with different stiffnesses (soft and hard). The blue diamond markers show the signals obtained from the soft phantom and the red star markers represent the signals from the hard phantom. Dashed lines simply link the two different pressures in order to better illustrate the inversion phenomenon.

Figure 5.10 shows the result for the first experiment. The standard deviation was achieved by repeating the measurements 20 times at each ultrasound pressure. In the figure, the signals increase with ultrasound pressure while the difference between the

two phantoms changes sign - the signal is higher at low pressure but lower at high pressure when comparing the soft phantom with the hard phantom. One hypothesis for the inverted signals is that the photon modulation saturates, and thus contributes little to the signal regardless of the large phase change (phase change > 2π). In the soft phantom, the photon modulation saturates at lower ultrasound pressures because of the larger relative displacement of the optical scatterers than in the hard phantom.

Figure 5.11 shows a comparison of the first and second experiments, in the latter of which the light intensity was different. As shown, the trend of the contrast difference change is similar for the two experiments but the intersection pressure where the same ultrasound pressure results in the same signal decreases within lower light intensity.

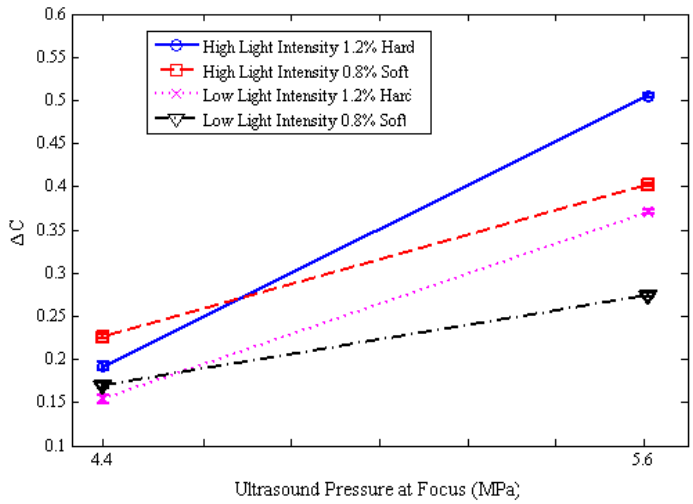

Figure 5. 11 contrast difference changes with pressure in soft and hard phantom under different light intensities in transmission mode.

To conclude, both ultrasound pressure and light intensity affect the signals. Given the low light intensity and higher pressure used in previous experiments, I think the reason for the inversed signal could be saturation of the optical modulation (> 2π) at the low light intensity in the reflection geometry. However, this needs to be further investigated and there could be other factors also affecting the result.

5.4 Discussion

Only a simplified model of shear wave propagation is used in this study, while neglecting the reflection and possible interference of shear waves from multiple reflections at mechanical inclusion boundary, or the phantom boundary. This might add more distortions to the $\Delta C(t)$ curve and needs to be further studied.

Table 5.1 shows a comparison between the optical measurement and mechanical test. As mentioned in the previous chapter, repeated tests are required to further validate my method. In addition, the two experiments were conducted at different rooms in different days with different phantoms. Although the phantoms were made following the same recipes, variation is still exciting. It is desirable to test the same phantoms with both of the methods and preferably in the same room within a short gap time, such that the errors due to the temperature change, moisture change and mechanical property variation could be minimised.

In Figure 5.6, the ratio of the standard deviation and the UOT signal is larger than it in Figure 5.5. The decreased signal-to-noise ratio is because of the reduced ultrasound pressure. The increased standard deviations of the stiffness measurement in Figure 5.6 also result from the decreased ultrasound pressure. In Figure 5.6, the UOT imaged optical absorber has a larger contrast with respect to the background and the mechanical inclusion than it in Figure 5.5. This could be caused by the variation of the added black ink, which influences the absorption coefficient of inclusion and thus the signal amplitude.

In Figure 5.5 and 5.6, UOT signals neighbouring the optical inclusions do not stay on the baseline values. This is likely caused by the absorption of the scattered light by the optical inclusion, i.e. some photons were scattered into the optical inclusion and were

absorbed even though the ultrasound focus was outside the inclusion (e.g. scan step 35 and 45 in Fig. 4). As a result, the UOT signal decreases due to the decrease of light intensity. This effect may be reduced by increasing the light intensity so that the decrease of detected photons has a reduced influence on the UOT signal. In addition, the asymmetry in the UOT base line before and after the inclusions could be related with the uneven thickness of the phantom and the reflection detection of the CCD, which may change the light environment (e.g. the intensity and geometry) and thus the UOT baseline before and after the inclusion.

For future in vivo applications using this dual mode imaging system, a number of further improvements can be made. First of all, both the system setup - including the separation and angle between the CCD and laser - and the measurement parameters - including the CCD exposure time and the length of the ultrasound burst - need to be optimised in order to improve the signal-to-noise ratio for clinical applications, e.g. in this study, a measurement geometry of 180 degree back reflection was used. Considering future in vivo applications where the skin surface may be curved, a reflection geometry with an angle less than 180 degrees would be more appropriate, and this could significantly reduce unmodulated optical background and improve the SNR. Secondly, the scan time could be reduced significantly by replacing the single element transducer used in this study with a multi-element transducer with electronic focusing, and using a higher speed CCD camera for tracking the shear wave propagation. The use of an ultrasound system with a multi-element transducer would also offer ultrasound B-mode images that are registered naturally to the UOT and elasticity images. Thirdly, the green laser used in current study should be replaced by a near-infrared laser for a lower optical attenuation and thus a better penetration depth

in biological tissues. Fourthly, speckle decorrelation needs to be investigated because it could lead to a noisy signal, e.g. it would be interesting to evaluate the influence of the speckle decorrelation on UOT and SW-LASCA measurements with a flow phantom. Fifthly, the resolution of the UOT measurement was estimated according to [5] which stated the resolution of an ARF-UOT is comparable with the ultrasound beam waist. With a hydrophone, we measured the ultrasound beam waist of our ultrasound transducer to be about 1 mm. It would be useful to evaluate the resolution of the system by scanning a point scatter inclusion in phantoms in the future. Figure 5.12 shows a possible geometry of the system that is clinically useful. The holder could be bent or extended so the distance between the camera and light beam can be modified. The tips of the holder could also be adjusted so the angle between camera and light beam can be changed. The transducer could be aligned with laser beam as shown in the figure. It also could be connected to an extra tip of holder so that the ultrasound can be focused freely in the 'banana shape' depending on applications. There may also be a layer of hydrogel phantom attached to the device to reduce the attenuation of ultrasound at the air-tissue interface.

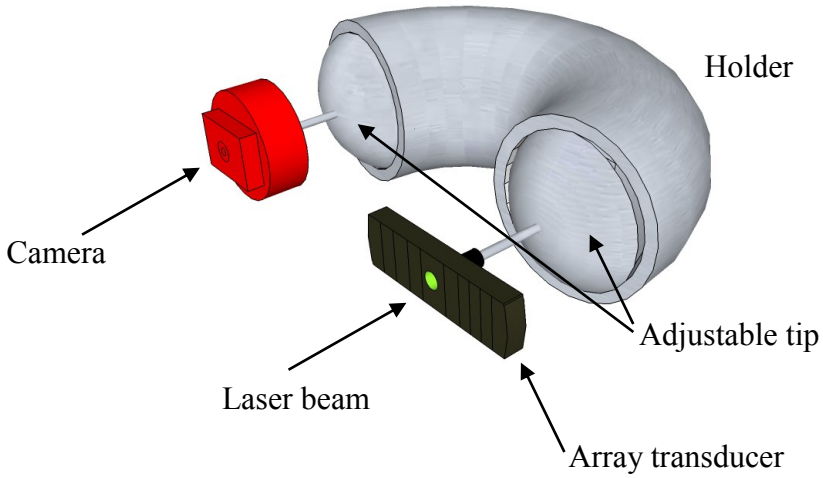

Figure 5. 12 A possible geometry of reflection detection system.

There are a few aspects, such as the optimisation of the system and the unexpected UOT signal trend, could be explored for the dual mode system. However, due to the time limit, I stopped the work and it would be interesting to continue this study in the future. In addition, the content of Chapter 6 was done before this study. The thesis was arranged in a way of increased scientific complexity.

5.5 Summary

In this chapter, by combining SW-LASCA with UOT, I developed a dual-UOT system that quantitatively measures the elasticity and qualitatively provides optical absorption information at cm depths within tissue mimicking phantoms. The ability to measure both tissue elasticity and optical properties using the same hardware offers a significant advantage over existing techniques in, e.g. imaging of cancer. The dual system was built in the reflection mode where the laser and the CCD camera were positioned on the same side of the samples. Due to the high degree of scattering of light in biological tissues, it may not be possible to take measurements in a transmission geometry and detection in reflection mode offers a more practical solution in such cases.

References

1. Wang, L., S.L. Jacques, and L. Zheng, *MCML—Monte Carlo modeling of light transport in multi-layered tissues*. Computer Methods and Programs in Biomedicine, 1995. **47**(2): p. 131-146.

2. van Staveren, H.J., et al., *Light scattering in Intralipid-10% in the wavelength range of 400-1100 nm*. Applied Optics, 1991. **30**(31): p. 4507-4514.

3. Kollmann, C., *Diagnostic Ultrasound Imaging: Inside Out (Second Edition)*. Ultrasound in Medicine and Biology. **41**(2): p. 622.

4. Cheng, Y., et al., *Shear Wave Elasticity Imaging Based on Acoustic Radiation Force and Optical Detection*. Ultrasound in Medicine & Biology, 2012. **38**(9): p. 1637-1645.

5. Zemp, R.J., C. Kim, and L.V. Wang, *Ultrasound-modulated optical tomography with intense acoustic bursts.* Appl. Opt., 2007. **46**(10): p. 1615-1623.

Chapter 6

Viscosity measurement with shear wave laser speckle contrast analysis

I report two studies on the feasibility of viscosity measurement with shear wave laser speckle contrast analysis (SW-LASCA) in the chapter. The first study shows both the simulation and experimental results on the detection of continuous shear waves generated by the amplitude modulated ultrasound (AM US). The distortions of the detected shear wave signals were observed and the possible reasons explored and discussed. In the second study, by measuring the attenuation of shear waves at different frequencies, I propose a method to quantify the viscosity of tissue mimicking phantoms with SW-LASCA. The derived viscosity values measured had a maximum standard deviation of 9%, and these were consistent with the independent measurements reported in a previous study using a non-optical method.

6.1 Introduction

As mentioned in Chapter 2, tissue viscosity may have significant effects on the tissue response [1, 2]. Tissue viscosity can be evaluated by measuring shear wave dispersion, e.g. measuring shear wave attenuation or velocity at various shear wave frequencies and the viscoelasticity can be obtained from the Voigt model. In a previous chapter, I proposed an optical method to track transient shear waves at ~cm depths within tissue mimicking phantoms by shear wave laser speckle contrast analysis (SW-LASCA). Based on a time-of-flight method, local shear wave speed was calculated by finding the time shift of a time-resolved contrast difference signal due to the transient shear waves generated at two locations separated by a known distance. In

this chapter, with the same set up, I study the feasibility of measuring the dispersion of shear waves. Firstly, the methods and principles are described, including the amplitude modulated ultrasound (AM US) to generate mono-frequency shear waves, the SW-LASCA system to track the shear wave propagation and the Voigt model to derive the viscosity. Then, two studies and their results are presented. Finally, the chapter is summarised.

6.2 Method

6.2.1 Brief introduction to SW-LASCA

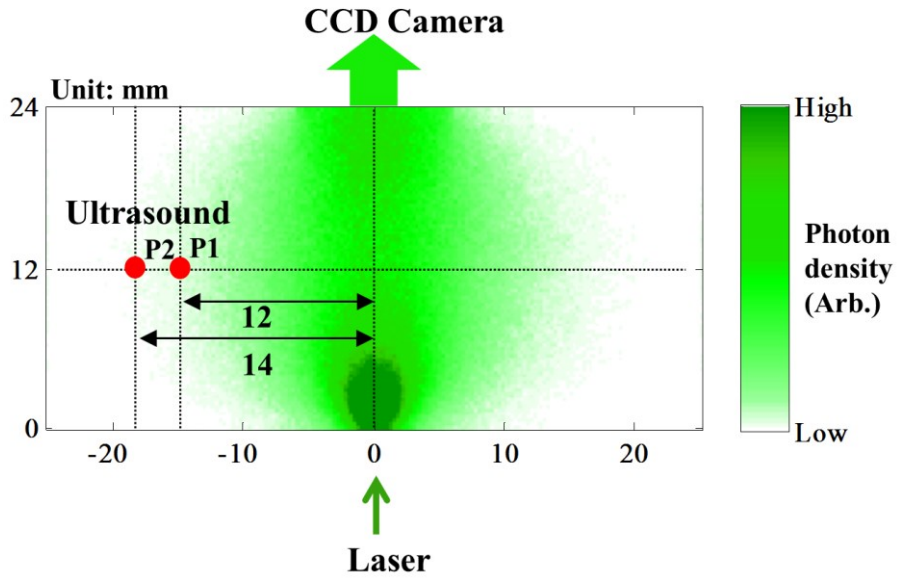

Figure 6.1 Top view of experimental setup. The Laser and CCD camera are positioned at opposite sides of the rectangular phantom. The ultrasound propagates perpendicularly to the laser axis and is positioned 12 mm or 14 mm away from it. The green region is the photon density simulated by the Monte Carlo method [3] and the phantom properties are estimated based on [4].

The method of SW-LASCA was described in previous chapters and a brief summary is provided here. In SW-LASCA, shear waves introduce disturbances in an optical turbid medium and the time-resolved speckle contrast difference ($\Delta C(t)$) is calculated to reveal the shear wave propagation.

A tissue mimicking phantom was fixed in a Perspex tank (the rectangle in Figure 6.1) and illuminated by a 532 nm laser. The transmitted laser speckle patterns were recorded on a CCD camera positioned in line with the laser. Shear waves were generated by a focused ultrasound transducer tens of millimetres away (12 mm or 14 mm in Figure 6.1) from the optical axis. The time-resolved contrast difference signal was produced by recording CCD speckle images with different time delays after the ultrasound wave has been launched.

6.2.2 Voigt model for viscosity measurement

In a viscoelastic medium such as biological tissue, shear wave velocity and attenuation may change at different frequencies. This phenomenon is defined as shear wave dispersion. The Voigt model [3] may be used to describe the shear wave dispersion as below,

$$c_s(\omega) = \sqrt{\frac{2(\mu_1^2+\omega^2\mu_2^2)}{\rho(\mu_1+\sqrt{\mu_1^2+\omega^2\mu_2^2})}} \quad \textbf{(6-1)}$$

$$\alpha_s(\omega) = \sqrt{\frac{\rho\omega^2(\sqrt{\mu_1^2+\omega^2\mu_2^2}-\mu_1)}{2(\mu_1^2+\omega^2\mu_2^2)}} \quad \textbf{(6-2)}$$

For a homogeneous Voigt medium, the shear wave propagation speed c_s and attenuation α_s depend on the frequency of the shear wave ω. μ_1, μ_2 and ρ are the shear elasticity, shear viscosity and medium density respectively. Compared with other models, such as the Maxwell model, the Voigt model is shown to be a better model for describing shear wave dispersion in soft tissue [4]. Since the density ρ of soft tissue varies little and could be assumed to be 1000 kg/m^3, the shear elasticity and shear viscosity can be inversely solved by measuring either the shear wave speed c or

attenuation coefficient α versus frequency ω.

6.2.3 Amplitude modulated ultrasound and shear waves

In previous chapters, shear waves were generated by short ultrasound bursts (1 ms or 2 ms), and their frequency spectra were broad. To find the shear wave dispersion, the shear wave frequency ω and thus a long shear wave chain at a certain frequency is required. One way to generate continuous shear wave propagation at a certain fixed frequency in tissue is to generate an oscillatory acoustic radiation force (ARF), and this can be done in several ways, such as using confocal or X-focal transducers where two transducers are intersected to generate the ARF at their beat frequency [5]. In this chapter, I use an alternative method that generates the oscillatory ARF by a long amplitude modulated ultrasound (AM US) burst from a focused transducer.

Amplitude modulated ultrasound

Consider an ultrasound pressure field $p_c(t)$, as:

$$\boldsymbol{p_c(t) = P_c \cos(\omega_{US} t)}. \quad \textbf{(6-3)}$$

In the expression, $p_c(t)$ represents the instantaneous value of ultrasound wave at a specific time t, P_c represents the amplitude of the ultrasound wave and ω_{US} is the angular frequency of the ultrasound wave.

The modulating signal can be expressed with a similar formula,

$$\boldsymbol{p_m(t) = P_m \cos(\omega_m t + \varphi)}, \quad \textbf{(6-4)}$$

where $p_m(t)$, P_m and ω_m represents the instantaneous value of the modulating wave at a specific time t, the amplitude and the frequency of the modulating wave respectively. φ is the phase shift of the modulating wave relative to the ultrasound wave.

Therefore, an AM ultrasound pressure field $p(t)$ can be expressed as:

$$\boldsymbol{p(t) = [P_c + P_m\ \cos(\omega_m t + \varphi)\ ]\cos(\omega_{US} t)},\qquad \textbf{(6-5)}$$

where the amplitude of the ultrasound wave is periodically modulated by the modulating wave $p_m(t)$. Since the amplitudes for both waves were the same and the phase difference $\boldsymbol{\varphi}$ was equal to π in the experiment, equation 6-5 can be rewritten as

$$\boldsymbol{p(t) = P_c[1 + \cos(\omega_m t + \pi)\ ]\cos(\omega_{US} t)},\qquad \textbf{(6-6)}$$

Figure 6.2 shows an example of an AM signal where the amplitude of the blue ultrasound signal is modulated by a signal (red dash line) with a lower frequency.

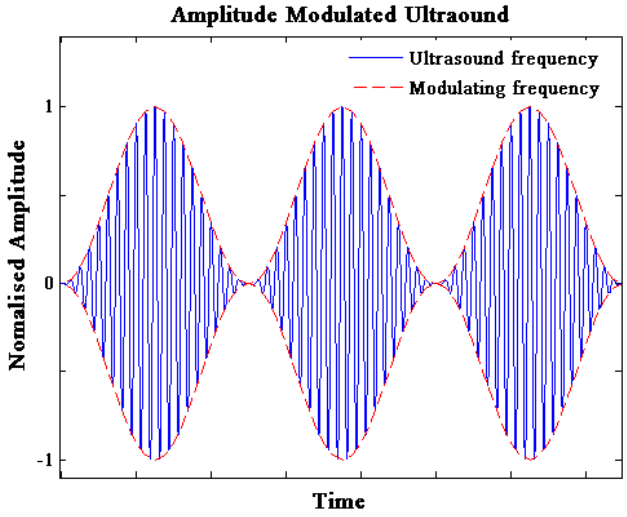

Figure 6.2 Example of amplitude modulated ultrasound signal. The blue curve shows the ultrasound wave which is amplitude modulated by the modulating frequency, indicated the red curve. The frequency of the modulating wave is 200 Hz which much lower than the 5 MHz ultrasound frequency.

Acoustic radiation force and shear wave

The ARF is generated by a transfer of the momentum from the ultrasound to the tissue. In soft tissue, the magnitude of force (F) can be approximated by

$$\boldsymbol{F = \frac{2\alpha_{US}\langle I\rangle_T}{c_{US}}}.\qquad \textbf{(6-7)}$$

where α_{US} is the acoustic absorption coefficient of the medium, c_{US} represents the speed of sound in the medium, I is the intensity of the sound and $\langle\ \ \rangle_T$ means the average within time T. The modulating frequency was much lower than the ultrasound

frequency and thus the intensity I, which is proportional to $p(t)\text{^}2$, has a slow variation in time. To calculate the averaged intensity, T was chosen to be longer than the ultrasound period but much shorter than the modulation period, which is $2\pi/\omega_{US} \ll T \ll 2\pi/\omega_m$. Under this condition, F can be given by

$$\boldsymbol{F = \frac{2\alpha_{US}\langle I\rangle_T}{c_{US}} = \frac{2\alpha_{US}}{c_{US}T}\int_{t-\frac{T}{2}}^{t+\frac{T}{2}} p^2(\tau)d\tau}$$

$$\boldsymbol{= \frac{2\alpha_{US}}{c_{US}T}\int_{t-\frac{T}{2}}^{t+\frac{T}{2}} {P_c}^2[1+\cos(\omega_m\tau+\pi)]^2\frac{1}{2}(1+\cos 2\omega_{US}\tau)d\tau}$$

$$\boldsymbol{\approx \frac{\alpha_{US}{P_c}^2}{c_{US}}[1+\cos(\omega_m t+\pi)]^2} \qquad \textbf{(6-8)}$$

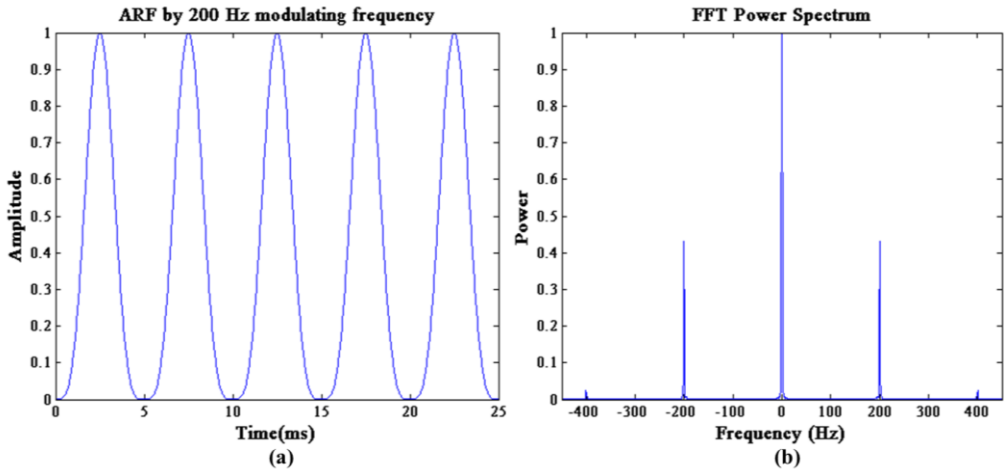

Figure 6.3 (a) Normalised ARF amplitude versus time for the amplitude modulated ultrasound at 200 Hz. (b) Power spectrum of the signal in (a). Harmonics can be seen at 400 Hz but with a very low power.

Equation 6-8 shows that the oscillation of the ARF is related to the modulating frequency ω_m rather than the ultrasound frequency. Figure 6.3(a) plots the normalised ARF based on Equation 6-8 where the modulating frequency was 200 Hz. As seen, the ARF periodically oscillates with time. Figure 6.3(b) shows the Fourier transform of the ARF. ARF harmonics can be seen at 400 Hz, but their power is much smaller

than the fundamental power. Therefore, I assume the generated shear waves oscillated only at the fundamental frequency.

6.3 Detection of continuous shear wave with SW-LASCA

In this section, I study the detection of continuous shear waves with both experiment and simulation. In the experiment, it was not feasible to generate continuous shear waves, which would destroy the transducer due to the high energy used. Therefore, shear waves with multiple cycles (> 10 cycles) were generated as a compromise and herein called 'continuous shear wave'. The simulation tool was developed by Li et al and proven in experiments to detect short shear wave bursts (1 ms or 2 ms) [6]. I applied this tool to study the detection of continuous shear waves.

6.3.1 Experimental system for continuous shear wave

The experimental setup is shown in Figure 6.1 where the laser and CCD are perpendicular to the ultrasound transducer and placed in a transmission geometry, and the ultrasound and shear wave are generated several millimetres away from the optical axis (DAO). The setup is the same as that used for the elasticity measurements in Chapter 4.

In order to generate a continuous shear wave, the control system was modified and two function generators were used. One function generator was to generate the 5 MHz ultrasound frequency and another was used for the amplitude modulation. The modulating frequency was usually within 1 kHz and the result part (section 6.3.4) showed the signals for 200 Hz and 400 Hz modulating frequencies at 12 mm and 14 mm DAO as examples. Other parts of the control system remained the same as before.

6.3.2 Simulation of SW-LASCA for continuous shear waves

Figure 6.4 illustrates a simple flowchart for the simulation. Firstly, the displacement field of shear wave and photon trajectories were simulated. Secondly, depending on the displacement field, the time-resolved phase change of each photon along its orbit was calculated. Finally, the time-resolved contrast signal was obtained based on the phase change of thousands of photons. The background contrast was assumed to be 1 and the final signal was obtained by $\Delta C(t) = 1 - C(t)$.

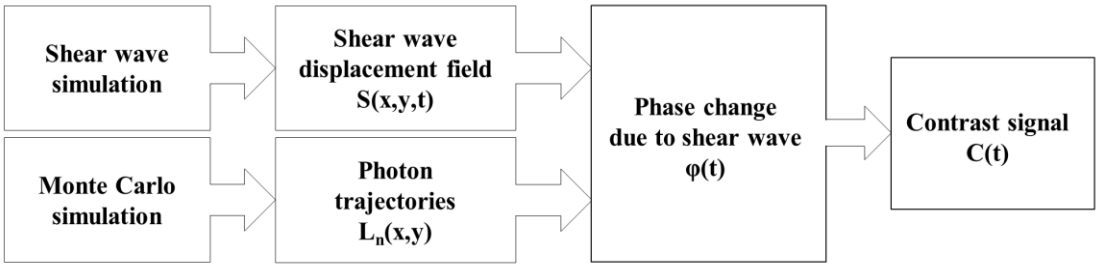

Figure 6.4 A simple flowchart for the simulation of SW-LASCA

Shear wave field

In Chapter 2, the shear wave displacement field generated by an impulse (called P-field below) was calculated based on [7]. In order to calculate the shear wave displacement field generated by an oscillated ARF (O-field), weighted convolution was applied to the P-field in both time and space. In the space domain, the P-field was convolved within the focal region of the transducer which was about 1 mm in the lateral and 10 mm in the vertical direction. The convolution was weighted by a mask generated based on the hydrophone measurement of the focal region of the transducer shown in Figure 6.5. Figure 6.5(a) is the lateral pressure profile of transducer (G(x)) and (b) is the profile along vertical direction (G(y)). The dots in the figures are the normalised hydrophone pressure values and the solid lines are the corresponding fittings with the smooth spline method in Matlab. The weights in the mask were

calculated by multiplying G(x) and G(y) at each position within the focal region. In the time domain, the convolved P-field was weighted based on Equation 6-8.

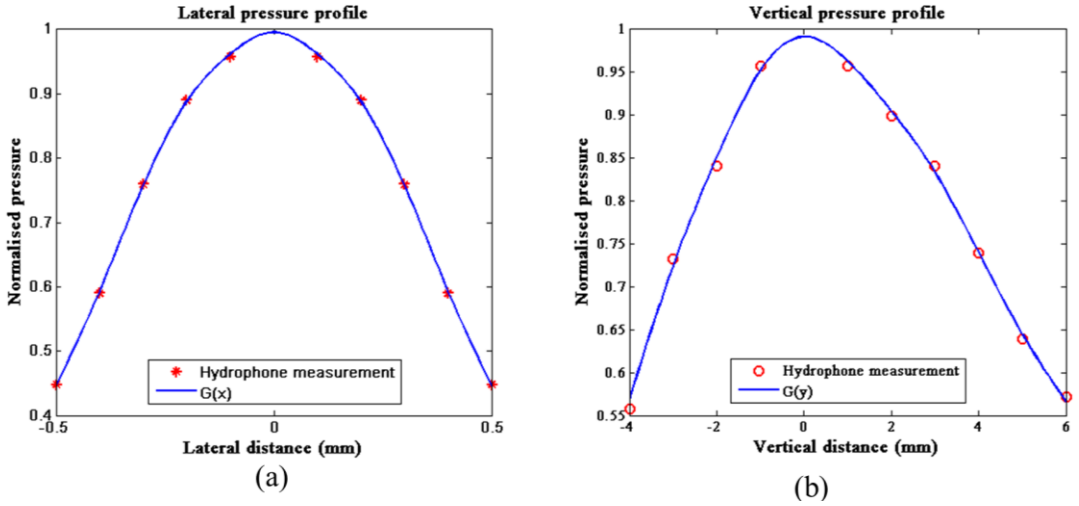

Figure 6.5 Hydrophone measurements for the lateral (G(x)) and vertical (G(y)) pressure within the transducer focal region. In both figures, the x-axis is the position of the hydrophone relative to the ultrasound central point, and the y-axis is the normalised pressure received by the hydrophone.

As an example, the convolution parameters in Table 6.1 were used to generate an O-field. In the time domain, the period of shear wave was 12.5 ms and the modulating frequency was 400 Hz. The amplitude of the ARF was normalised and thus $(aP^2)/c$ was equal to 1 in Equation 6-8. In the space, G(x) and G(y) were used to calculate the weights for the mask within the focal region (1 mm width and 10 mm length).

Table 6 - 1 Parameters to generate a continuous shear wave field

Convolution parameter (O-field)			
Time domain		*Space domain*	
Modulating frequency	400 Hz	Mask weight	G(x) × G(y)
Modulating length	12.5 ms	Mask width	1 mm
Amplitude of ARF	Normalised	Mask length	10 mm

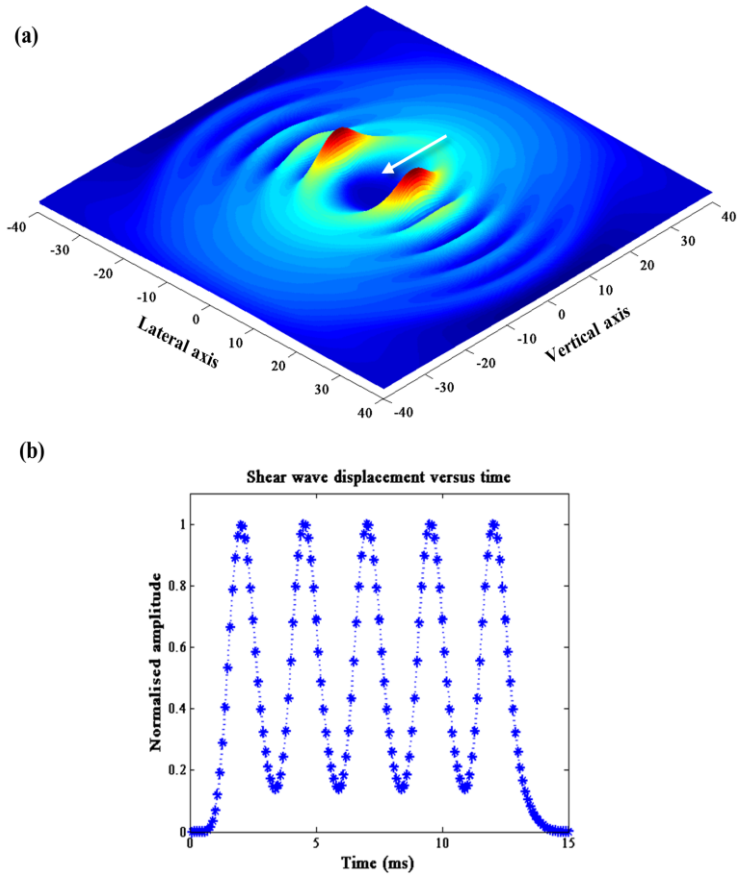

Figure 6.6 (a) Simulated shear wave O-field at 15 ms for a 400 Hz modulating frequency. (b) Simulated displacement versus time for a point 14 mm away from the focus.

Figure 6.6(a) is the shear wave field at 15 ms. The vertical and lateral axe are the shear wave propagation distances and the colour depicts the shear wave displacement. The white arrow indicates the ARF direction, which is along the vertical-axis. Five shear wave wavefronts can be observed in Figure 6.6(a) though the wavefronts far from the originating region have much smaller amplitudes due to the attenuation of the shear waves. Figure 6.6(b) plots the time-resolved displacement at a position 14 mm away from the focus in time. There are 5 cycles with 2.5 ms period at the position within 15 ms, suggesting the frequency of the wave is 400 Hz, as expected.

Monte Carlo simulation

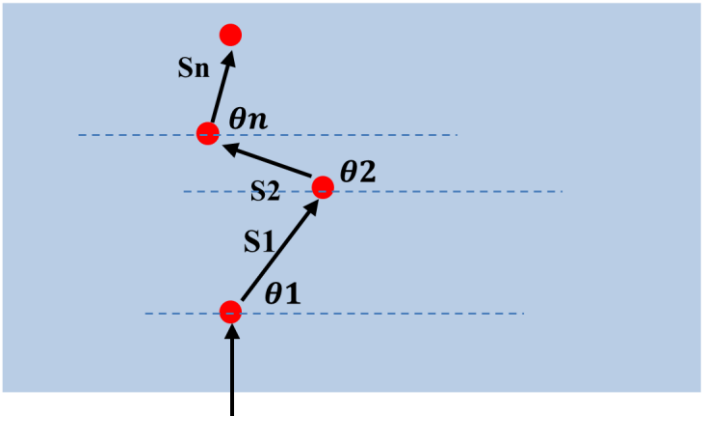

Figure 6.7 Schematic of a single photon's trajectory in a semi-infinite medium

A thorough discussion of the Monte Carlo simulation for the photon transport can be found in [8]. Briefly, photon trajectories are expressed by a sequence of scattering events whose positions are determined by the step sizes of photon movements between the interaction sites and the angles of the deflection at a certain scatterer. Figure 6.7 is a schematic for modelling a single photon's transport in a semi-infinite medium with the Monte Carlo simulation. Initially a single photon packet with unit energy is launched into the tissue. Due to the reflection at the tissue surface, a certain amount of photon energy is lost according to the reflection coefficient. Then, the step size **S** of the photon movement is determined by

$$\boldsymbol{s} = \frac{-\ln(\varepsilon)}{(\mu_a + \mu_s)}, \tag{6-9}$$

where ε is a random number that is uniformly distributed over (0, 1), and μ_a, μ_s are the tissue absorption and scattering coefficients respectively. The scattering angle θ is determined by the scattering anisotropy g as

$$\cos\theta = \begin{cases} \frac{1}{2g}\left[1 + g^2 - \left(\frac{1-g^2}{1-g+2g\varepsilon}\right)^2\right] & \text{if } g \neq 0 \\ 1 - 2\varepsilon & \text{if } g = 0 \end{cases} \tag{6-10}$$

And the polar angle φ is assumed to be uniformly distributed between 0 and 2π and equal to $2\pi\varepsilon$. Subsequently, the photon packet is moved to a new position according to these three parameters (s, θ and $\boldsymbol{\varphi}$). However, before moving the photon packet, the simulation will judge if the movement will intersect the boundary of the medium. If it hits the boundary, the simulation will calculate if the photon escapes from the medium or is internally reflected. Once it escapes, the photon trajectory terminates. Otherwise, it will reflect from the boundary and move to a new position within the medium. After each movement, the absorbed energy will be calculated according to the absorption coefficient and a survival roulette will run if the energy of the photon packet is below a set threshold. A trajectory finishes either when a photon escapes from a boundary or is absorbed in the medium. This process is repeated for millions of photons to obtain good statistics for a reliable light density distribution.

Contrast calculation

A stochastic explanation of CCD speckle analysis for ultrasound modulated optical tomography (UOT) was provided by [9]. In the simulation, it was extended to shear wave modulation.

The CCD speckle contrast is defined by $C = \sigma/\bar{I}$, where σ and $\bar{I}$ are the standard deviation and the mean of the CCD pixel intensities. With the assumption of spatial ergodicity, the standard deviation and mean intensity can be expressed as

$$\boldsymbol{\sigma} = \sqrt{\langle [\boldsymbol{E(t)E^*(t+\tau)}]^2 \rangle_{t,\tau,\varepsilon}}, \quad \textbf{(6-11)}$$

$$\boldsymbol{\bar{I}} = \langle \boldsymbol{E(t)E^*(t+\tau)} \rangle_{t,\varepsilon}\big|_{(\tau=0)}, \quad \textbf{(6-12)}$$

Where E is the complex optical field at a CCD pixel, E^* is the conjugate of E. The Symbol < > denotes averaging over t, τ, ε where t is the time, τ is the time derivative and ε represents a single realization of the optical scatter distribution. In a turbid

medium, $\boldsymbol{E(t)}$ could be considered as a summation of many random paths due to the random scattering of photons. Then $\langle \boldsymbol{E(t)E^*(t+\tau)} \rangle_{\boldsymbol{t}}$ can be written as

$$\langle \boldsymbol{E(t)E^*(t+\tau)} \rangle_{\boldsymbol{t}} \;=\; \sum_{\boldsymbol{i=1}}^{\boldsymbol{N}} \sum_{\boldsymbol{j=1}}^{\boldsymbol{N}} \langle \boldsymbol{E_i(t)E_j^*(t+\tau)} \rangle_{\boldsymbol{t}}, \qquad \textbf{(6-13)}$$

where i , j means the ith and jth paths of the many random paths and N is the total numbers of these paths. Assuming a week scattering in tissue, the phase of a photon in one scattering path is independent from another. Therefore, the phase differences between different paths ($i \neq j$) are uniformly distributed through 0 and 2π, leading to a cancellation of the cross terms in $\langle \boldsymbol{E(t)E^*(t+\tau)} \rangle_{\boldsymbol{t}}$ which can be then simplified as

$$\langle \boldsymbol{E(t)E^*(t+\tau)} \rangle_{\boldsymbol{t}} \;=\; \sum_{\boldsymbol{i=1}}^{\boldsymbol{N}} \langle \boldsymbol{E_i(t)E_i^*(t+\tau)} \rangle_{\boldsymbol{t}}$$

$$= \frac{\boldsymbol{1}}{\boldsymbol{N}} \sum_{\boldsymbol{i=1}}^{\boldsymbol{N}} \langle \boldsymbol{exp}\left(-\boldsymbol{i}\left(\sum_{\boldsymbol{k=1}}^{\boldsymbol{N'}} \Delta \boldsymbol{\varphi_{ik}(t,\tau)}\right)\right) \rangle_{\boldsymbol{t}}, \qquad \textbf{(6-14)}$$

where $\mathbf{N'}$ is the total number of scattering events in ith path and $\Delta \boldsymbol{\varphi_{ik}(t,\tau)}$ is the optical phase change at the kth scattering event in the ith path, which can be calculated by the path change between $(k-1)$th and the kth scatterers during time t to (t + τ) as

$$\Delta \boldsymbol{\varphi_{ik}(t,\tau)} \;=\; -\boldsymbol{nK}[\boldsymbol{\Delta r_{ik}(t+\tau)} \;-\; \boldsymbol{\Delta r_{ik}(t)}], \qquad \textbf{(6-15)}$$

where n is the refractive index of medium, K is the optical wave number and $\Delta r_{ik}\,(t)$ and $\Delta r_{ik}(t+\tau)$ are the paths between $(k-1)$th and the kth scatterers at times t and (t+ τ) respectively.

$$\boldsymbol{\Delta r_{ik}(t)} \;=\; (\boldsymbol{r_{ik}(t)} \;-\; (\boldsymbol{r_{i(k-1)}(t)}\,);$$

$$\boldsymbol{\Delta r_{ik}(t+\tau)} \;=\; (\boldsymbol{r_{ik}(t+\tau)} \;-\; (\boldsymbol{r_{i(k-1)}(t+\tau)}\,); \qquad \textbf{(6-16)}$$

The equations above showed the calculation of $\mathbf{\Delta r_{ik}\,(t)}$ and $\mathbf{\Delta r_{ik}(t+\tau)}$, where $\mathbf{r_{ik}}$ and $\mathbf{r_{i(k-1)}}$ are the positions of the kth and the (k – 1)th scatterers. When there is no

modulation and the scatterers are static, according to Equations 6-17 and 6-18, $\Delta\boldsymbol{\varphi_{ik}}(\mathbf{t},\boldsymbol{\tau})$ is equal to zero. When the shear wave modulation is considered, the optical path at time t and (t+ $\boldsymbol{\tau}$) between the (k – 1)th and the kth scatterers are affected by the shear wave displacement $\mathbf{S_{ik}}$ as

$$\boldsymbol{\Delta r_{ik}(t)} = (\boldsymbol{r_{ik}(t)} + \boldsymbol{S_{ik}(t)}) - (\boldsymbol{r_{i(k-1)}(t)} + \boldsymbol{S_{i(k-1)}(t)}).$$

$$\boldsymbol{\Delta r_{ik}(t+\tau)} = (\boldsymbol{r_{ik}(t+\tau)} + \boldsymbol{S_{ik}(t+\tau)}) - (\boldsymbol{r_{i(k-1)}(t+\tau)} + \boldsymbol{S_{i(k-1)}(t+\tau)}). \textbf{(6-17)}$$

As a result, $\Delta\varphi_{ik}(\boldsymbol{t},\tau)$ and thus the contrast of the CCD vary with the displacement of the shear wave. The contrast difference due to the shear wave modulation can be then calculated using the equations above and the shear wave displacement field.

For the ultrasound modulation, the variation of the refractive index of sample is with the ultrasound propagation and thus has an impact on the phase of photon. For the shear wave modulation, the contribution from the refractive index change is neglected because the slow motion of shear wave propagation and thus a little change of refractive index during the exposure time. However, in the situation where the period of shear wave is much shorter than the exposure time, neglecting the impact of refractive index could introduce bias in the calculation of contrast.

6.3.3 Experiment and simulation design

A homogenous phantom made of 0.8% agar powder and 4% Intralipid solution was used. The size of the phantom was 180 mm (length) × 80 mm (width) × 24 mm (thickness). An 80 ms amplitude modulated ultrasound (AM US) burst was excited and focused into the phantom. In a first experiment, a 200 Hz modulating frequency was used and the distance between optical axis and ultrasound focus (DAO) was 12 mm or 14 mm. The detection of the shear wave started at 40 ms after the generation of ultrasound and finished at 60 ms with 0.25 ms resolution. In a second experiment, a

400 Hz modulating frequency was used and the procedure was repeated. In the experiment, the ultrasound pressure used was 5.7 MPa at the ultrasound focus and the exposure time was 1.5 ms.

The simulation design remained the same as the experiment. The signals for 80 ms AM US bursts at 200 and 400 Hz were simulated. The input optical properties of the homogenous phantom were estimated based on [10], including the optical absorption coefficient μ_a = 0.2 cm^{-1}, the optical scattering coefficient μ_s =30 cm^{-1} and the anisotropic coefficient g=0.8. The mechanical parameters were set based on [7], including the shear wave speed $c_s = 2.5$ m/s, the bulk wave speed $c_{US} = 1500$ m/s, the shear viscosity $v_s = 0.1$ Pa.s and the bulk viscosity $v_p = 0$ Pa.s. The shear wave amplitude was set to be 30 nm at DAO = 12 mm for both the 200 and 400 Hz AM US bursts. In the experiment, a Perspex tank was used to fix the phantom. Due to the large mismatch between the phantom and the tank walls, shear waves were almost totally reflected into the phantom at its boundaries. This was considered in the simulation by adding extra shear wave sources along the directions of the reflected shear waves [6]. In this simulation, the shear wave dispersion was not considered and thus the shear wave speed and attenuation were fixed for different frequencies.

6.3.4 Results

Figure 6.8 shows the results from the experiment. Figure 6.8(a) is the signal from the 200 Hz AM US and Figure 6.8(b) is for 400 Hz. The deformation of signal could be seen for both frequencies. The signal within one period is not symmetric and there are two peaks appearing in some cycles. Moreover, the signal at 14 mm is not a simple shift of the signal at 12 mm. The deformation pattern changed at the two DAOs.

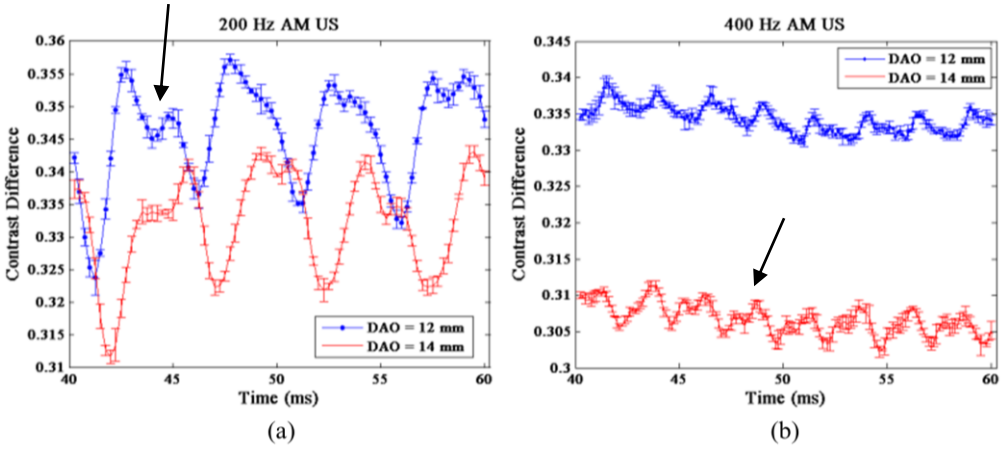

Figure 6.8 Experimental results for (a) 200 Hz AM US and (b) 400 Hz AM US. The x-axis is the time after the ultrasound was launched and the y-axis is the CCD signal. The standard deviations were calculated by repeating the experiments three times. Arrows indicate examples of the signal deformation.

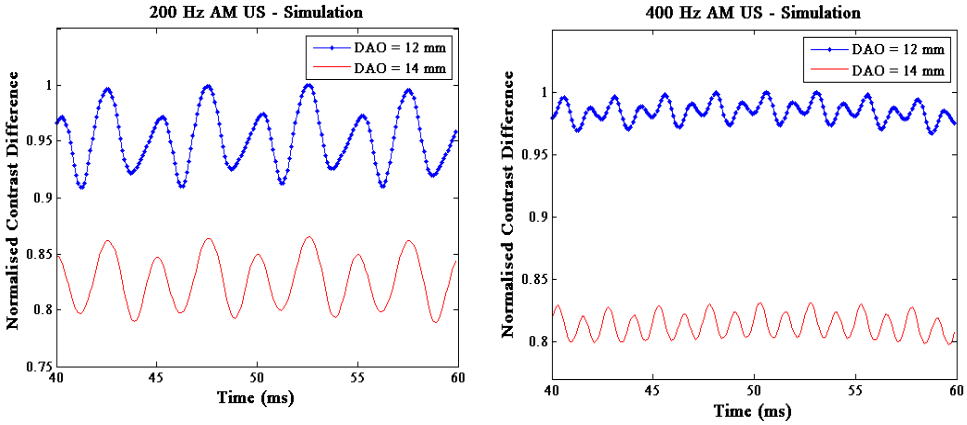

Figure 6.9 Simulation results for (a) 200 Hz AM US and (b) 400 Hz AM US. The x-axis is the time after the ultrasound was launched and the y-axis is the normalised signal.

Figure 6.9 shows the results from the simulation where Figure 6.9(a) is for a 200 Hz shear wave and (b) for 400 Hz. The simulation results confirmed the signal deformations and pattern changes at the two DAOs. Moreover, in the simulation, the shear wave speed was set as 2.5 m/s and thus the time delay between the two DAOs (2 mm) should be 0.8 ms. Nevertheless, according to the results, neither of the time differences between any two peaks or troughs is equal to 0.8 ms for either figures.

6.3.5 Discussion and Conclusion

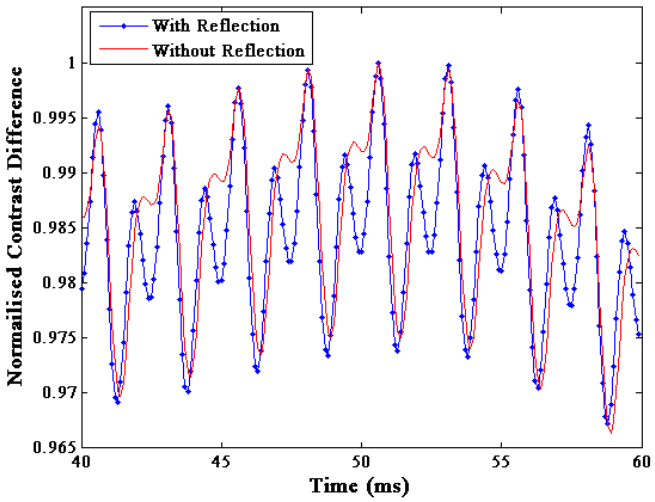

Figure 6.10 Simulation result with (blue) and without (red) consideration of shear wave reflections. The frequency of shear wave is 400 Hz and the detection distance (DAO) is 12 mm.

In the experiment and simulation, the signal at 400 Hz has a smaller amplitude of oscillation than that at 200 Hz. This is likely because the same exposure time was used for both frequencies, which averaged out the signal more for the higher frequency. In the experiments, due to the shear wave dispersion, the shear wave attenuates more at higher frequencies and thus the signal at 14 mm is much smaller than at 12 mm for the 400 Hz shear wave compared with the signals for the 200 Hz shear wave. In the simulation, the shear wave attenuation could also be observed but it was similar for the two frequencies. The difference between the results of the experiment and simulation could be due to inaccurate input parameters for the simulation, including the optical properties of the phantom which were estimated based on [10] and could deviate from the true properties of the phantom. Also the detection area of the CCD was set as 6 mm in radius in the simulation, an estimation based on the experimental setup. This could also deviate from the true detection area in the experiments.

There are several reasons that may result in distortions of the CCD signal, including reflections of the shear waves from the phantom boundaries, CCD detection and the complex 3D geometries between the illuminated volume and the shear wave field.

Due to the large mismatch between the phantom and the water tank, shear waves were almost totally reflected at the boundaries. The extra peak in some shear wave cycles may result from the superposition between the original shear waves and reflected shear waves. In order to verify this assumption, a simulation without shear wave reflections was made and the result is plotted in Figure 6.10 for the 12 mm DAO (red curve) while the blue curve is the signal when shear waves reflections were considered. Based on this result, the reflected shear waves do affect the signal but the deformation still exists.

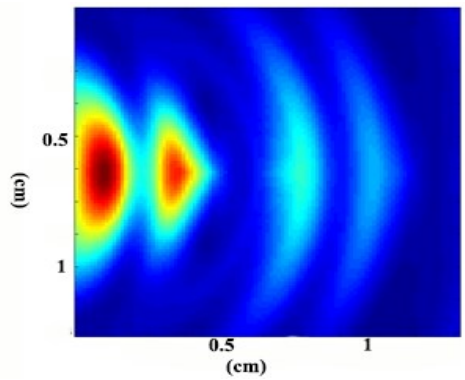

Figure 6.11 speed field of scatters for two-cycle shear waves at t = 45 mm.

Another possible reason for the extra peak may result from the CCD detection which is sensitive to the speed rather than the displacement of scatters. Figure 6.11 shows the speed field obtained by calculating the derivative of the displacement field of a 400 Hz shear wave at t = 45 ms within a 1.2 cm square. There are two cycles of shear wave (two wavefronts) in the displacement field given the 2.5 m/s shear wave speed in the simulation. After differentiation, it shows four wavefronts in the speed field,

suggesting an extra wavefront within a cycle of shear waves. Since the CCD detection could be regarded as an integration of the speed field within space and time, Figure 6.12 plots the possible CCD signal obtained by integrating the speed field within the 1.2 cm square and 1.5 ms exposure time for the DAO of 12 mm (a) and 14 mm (b). The results have similarity with the results in Figure 6.8 and 6.9. The difference could result from the 1.2 cm integration square and the properties of the phantom which may not be accurate in the experiments. Although this needs to be further investigated, the result suggests that the use of a CCD has influence on the detection of continuous shear waves.

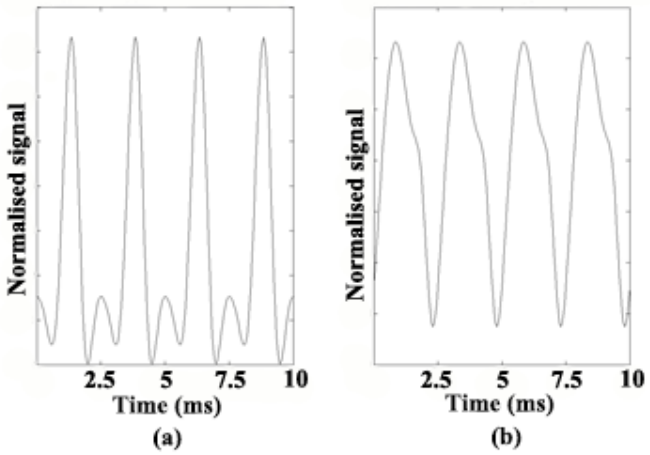

Figure 6.12 Signals for two DAOs by integrating the scatterer speed field in time and space. (a) Normalised signal when DAO was 12 mm and (b) Normalised signal with 14 mm DAO.

In addition, the pattern change at two DAOs may result from the complex 3D overlapping geometries between the shear wave field and the light volume. At different DAOs, the light and CCD were fixed while the ultrasound moved a certain distance away from the light. Due to the spreading of the shear wave, the volumes of the shear wave and thus the overlap between the light volume and the shear wave differed at the two DAOs, which may change the shapes of the signals at different

DAOs.

Since the detection of continuous shear waves is complex, there may be other factors leading to the distortions and my assumptions could be incomplete or invalid. Based on the above results and discussions, it is difficult to calculate the shear wave speed using the differential method described in Chapter 4. In order to measure the viscosity, one possible way is to use advance signal processing method, such as a statistical analysis of the data to detect the time shift. Alternatively, I propose a new method which measures the attenuation dispersion of shear wave in next section.

6.4 Viscosity measurement with SW-LASCA

In this part, Equation 6-3, which describes the relation among shear wave attenuation, shear wave frequency, tissue elasticity and viscosity, is investigated to estimate the viscosity of tissue mimicking phantoms with SW-LASCA.

6.4.1 Principle

Equation 6-3 is reproduced below. The tissue density is about 1000 kg/m^3 for phantom and viscosity could be inversely solved if the relation between shear wave attenuation and frequency could be obtained.

$$\boldsymbol{\alpha(\omega) = \sqrt{\frac{\rho\omega^2\left(\sqrt{\mu_1^2 + \omega^2\mu_2^2} - \mu_1\right)}{2(\mu_1^2 + \omega^2\mu_2^2)}}}$$

To measure the shear wave attenuation, the following relationships are deduced. Firstly, the relationship between the shear wave attenuation coefficient and amplitude is known as:

$$\boldsymbol{A_i = A_0 exp(-\alpha_f S_i)}, \qquad \textbf{(6-18)}$$

where A_i the shear wave amplitude at position i, A_0 is the initial amplitude of the

shear wave at the ultrasound focus, α_f is the attenuation coefficient of the shear wave at frequency f, and S_i is the shear wave path length between the focus and the position i. According to Eq. 6-18, the shear wave attenuation coefficient could be derived if A_i, A_0 and S_i are known.

In the experiments, the S_i, which is the distance between the laser and ultrasound axes, is known. A_0 is assumed to be linear with the magnitude of the ARF, and the ARF is proportional to the time-averaged ultrasound intensity I_0 [11]. Therefore, the relationship between shear wave initial amplitude A_0 and I_0 can be related as:

$$\boldsymbol{I_0 = KA_0,} \tag{6-19}$$

where K is an unknown constant. On the other hand, the time-averaged ultrasound intensity I_0 is proportional to the mean square of the ultrasound pressure. With a hydrophone measurement, I_0 could be further related to the input voltage of the ultrasound transducer. Figure 6.13 shows the hydrophone measurement result (red dots), where the x-axis is the ultrasound input voltage and the y-axis is the ultrasound intensity (mean square of acoustic pressure). With linear regression (blue solid line), the relationship between the time averaged ultrasound intensity and the transducer input voltage (between 300 and 600 mVpp) was found to be

$$\boldsymbol{I_0 = 0.28V - 66.42,} \tag{6-20}$$

By substituting Equation 6-19 and 6-20 into 6-18,

$$\boldsymbol{A_i = \frac{0.28V-66.42}{K}\exp(-\alpha_f S_i),} \tag{6-21}$$

In Equation 6-21, A_i and K are unknown, α_f is the averaged attenuation coefficient over S_i. To eliminate K and calculate the local shear wave attenuation coefficient, shear waves were generated at two locations, with path lengths of S_i and S_j. The ratio of the corresponding shear wave amplitudes is calculated as

$$\frac{A_i}{A_j} = \frac{0.28V_i - 66.42}{0.28V_j - 66.42} \exp(-\alpha_f(S_i - S_j)) \,. \qquad \textbf{(6-22)}$$

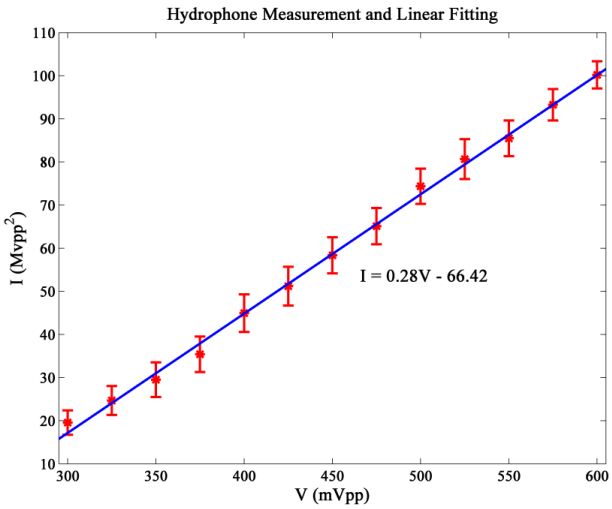

Figure 6.13 Hydrophone measurements of voltage and ultrasound intensity

To calculate the left side of Equation 6-22, I assumed that identical shear wave amplitudes at the detection position result in identical contrast differences, which means if $\Delta C_i = \Delta C_j$, then $A_i = A_j$, despite the differences in the original positions of the shear waves. Consequently, 6-22 can be rewritten as:

$$\left\{1 = \frac{0.28V_i - 66.42}{0.28V_j - 66.42} \exp(-\alpha_f(S_i - S_j))\right\}_{\Delta C_i = \Delta C_j}, \qquad \textbf{(6-23)}$$

and the shear wave attenuation coefficient α_f at frequency f can be calculated by

$$\left\{\alpha_f = \frac{\log \frac{0.28V_j - 66.42}{0.28V_i - 66.42}}{S_i - S_j}\right\}_{\Delta C_i = \Delta C_j} . \qquad \textbf{(6-24)}$$

The method to find the (V_i, V_j) pair in Equation 6-26 is described below. Figure 6.14 shows the relationship between the ultrasound input voltages $V_{i(j)}$ and the contrast difference $\Delta C_{i(j)}$ induced by the 400 Hz shear wave. P1 and P2 are the two positions where shear waves are generated (Figure 6.1). Because P2 is located 2 mm further away from the detection area than P1, the corresponding mean contrast difference

values are smaller because of shear wave attenuation. By changing the ultrasound input voltage, the mean contrast differences increase for both P1 and P2. The two curves in the figure indicate the linear regressions of the data. As indicated by the dashed black lines in the figure, for a given ΔC, V_i and V_j can be obtained from the fitted curves to calculate the shear wave attenuation coefficient α_f using Equation 6-24. By varying the shear wave frequency, α_f at several frequencies were found and the viscosities were inversely estimated with the least-squares method.

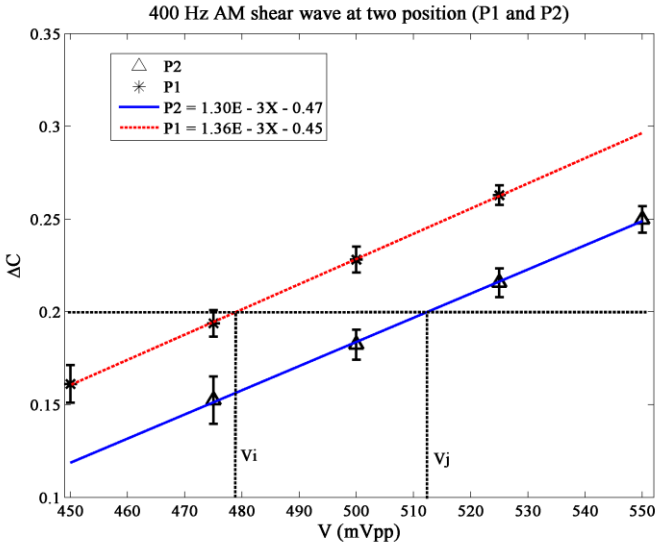

Figure 6.14 Relationship between ultrasound input voltages $V_{i(j)}$ and contrast difference $\Delta C_{i(j)}$ induced by a 400 Hz shear wave

6.4.2 Experimental design

Figure 6.15 illustrates the experimental design of a viscosity measurement. Firstly, two homogenous phantoms were made of 4% gelatine and 1% agar powder following the recipe in [2]. 4% intralipid was added to the solution to obtain a reduced optical scattering coefficient of 5 cm^{-1} [12]. To alter the viscosity of the phantom, 0.3% xanthan gum was added to one of the phantoms (#1). The viscosity of phantom is directly related to gum concentration where a higher concentration will result in a larger viscosity of phantom [13]. Secondly, the relations between ultrasound input

voltage and contrast difference at P1 and P2 were measured. The shear wave frequencies were controlled by varying the AM frequency from 100 Hz to 600 Hz with an interval of 100 Hz for both phantoms and the equal-voltage pair for each frequency was found. Subsequently, the shear wave attenuation coefficients were calculated using Equation 6-24 for different shear wave frequencies. Finally, the viscosities of the phantoms were estimated with the least-squares fitting by substituting the density, frequency and the corresponding attenuation coefficient into Equation 6-2. It should be noted that the elasticity was confined to be within 6 kPa based on the result from Chapter 4.

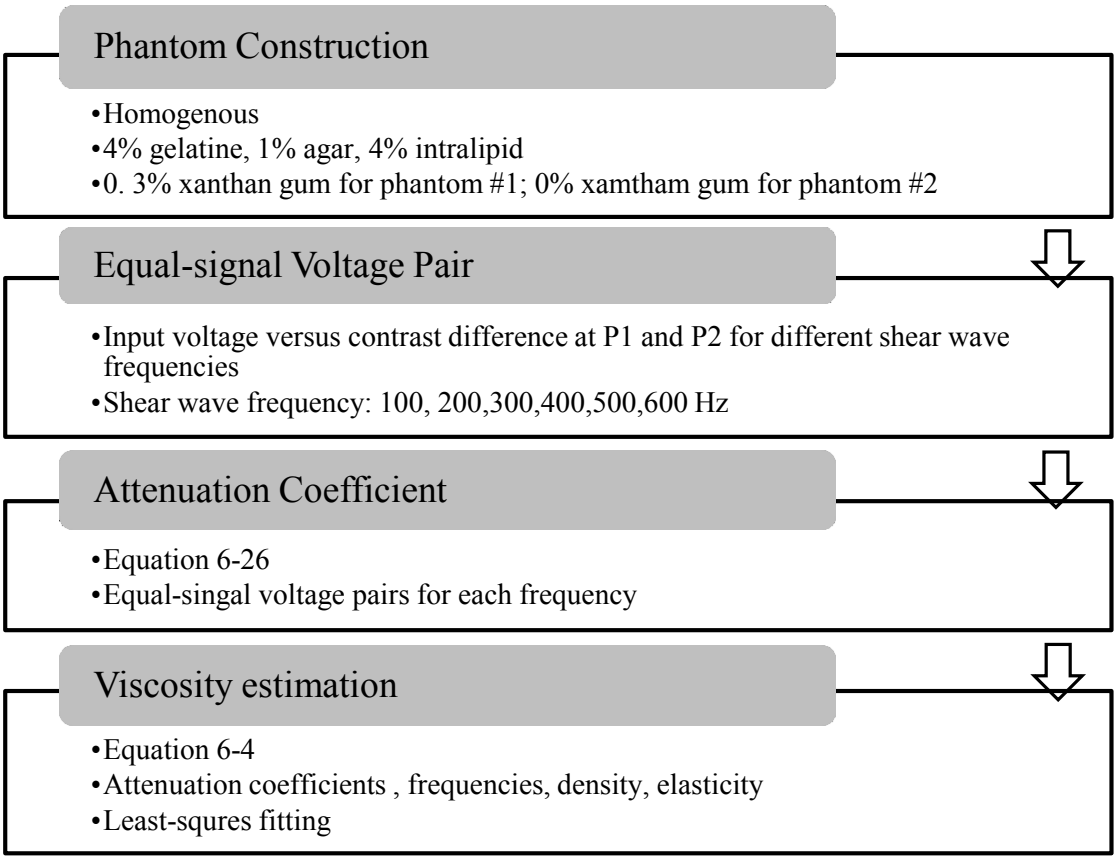

Figure 6.15 Experimental design

6.4.3 Results

Table 6.2 shows the shear wave attenuation coefficients measured in the experiment.

The standard deviations were produced from three repeated measurements. As expected, the shear wave attenuation dispersion is observed with both phantoms - shear wave attenuation increases with the increase of shear wave frequency. The phantom with higher viscosity (#1) has larger attenuation coefficients compared with the less viscous phantom (#2).

Table 6 - 2 Attenuation coefficients over shear wave frequency (f)

f / Phantom	100 Hz	200 Hz	300 Hz	400 Hz	500 Hz	600 Hz
#1 (Np/m)	44.56±2.18	70.63±5.10	90.36±1.93	116.18±7.80	121.62±3.01	126.74±2.50
#2 (Np/m)	7.53±1.76	17.54±3.92	30.20±4.58	36.43±2.74	41.42±4.74	47.50±4.17

Table 6.3 shows that the viscosities measured in the experiment (Row 2) agree with the reference values in [2] (Row 3).

Table 6 - 3 Comparison of SW-LASCA result with reference values in the literature

Phantom	#1	#2
Experiment result (Pa.s)	0.12±0.01	0.35±0.02
Reference value (Pa.s)	0.10±0.02	0.30±0.05

6.4.4 Discussion

This study shows promising results of viscosity measurements in tissue mimicking phantoms using SW-LASCA. The prior information on elasticity can be obtained by measuring the shear wave speed described in [9]. These two methods are based on the same set-up and therefore it is easy to switch between them.

The previously reported ultrasound based method had a bias of ~ 6% on viscosity measurements [10, 15]. This study shows a bias of ~ 17%, assuming the reference values in Table 6.3 are the true values for the viscosity of phantoms. This bias may be caused by three factors. Firstly, shear wave reflection at phantom boundaries may affect the measured contrast difference values and this results in the bias on the attenuation coefficient estimation. In the experiment, the phantom was fixed within a

water tank made of Perspex. Due to the large shear impendence mismatch between the Perspex and the phantom, shear waves were almost totally reflected at the Perspex-phantom interface. Therefore, both the original and reflected shear waves contributed to the contrast difference signal and this may bias the estimation of the shear wave attenuation coefficient. However, this artificially strong shear wave reflection in the experiments may not occur in clinical applications. Secondly, in Equation 6-22, I assumed that identical shear wave amplitudes at the detection point result in identical contrast differences, even if the shear waves originated from two positions along the propagation path. This assumption may not be totally true due to shear wave diffraction: the shear wave with a longer propagation distance will overlap more with the scattered light and so generate a different contrast difference amplitude compared with the shear wave that propagated for a shorter distance. This effect could be minimised by either generating plane shear waves so that less shear wave spreading will be encountered, or decreasing the distance between the two locations so that the change of shear wave geometry may be ignored. Thirdly, in the experiment plane shear wave was assumed where the geometry attenuation of shear wave was neglected. Since the shear waves generated in the experiment spread as propagating, the measured attenuation coefficient could increase and bias the fitting.

A possible way to validate the result is to independently measure the viscosity, e.g. to measure the attenuation of shear wave at different frequencies with ultrasound scanner. However, due to the time limitation and lack of suitable scanner in the lab, I chose to compare with reported values in the literature as shown in Table 6.3. It is necessary to properly validate my method with an independent measurement under controlled environment in near future.

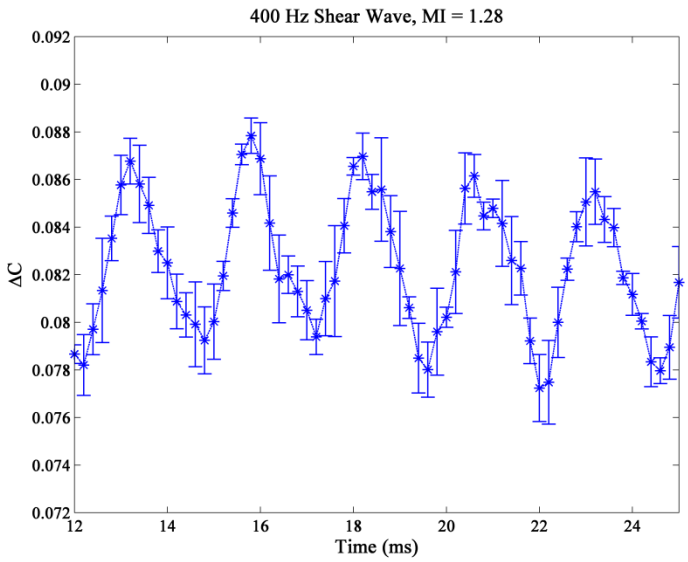

Figure 6.16 Signal with low MI (MI = 1.28). The standard deviation is produced from three repeated measurements.

In Table 6.3, the standard deviation of my measurement is from three repeated measurements. Given the high ultrasound intensity used (for a good signal-to-noise ratio in this feasibility study), I infer the variation is resulted from the thermal effect caused by the ultrasound as viscosity is temperature dependent [14]. In Figure 6.16, I used an ultrasound pressure equivalent to a mechanical index of 1.28 at 5 MHz (well below the ultrasound safety limit MI (mechanical index) =1.9) to generate shear waves. The other parameters were the same as in the previous experiment. Results shows a good signal to noise ratio at MI = 1.28, which proves that it is feasible to reduce ultrasound intensity for the measurement.

6.5 Summary and conclusions

In this chapter, the feasibility of measuring viscosity with SW-LASCA was investigated. Based on the Voigt model, viscosity is related to both shear wave speed and shear wave attenuation. In the first part of this chapter, simulation and experiment

were conducted to study the viscosity measurement using the shear wave speed. Continuous shear waves at difference frequencies were generated and time-resolved contrast signals were obtained. The shear wave speed was supposed to be calculated by finding the time delay between peaks of signals originated from two ultrasound positions. Nevertheless, the signals of the shear wave were deformed, making it hard to find the delay time between ultrasound positions.

In the second part, a method to quantitatively measure the viscosity by shear wave attenuation was proposed. SW-LASCA was used to measure the relation between the input ultrasound power and contrast difference for different shear wave frequencies. The attenuation coefficient was calculated by comparing the signals at two DAO positions. With the prior knowledge of elasticity, viscosity was then inversely solved using the Voigt model. This method is potentially more sensitive to viscosity changes than ultrasound-based methods because the wavelength of light is much smaller than that of the ultrasound. It may also complement visco-elastography techniques based on ultrasound or magnetic resonance imaging by providing optical information of tissues. However, further investigation is needed to assess the feasibility of this method *in vivo*.

References

1. Taylor, L.S., et al., *Viscoelastic effects in sonoelastography: Impact on tumor detectability.* 2001 Ieee Ultrasonics Symposium Proceedings, Vols 1 and 2, 2001: p. 1639-1642.

2. Bercoff, J., et al., *The role of viscosity in the impulse diffraction field of elastic waves induced by the acoustic radiation force.* Ultrasonics, Ferroelectrics and Frequency Control, IEEE Transactions on, 2004. **51**(11): p. 1523-1536.

3. Chen, S., M. Fatemi, and J.F. Greenleaf, *Quantifying elasticity and viscosity from measurement of shear wave speed dispersion.* The Journal of the Acoustical Society of America, 2004. **115**(6): p. 2781-2785.

4. Catheline, S., et al., *Measurement of viscoelastic properties of homogeneous soft solid using transient elastography: An inverse problem approach.* The Journal of the Acoustical Society of America, 2004. **116**(6): p. 3734-3741.

5. Shigao, C., et al., *Comparison of stress field forming methods for vibro-acoustography.* Ultrasonics, Ferroelectrics and Frequency Control, IEEE Transactions on, 2004. **51**(3): p. 313-321.

6. Li, S., et al., *Tracking shear waves in turbid medium by light: theory, simulation, and experiment.* Optics Letters, 2014. **39**(6): p. 1597-1600.

7. Bercoff, J., M. Tanter, and M. Fink, *Supersonic shear imaging: a new technique for soft tissue elasticity mapping.* Ultrasonics, Ferroelectrics and Frequency Control, IEEE Transactions on, 2004. **51**(4): p. 396-409.

8. Wang, L., S.L. Jacques, and L. Zheng, *MCML—Monte Carlo modeling of light transport in multi-layered tissues.* Computer Methods and Programs in Biomedicine, 1995. **47**(2): p. 131-146.

9. Zemp, R., S. Sakadžić, and L.V. Wang, *Stochastic explanation of speckle contrast detection in ultrasound-modulated optical tomography.* Physical Review E, 2006. **73**(6): p. 061920.

10. van Staveren, H.J., et al., *Light scattering in Intralipid-10% in the wavelength range of 400-1100 nm.* Applied Optics, 1991. **30**(31): p. 4507-4514.

11. Torr, G.R., *The acoustic radiation force.* American Journal of Physics, 1984. **52**(5): p. 402-408.

12. van Staveren, H.J., et al., *Light scattering in Intralipid-10% in the wavelength range of 400-1100 nm.* Appl. Opt., 1991. **30**(31): p. 4507-4514.

13. Zatz, J.L. and S. Knapp, *Viscosity of Xanthan Gum Solutions at Low Shear Rates.* Journal of Pharmaceutical Sciences, 1984. **73**(4): p. 468-471.

14. Masuko, T. and J.H. Magill, *A Comprehensive Expression for Temperature Dependence of Liquid Viscosity.* Nihon Reoroji Gakkaishi(Journal of the Society of Rheology, Japan), 1988. **16**(1): p. 22-26.

Chapter 7

Summary, future work and discussions

7.1 Summary

The aim of this project is to build a dual-mode system that measures both the mechanical and optical properties of biological tissue at depths. Surrounding this aim, I carried out four studies with tissue mimicking phantoms.

The first study was about imaging the ultrasound field and shear wave propagation at shallow depths in phantoms. The imaging result of the ultrasound field was consistent with that from a hydrophone measurement, while the shear wave propagation was observed in both homogenous and heterogeneous phantoms. This study provided alternative methods to map ultrasound and shear waves using a single camera shot without scanning.

Based on the observation of shear wave propagation, my second study investigated the feasibility to quantify elasticity with a modified method of ultrasound-modulated optical tomography (UOT) at deep tissue. The shear wave was sensed with speckle images detected in free space and the propagation was tracked by calculating the time-resolved speckle contrast difference before and after the shear wave. In order to acquire an elasticity image with high resolution, I proposed a differential method to track shear waves generated at two distances away from the optical axis. This allowed the quantification of the shear wave speed, and thus the elasticity, by finding the time shift of the signals for these two distances.

The purpose of my third study was to build a dual-mode system that combines opto-elastography with UOT. Further to this purpose, I built a new system that measures

both mechanical and optical properties in the reflection geometry. Compared with the transmission geometry, the reflection geometry is more suitable for clinical applications. The system was demonstrated with heterogeneous phantoms within which inclusions with different properties were embedded. It was found that UOT itself has limited ability to differentiate mechanical and optical inclusions, whereas, the new system can not only differentiate between the two types of inclusions but also quantify their elasticity.

My fourth study investigated the feasibility to measure viscosity with the system since viscosity can add complementary information for discriminating tumours. The Voigt model used in the study allows the quantification of viscosity by measuring the speed or attenuation dispersion of shear waves. The feasibility of measuring speed dispersion with the system was firstly investigated with both experiments and simulation. It is concluded that it is not feasible to measure shear wave speed due to the distortions in the signal. Possible reasons for the distortion were discussed. Furthermore, attenuation dispersion of shear waves was studied and viscosity was quantified and compared with readings obtained with a non-optical method reported in the literature.

These four studies compromise the four main chapters of my thesis. They represent a new system that is sensitive to two types of tissue properties. To my knowledge, this is the first dual-mode technique that measures both optical and mechanical properties deep within tissue mimicking phantoms with optical detection.

7.2 Further work and discussion

The first step for future work is to apply the system *in vitro* and *in vivo*. The potential applications could be breast cancer or lymph node characterisation. In order to

achieve this objective, several aspects need to be improved.

The first is speckle contrast and its decorrelation. In laser speckle contrast measurement, the CCD contrast value is exposure time dependent. In UOT, exposure time affects measurement resolution because a long exposure time leads additional modulation from shear waves which spread away from the ultrasound focus and degrade the UOT resolution. On the contrary, a short exposure time decreases detected light intensity and thus the signal-to-noise ratio. In elasticity measurements, exposure time should not influence the timing of the contrast difference signal peak but it does affect the signal-to-noise ratio and hence the accuracy of estimates of the peak time. In viscosity measurements, exposure time affects signal amplitude but it may not affect the difference between the two signals and the final fitting process. However, noise increases with short exposure times, which could induce errors in the measurement. Laser speckle contrast measurement also suffers from speckle decorrelation where speckle contrast decreases because of motions, e.g. blood flow, Brownian motion and body movements. In order to minimise the contrast decorrelation, short exposure times are needed. This again decreases the signal-to-noise ratio of the signal. Experimentally, a 2 ms exposure time was used and an excellent signal to noise ratio was obtained. This provides the possibility to reduce the exposure time given that the speckle decorrelation is faster in the human body than in these phantoms. However, to what extent the measurements will be affected by speckle decorrelation and exposure time need to be investigated.

The second problem concerns the camera. The CCD camera I used has a very limited frame rate (10 fps) and hence the shear wave tracking needs to be done by repeatedly generating shear waves and delaying the timing of CCD exposure. A fast camera

would be better, not only because it would help improve the imaging speed but also because it would avoid repeated ultrasound transmission and hence reduces potential thermal damages both to the transducer and to the tissue due to the transmission of high energy ultrasound bursts.

Thirdly, a single element transducer was used to generate the shear waves at two positions by translating the transducer to different positions. In the future, a multi-element transducer is required to replace the mechanical translation by dynamic ultrasound beam steering, which will provide a faster and more flexible measurement.

The next problem concerns the laser. The scattering and absorption coefficients of a green laser in biological tissues are much higher than a near-infrared laser. Therefore, the current laser should be replaced with a near-infrared laser to increase both the signal-to-noise ratio and the imaging depth. Moreover, a pulsed and synchronised laser could help improve the system compared with the current continuous wave laser. In one aspect, pulsed lasers allow the use of higher instantaneous power compared with continuous wave lasers, such that the signal intensity could be improved. In another aspect, synchronising the laser with ultrasound and CCD exposure time could reduce the scan time of UOT by illuminating the tissue at the moment when the ultrasound pulse propagates to different depths, such that an axial scan could be accomplished using one ultrasound pulse.

The final question concerns the safety of using ultrasound and lasers. High ultrasound and light energy could induce tissue damage, such as burning and capillary bleeding. At the early stage of this development, ultrasound and laser safety were not fully considered. The mechanical index (MI) of ultrasound used in the experiments was generally higher than the maximum MI that is allowed in the clinic in order to obtain

an excellent signal to noise ratio. Although some experiments were made with a lower MI, the influence of using a low MI on the measurements, including the feasibility and accuracy, needs to be investigated. The safety power for a laser varies with the exposure duration and wavelength. In the future, for *in vitro* and *in vivo* applications, the laser should be properly chosen based on safety guidance. In addition, using a pulsed and synchronised laser could also help avoid potential damages.

Another step forward would be quantification of the optical properties. The current system acquires only qualitative optical absorption information. For more robust diagnose, quantification of the optical properties would be useful. However, quantifying optical properties is challenging, because, from one aspect, the system is sensitive to mechanical contrast, which affects the quantification of optical properties by adding extra mechanical signals, and, from another aspect, the high scattering of light in tissue reduces spatial information, which makes it difficult to quantify local optical properties. Therefore, the first new study should be on compensation of the optical signal, which extracts pure optical signals from the detected signal. This could be feasible since the mechanical sensitivity of the system depends on the experimental setting, such as the ultrasound pressure and light intensity. The next study could use diffuse optical tomography as a reference, which reconstructs the optical properties in deep tissue.